AD-A087 076 AVCO SYSTEMS DIV WILMINGTON MA F/G 11/4
HIGH ENERGY DENSITY COMPOSITE FLYWHEEL PROGRAM.(U)
MAY 80 A D SAPOWITH, A L GURSON, J A MCELMAN DAAG53-75-C-0269
UNCLASSIFIED AVSD-0170-80-RR NL

1 OF 2
AD A
087076

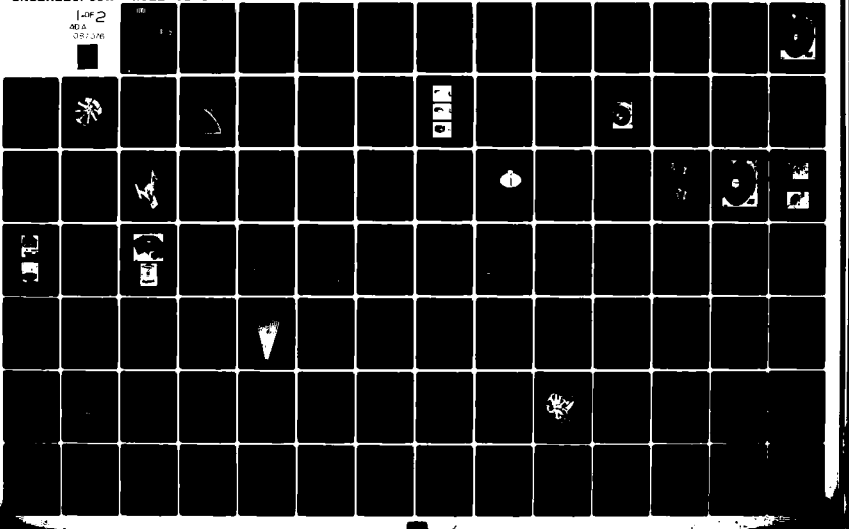

PHASE II – FINAL REPORT

HIGH ENERGY DENSITY COMPOSITE FLYWHEEL PROGRAM

AVSD-0170-80-RR

For Period June 1976 – May 1980

Prepared for

U.S. ARMY MOBILITY EQUIPMENT
RESEARCH AND DEVELOPMENT CENTER
Fort Belvoir, Virginia 22060

Contract No. DAAG53-75-C-0269

30 May 1980

Prepared by

AVCO SYSTEMS DIVISION
Wilmington, Massachusetts 01887
Lowell, Massachusetts 01851

UNCLASSIFIED

SECURITY CLASSIFICATION OF THIS PAGE *(When Data Entered)*

REPORT DOCUMENTATION PAGE	READ INSTRUCTIONS BEFORE COMPLETING FORM
1. REPORT NUMBER (14) AVSD-0170-80-RR	2. GOVT ACCESSION NO. AD-A087076	3. RECIPIENT'S CATALOG NUMBER
4. TITLE *(and Subtitle)* (6) Phase I Final Report / High Energy Density Composite Flywheel Program	5. TYPE OF REPORT & PERIOD COVERED (9) Final Report. June 76 — May 80 on Phase 2
	6. PERFORMING ORG. REPORT NUMBER
7. AUTHOR(S) (10) Sapowith, A. D. / Sapowith Gurson, A. L. / Gurson McElman, J. A. / McElman	8. CONTRACT OR GRANT NUMBER *(s)* (15) DAAG 53-75-C-0269
9. PERFORMING ORGANIZATION NAME AND ADDRESS Avco Systems Division 201 Lowell Street Wilmington, Massachusetts 01887	10. PROGRAM ELEMENT, PROJECT, TASK AREA & WORK UNIT NUMBERS
11. CONTROLLING OFFICE NAME AND ADDRESS U.S. Army Mobility Equipment Research and Development Center Fort Belvoir, Virginia 22060 (11)	12. REPORT DATE 30 May 1980 13. NUMBER OF PAGES 154
14. MONITORING AGENCY NAME AND ADDRESS *(if different from Controlling Office)* (12) 155	15. SECURITY CLASS. *(of this report)* Unclassified 15a DECLASSIFICATION/ DOWNGRADING SCHEDULE

16. DISTRIBUTION STATEMENT *(of this Report)*

Approved for public release
Distribution unlimited

17. DISTRIBUTION STATEMENT *(of the abstract entered in Block 20, if different from Report)*

18. SUPPLEMENTARY NOTES

19. KEY WORDS *(Continue on reverse side if necessary and identify by block number)*

Flywheels
Composites
Kevlar
Burst Containment

20. ABSTRACT *(Continue on reverse side if necessary and identify by block number)*

A bi-directional composite flywheel was instrumented with strain gages and tested to destruction. The flywheel was designed to exhibit constant stress in both radial and circumferential directions for all radial positions. Strain gage data verified this design. The burst speed was 38,741 rpm representing a specific energy level of 32.3 Wh/lb.

DD FORM 1 JAN 73 1473 EDITION OF 1 NOV 65 IS OBSOLETE

UNCLASSIFIED

SECURITY CLASSIFICATION OF THIS PAGE *(When Data Entered)*

404788

20. ABSTRACT (Cont'd)

The flywheel was constructed of Kevlar composite, had an outside diameter of 19.5", an axial thickness of 1.5" and weighed 18.6 lbs. Premature failure was initiated at the inside diameter by excessive pressure exerted by a metal hub. A polyarylate hub design, with test data, is presented to solve this problem.

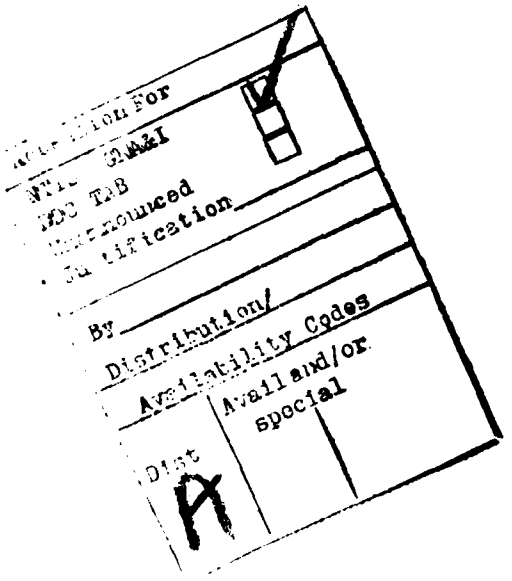

PREFACE

This is the Phase II report for the "Development of a High Energy Density Flywheel". The work was performed for MERADCOM, formerly MERDC, U. S. Army, Ft. Belvoir, Virgina, under Contract Number DAAG53-75-C-0269. It covers the period of June 1976 through May 1980.

Acknowledgement is made to Dr. L. Amstutz, MERADCOM, who has served as Program Manager for the Army and provided continuous support and belief in our design concept throughout the program.

CONTENTS

ILLUSTRATIONS

ILLUSTRATIONS (Cont'd)

ILLUSTRATIONS (Cont'd)

ILLUSTRATIONS (Cont'd)

ILLUSTRATIONS (Concl'd)

TABLES

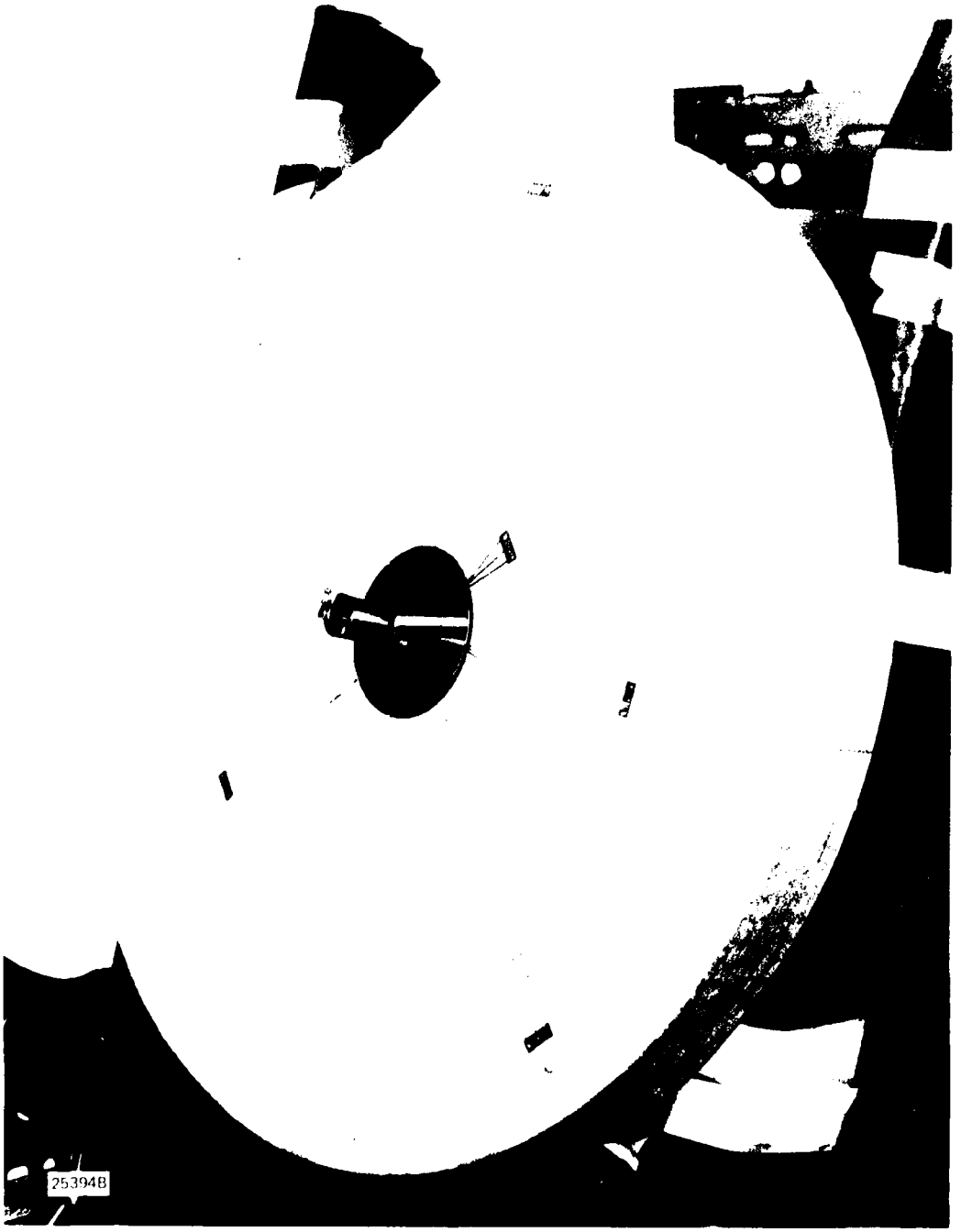

Figure 1 SECOND KEVLAR FLYWHEEL

SECTION 1.0 INTRODUCTION AND SUMMARY

A unique constant stress bi-directional composite design for high energy density flywheels has been demonstrated.* An 18.6 pound subscale Kevlar flywheel (Figure 1) was tested to destruction exhibiting a specific energy level at a burst of 32.3 watt-hours/pound. This flywheel was instrumented with strain gages whose measurements verify Avco's constant stress design approach.

Plagued by several years of dynamic and interface problems between our highly stressed composite flywheel and negligibly stressed metal drives, a special metal hub (Figure 2) was developed to conduct a vertical spindle mounted test of the flywheel without having to pass through critical resonances. Further analyses and design efforts have developed a hub which now satisfies the dynamic and interface problems for both spindle and axle mounted flywheels. The hub is made from a new polymer material, polyarylite, not available at the start of the program. It has among its unique properties, the capability of being injection molded. The hub geometric design in this material is a modified Stodola flywheel lightly contained by the inside diameter of the constant stress composite flywheel (Figure 3).

Avco's constant stress design is fully described in the Phase I report, Reference 1. In brief, the design constitutes a cross ply construction of hoop (circumferential) fibers and radial fibers. The fibers can be in alternate layers or integrated in each layer. The hoop fibers ultimately carry all inertial loads. The radial fibers are so constructed as to equalize these loads over the flywheel. The resulting pattern of radial on hoop fibers is shown in Figure 4. This design theoretically results in a constant (radial and circumferential) stress flywheel independent of stress direction or location. Loads and stresses in the axial direction are not critical. The key to this design is the adjustment of radial to hoop stiffness as a function of radial station.

The flywheel shape results in a hollow right circular cylinder that fills almost the entire swept volume of the flywheel envelope with high energy density composite materials. The design is applicable to any of the high strength-to-weight fiber composites. From an energy density standpoint, this is the ultimate achievement.

The Kevlar wheel design efficiency was reduced some 5% to minimize interlaminar shear loads. The result was a near constant stress flywheel. Figure 5 shows the raw strain data vs. speed obtained in the test at three radial stations: 2.7, 5.7 and 8.25 inches. The hoop stresses are remarkably uniform. For comparison, a flywheel

*Patent Pending.

25287 B

Figure 2 SPINDLE HUB (STEEL)

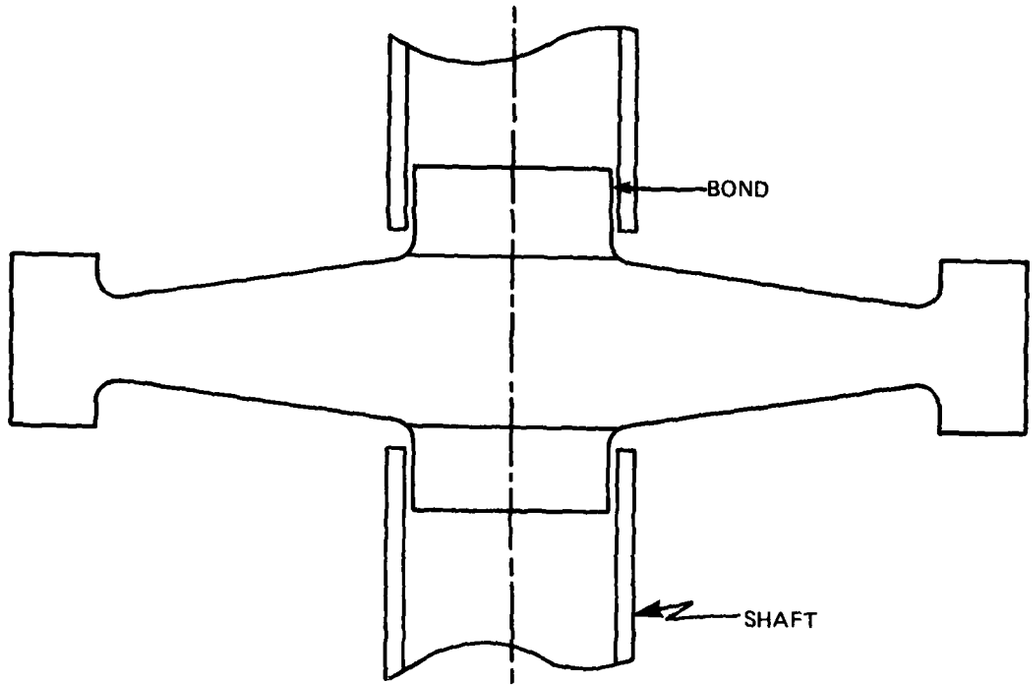

Figure 3 POLYARYLITE HUB – MODIFIED STODOLA SHAPE

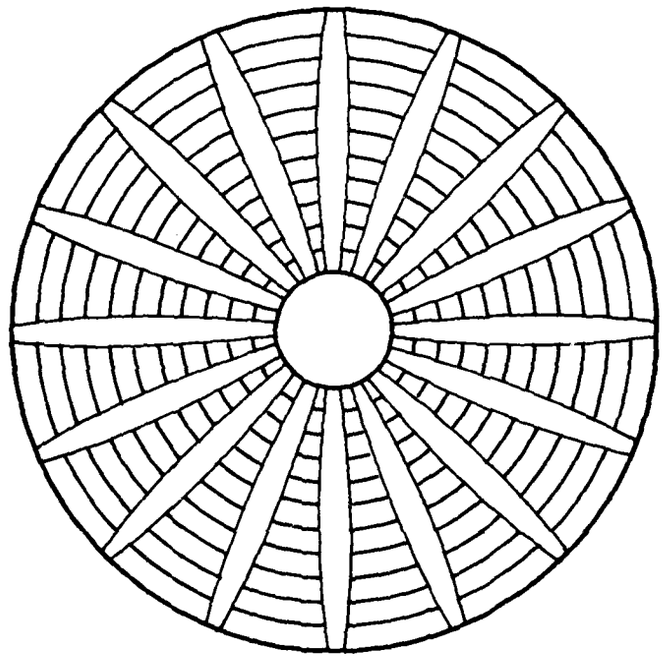

85-1569

Figure 4 SCHEMATIC OF TYPICAL BI-DIRECTIONALLY REINFORCED FLYWHEEL

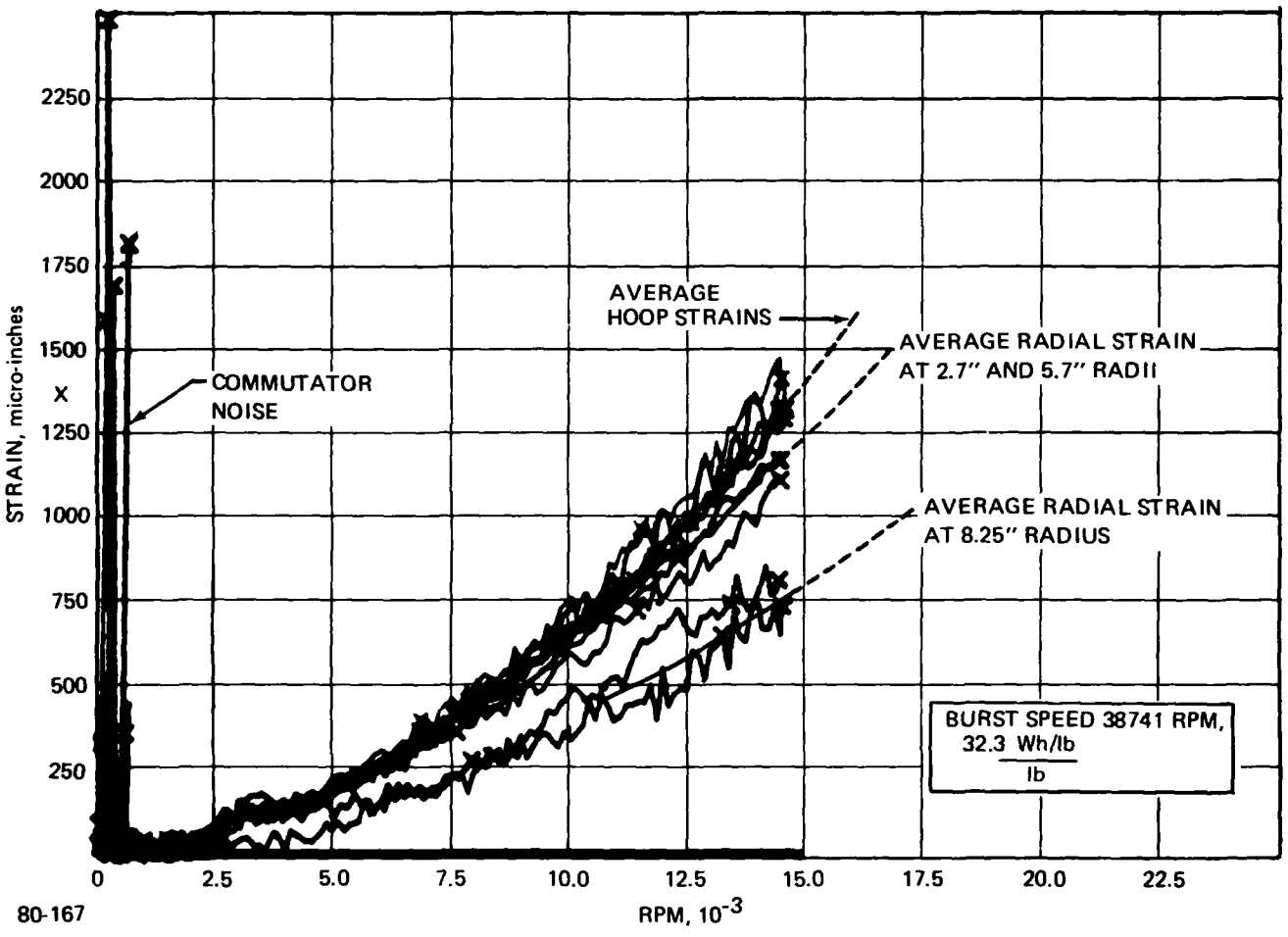

Figure 5 RAW STRAIN DATA

without this radial design would experience hoop strains proportional to the square of the radius or a factor of 10:1. The outer radial strains do experience some fall off as predicted. The radial strain at the inside and outside diameters (ID and OD) must be zero. Figure 6 shows a plot of the predicted values of the ratio $\varepsilon_r/\varepsilon_\theta$. Superimposed on this plot are the measured values. There is very good correlation between the predicted to measured strain ratios.

Pressure on the inside diameter of the flywheel by the metal hub coupled with the low cross-fiber properties of Kevlar have been identified as the factors that caused premature failure. The new hub design results in markedly decreased pressure on the ID.

The basic conclusion reached from this program is that high energy density composite flywheels operating at 40 Wh/lb and able to deliver high power levels are entirely feasible. Accordingly, there are two recommended alternative development paths to follow and they could be conducted in parallel. The first is to extend the present high confidence design utilizing low cost fabrication techniques. The second is to modify the design for integration and combination with a motor/generator, a high risk, high payoff effort.

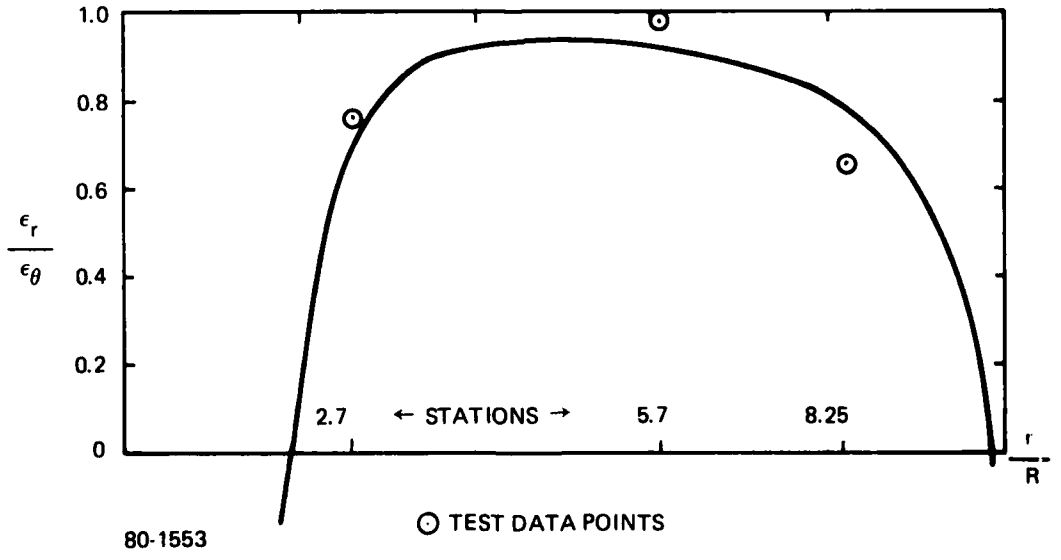

Figure 6 $\frac{\epsilon_r}{\epsilon_\theta}$ vs. RADIUS AND SPIN RATE – 16,000 RPM

SECTION 2.0 BACKGROUND AND PHASE II OBJECTIVES

The initial plan for the MERADCOM Program was to develop a high energy density flywheel in two phases. Phase I was to demonstrate concept feasibility with analyses, component and subscale tests. Phase II was to build and demonstrate a 750-lb flywheel capable of storing 40 Wh/lb operationally and delivering at least 3215 KW of power.

A series of difficulties were encountered in Phase I so that concept feasibility was not proven. The detailed analyses and component/material test data all indicated that Avco's unique concept of designing a high energy density constant stress flywheel was valid. These are fully detailed in the Phase I report. The concept was not believed to be amenable to static subscale tests such as a hoop tensile test that could be run on a simple ring. It was believed that only a burst test could serve as incontestable proof of energy storage capacity.

The second and major difficulty in demonstrating concept feasibility was in the design choice of the flywheel hub. A match had to be made to interface strains of the flywheel ID at a maximum strain value of at least 1% (1% graphite, 1.6% Kevlar, 2.5% fiberglass), with a steel shaft undergoing negligible strain. For a 3.2-inch flywheel ID, the radial displacement for a Kevlar wheel is 0.026 inch. To match this radial growth and still have sufficient hub to flywheel stiffness to be able to design away from critical vibrational resonances, has almost been the Achilles heel of the Avco concept. A flywheel using 90% of the swept volume with high energy density composite materials is academic if there is no hub to drive it. The solution of this problem has been demonstrated for vertical spindle mounted flywheels, and analyses, herein, describe an improved design applicable to both spindle mounts and horizontal or vertical axle mounted flywheels.

The initial hub designs, a rubber bond mount and a flexible steel mount, both matched the ID growth, and both experienced critical resonances which caused flywheel failure. Table 1 summarizes the key data for the first three subscale wheels tested in Phase I. The hub lateral (in the plane of the flywheel) and rotational stiffnesses K_L and K_θ are shown together with the hub weight and effective spindle length. These are the key factors in determining the various resonances. The predicted first and second shaft modes are shown. Not shown is the first pendulum mode, approximately 200 rpm for all wheels. The predicted amplitudes for each resonance was small. Classically predicting the resonance point is far more accurate than predicting the resulting amplitudes.

TABLE 1. PHASE I – FLYWHEEL DATA

Flywheel	Composite Wheel Weight (lb)	Steel Hub Weight (lb)	Hub Stiffness K_L lbs/in	Hub Stiffness K_α in-lbs/rad	Effective Spindle Length (inch)	Predicted Resonance (rpm) 1st Shaft Mode	Predicted Resonance (rpm) 2nd Shaft Mode	Test Results Failure Speed (rpm)
Graphite	19.8	10.7	$6.31\ 10^4$	$4.05\ 10^4$	10	8,100	17,600	17,700
Steel	25.5	9.3	$3.19\ 10^5$	$5.94\ 10^6$	1[illegible]	16,550	34,850	17,650
1st Kevlar	16.9	10.4	$6.02\ 10^5$	$3.31\ 10^6$	10.3	21,800	46,900	20,200

The graphite wheel did pass through its first shaft mode. The amplitudes were highly damped. It did not survive the second mode. Figure 7 shows the hub shaft progressively ripping its way from the inside diameter (ID) to the outside diameter (OD) of the flywheel. Similar photographic evidence of hub failure for the steel wheel was obtained. While no photographic proof was obtained on the first Kevlar flywheel, it too failed at or near a resonance point. In all cases, the displacement probe readings which monitored the shaft movement showed increasing amplitudes with the approach of resonance.

At this point, a reevaluation of the program objectives had to be made. To demonstrate the concept, a hub at least compatible for a vertical spindle mounted burst test was needed. Hub designs capable of operating with a vehicular axle mount would have to await proof of concept. In a detailed design review, it became clear that Avco's design objective was to markedly reduce the hub weight so that the critical shaft resonances would depend on hub weight to stiffness. Two designs were postulated. The first (Figure 8) was symmetrical and weighed 3.75 lbs. The second (Figure 9) considered more radical at the time, was asymmetrical and weighed less than one pound. It is the second design that was developed in Phase II.

While evaluation of Avco's hub resonance problem promised a solution that would allow a meaningful burst test, past experience cast some doubt on its projected success. Since the design concept was to result in a constant stress flywheel, it was decided to instrument the wheel with strain gages to determine just how constant a stress was actually developed. It was realized that the presence of strain gages might induce a premature failure; however, measuring the stress distribution achieved was deemed of first priority. Accordingly, the following objectives and tasks for Phase II were established:

(1) Refabricate a duplicate Kevlar flywheel identical to the Phase I Kevlar flywheel.

Figure 7 DYNAMIC FAILURE OF HUB (FIRST GRAPHITE WHEEL TEST)

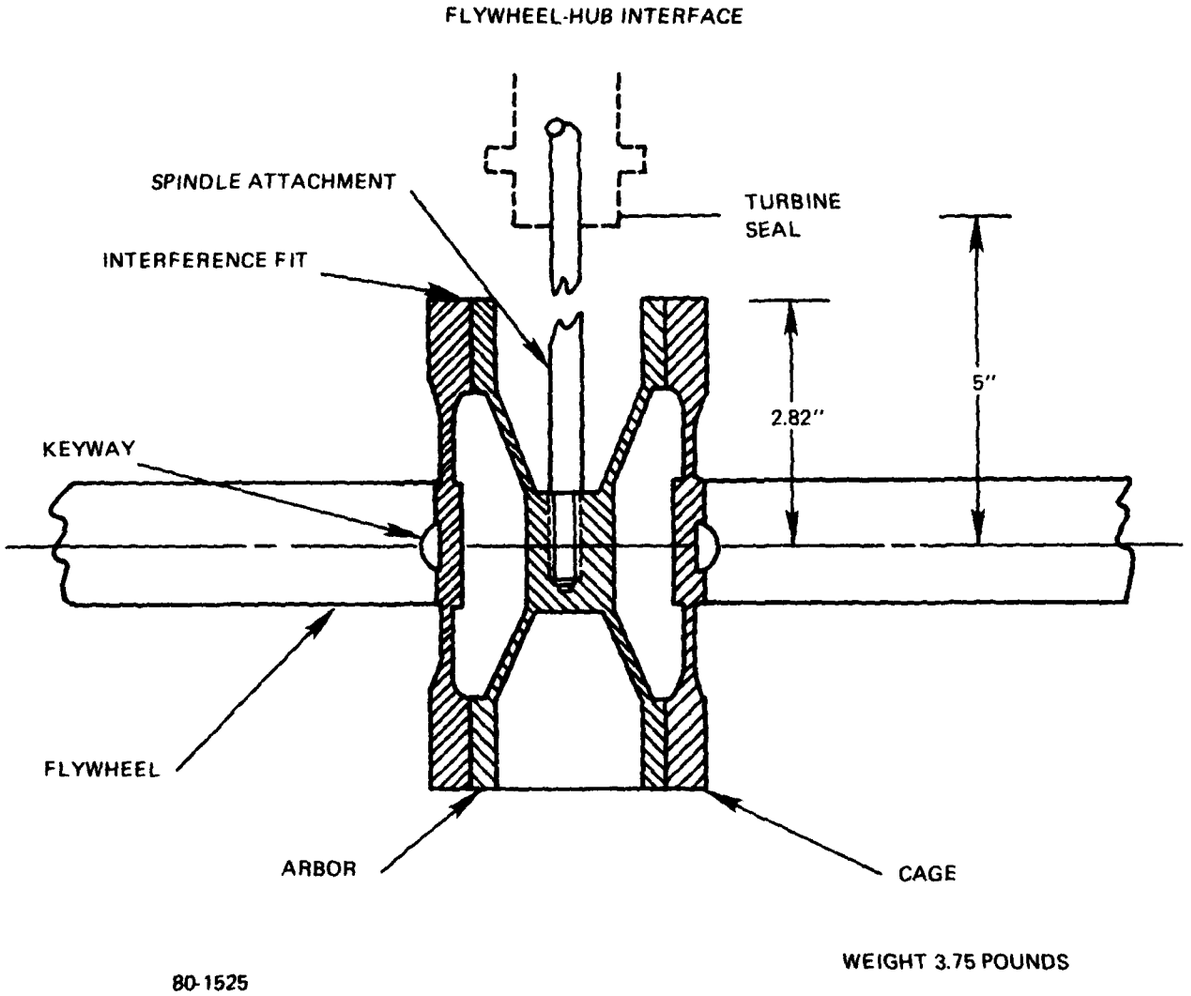

Figure 8 FLYWHEEL – HUB INTERFACE

(2) Design and fabricate a hub capable of functioning during at least a spindle test to burst.

(3) Instrument the flywheel with strain gages to determine stress (strain) distribution over the flywheel.

(4) Conduct a spin test to burst and monitor strain vs. speed over the flywheel.

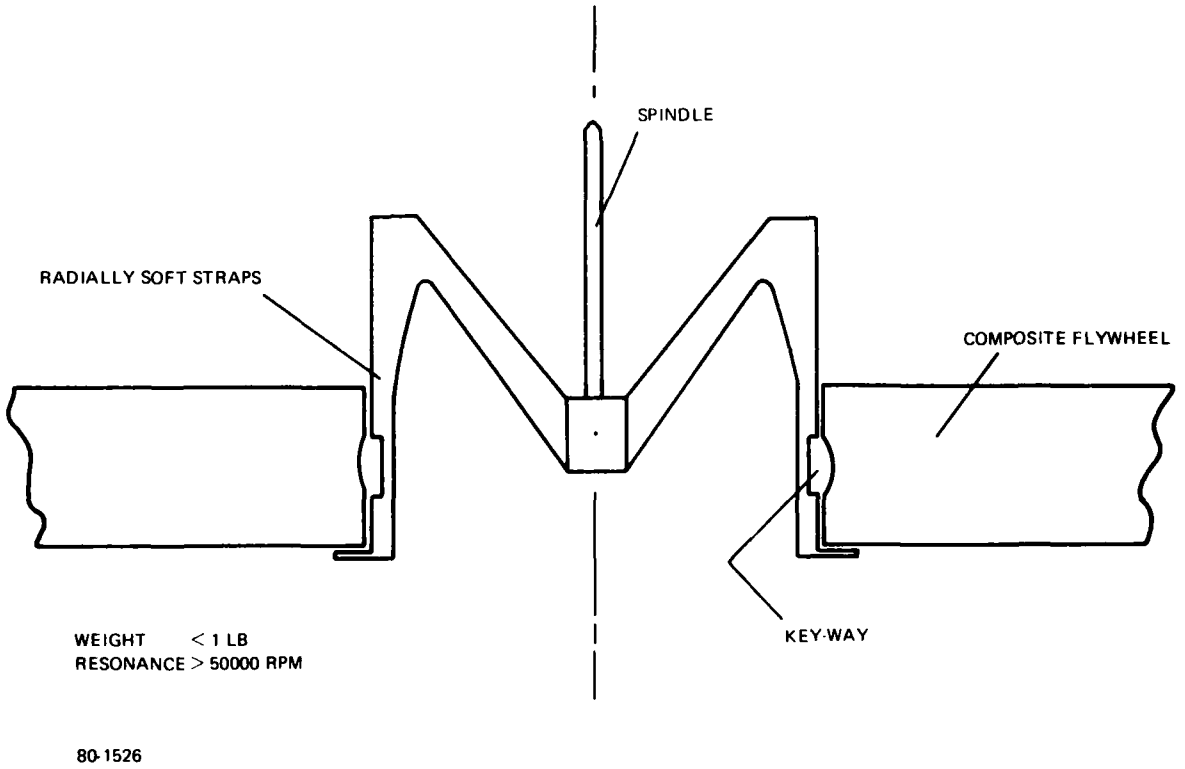

Figure 9 REVISED TEST HUB DESIGN

SECTION 3.0 COMPOSITE FLYWHEEL DATA

The wheel design concept and detailed design are covered in the Phase I report. The composite layup formed a right circular cylinder with an ID and OD machined to 3.2 and 19.5 inches; the molded thickness was 1.50 inches. These dimensions resulted in a swept volume usage, or volume of the composite to volume of the composite outside envelope of 97 percent. The weight was 18.6 pounds (8450 grams). Figure 10 shows the OD of the composite flywheel being machined.

The computed shape factor K_s was 0.474 compared to the maximum attainable for composites Of 0.5. Based on the minimum measured tensile allowables for Kevlar (189,000 psi), the burst energy level predicted was 58 Wh/lb at a speed of 52,770 rpm.

80-1527

Figure 10 MACHINING OF SECOND KEVLAR FLYWHEEL OD

SECTION 4.0 SPINDLE HUB DESIGN

The key problem to be solved with the hub was to make it sufficiently lightweight so that the first resonant frequency beyond the pendulum mode would be greater than the speed range of the burst test. A weight goal of one pound for the hub was chosen. If met, the 18-pound Kevlar wheel would act as ground, and the resonance would almost solely depend on the hub stiffness/weight properties.

The second key problem was to design a metal hub that was compatible with the growth of the Kevlar wheel. This growth was expected to be as high as 1.6% strain. To accomplish this, the design concept chosen was a set of fingers or arms which span the distance from the centerline to the wheel ID and act as cantilevered beams.

To establish the basic hub arm and hub weight requirements to satisfy the resonant frequency goals a simplified hub model was chosen as shown in Figure 11. The 0.8-inch diameter neck was fixed as the near minimum central cylinder required for spindle interface. The spindle set screws were fixed at what was considered the minimum allowable distance from the turbine bottom face. Dimension A, turbine face to top of flywheel, was varied, which in turn affected the weight of the neck. The combined arm stiffnesses K_L (lateral) and K_θ (rotational) were also varied over what was computed to be practical obtainable values. The frequency trade data are shown in Table 2. It was seen that frequency increased as spindle length and length A decreased. Frequency increased as the attachment of the spindle to the hub became more rigid. Case 10 satisfied the frequency goals. If the design parameters in Case 10 could be beaten or met the frequency goals could be obtained.

TABLE 2. HUB FREQUENCY TRADE ANALYSES

Case	1	2	3	4	5	6	7	8	9	10	Spindle Hub Design
Spindle Length (inches)	6.14	6.14	6.14	3.76	3.76	3.76	6.14	3.76	6.14	6.14	5.66
Arm Length A to top of wheel (inches)	5.625	5.625	5.625	5.625	5.625	5.625	5.625	5.625	1.65	1.65	0.99
K_L lbs/in 10^{-5}	2.5 10^5	fix	Pin	2.5 10^5	fix	Pin	2.5 10^5	2.5 10^5	2.5 10^5	2.5 10^5	2.5 10^5
K_θ rad/in lb 10^{-5}	12.5 10^5	fix	fix	12.5 10^5	fix	fix	3.0 10^5	3.0 10^5	12.5 10^5	3.0 10^5	3.0 10^5
Freq. rpm 10^{-3}	33.6	38.9	6.4	50.2	56	12.6	28	44.6	106.7	87.2	157.7
Pendelum freq. rpm	280	280	230	480	480	300	280	480	710	720	1301*

*1533 rpm measured

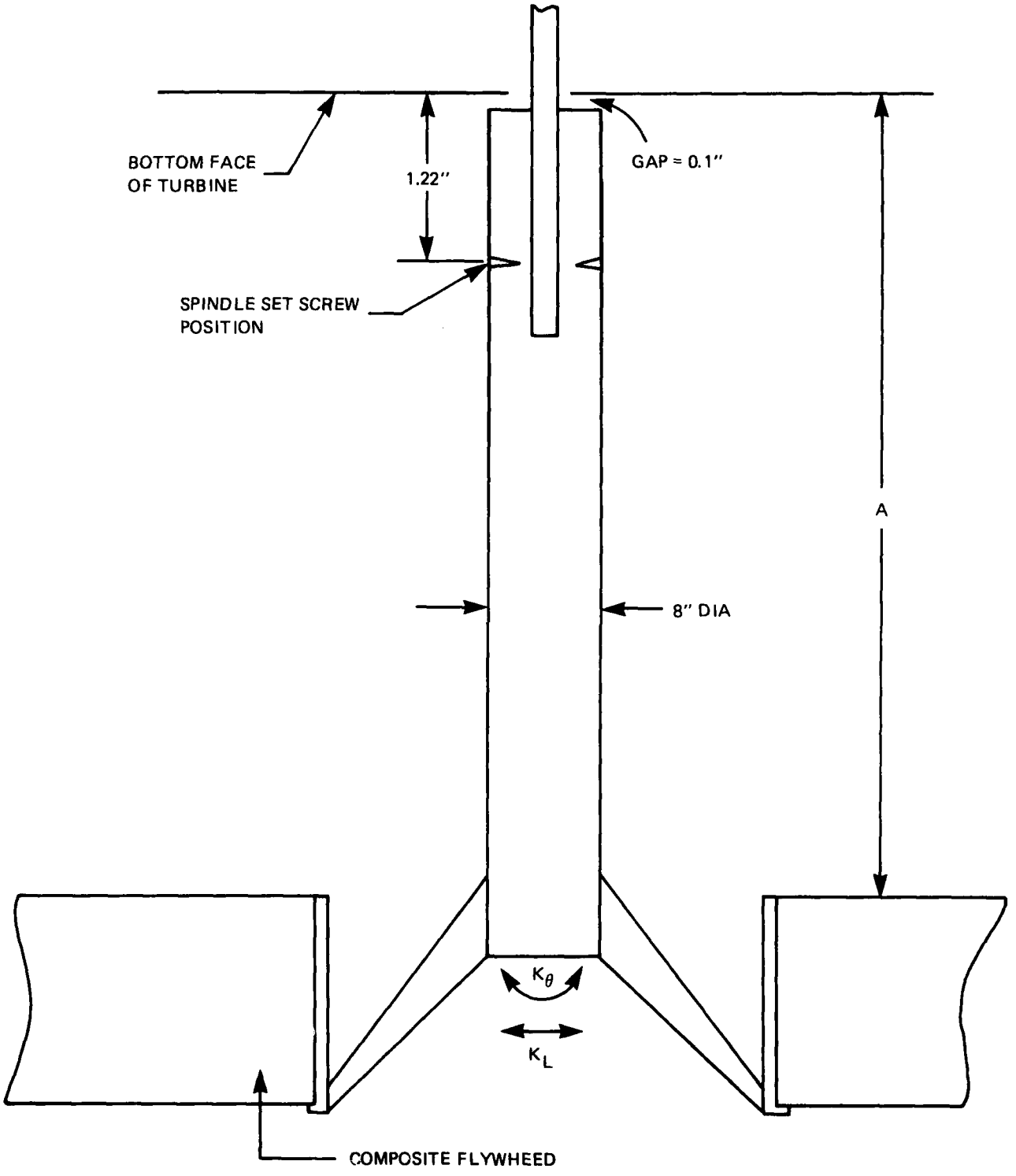

Figure 11 SIMPLIFIED HUB MODEL

In order to cover the large deformation of the composite ID with the stiffest acceptable arm it was decided to prestress or "squeeze" the arms into the ID. This allowed an arm to stress from compressive to tensile condition doubling the linear elastic range. The pressure from the arms was distributed by pads. The friction from the pad pressure was sufficient to drive the flywheel. As spin and ID increased, the pressure from the pre-stress went to zero and became negative; however, the centrifugal forces maintained or increased the pressure with speed. Friction was to be employed with no bond as previous designs had investigated both soft and hard bonds between the hub and wheel and found serious strain incompatibilities. While friction alone was more than sufficient to maintain the wheel, a small lip was to be provided at the base of each pad to ensure against wheel slippage in the vertical direction.

The arms had to be strong enough to withstand the centrifugal loads. This called for a stiff arm or deep section. As the arms increased in size, so did the weight, which reduced the resonant frequency point. The deeper or thicker the section, the more difficult it would be to bend the cantilevered arms and the higher the pressure on the ID. The angle of the arms also affected stiffness; the larger the angle the stiffer the arm. Thus, there were tradeoffs of static pre-stress to dynamic stress under spin conditions. Figure 12 shows some of these tradeoffs. It can be seen that minimum stress is indicated at about 0.016-inch "squeeze" or initial arm deflection per radius.

It was desirable that the metal pads at the ID distribute the loads from the preloaded arms over the complete ID surface. This called for stiff, thick pads. At high speed the thicker pads caused high centrifugal loads or compressive loads against the ID, thus a tradeoff in pad thickness.

A detailed design was developed from the above tradeoffs. Its general shape is shown in Figure 13. Prior to finalizing the interference between the hub and flywheel and prior to final machining of the flywheel ID and hub OD, flat piece specimens of hub material were fabricated simulating the neck, arm and pad design (Figure 14). The arms of these specimens were instrumented with strain gages. Tests simulating the squeezing of the hub into the wheel ID were conducted and the arm stresses measured. Figure 15 shows the change in diameter vs. tensile and compressive stresses in the arm. For static preloading compressive stresses were critical. The initial squeeze of 0.016 inch was chosen.

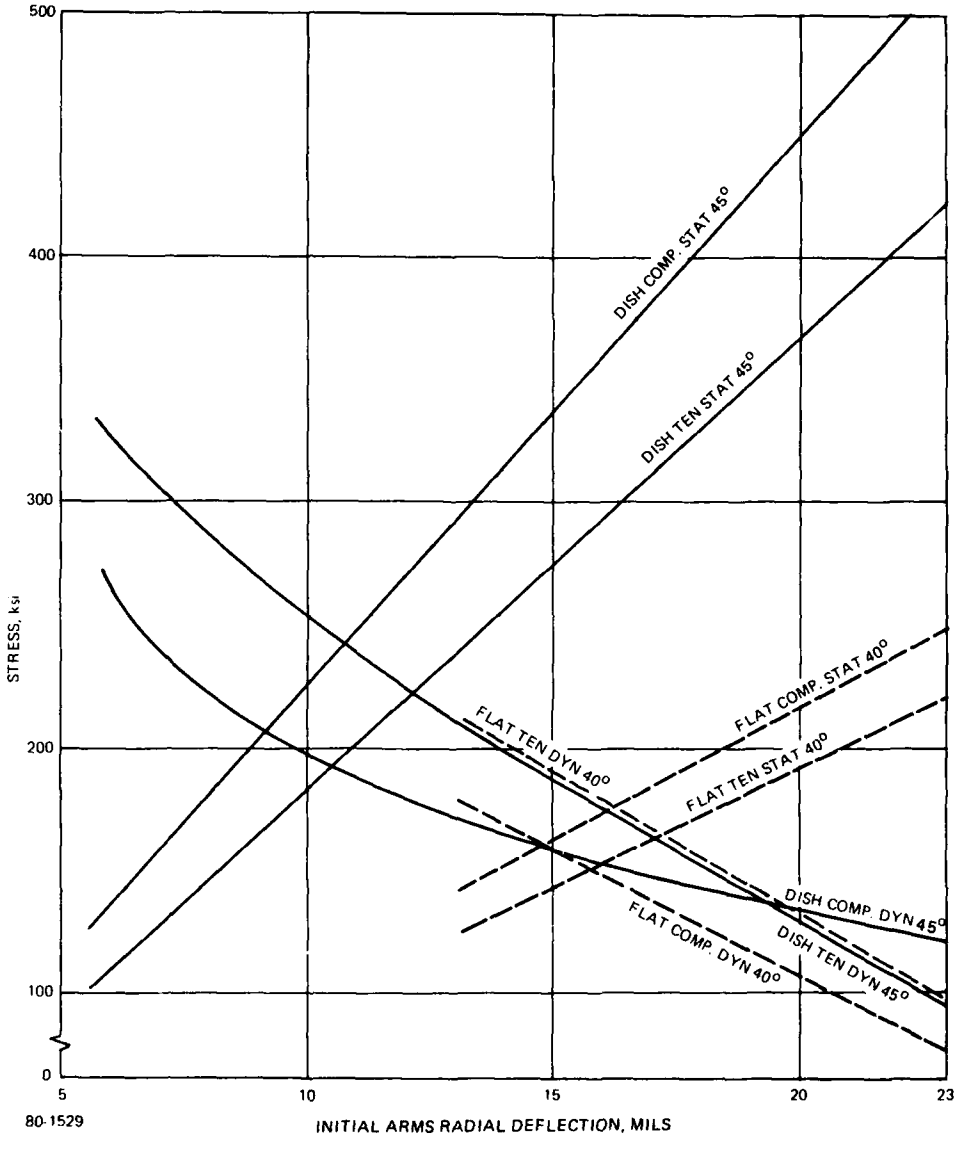

Figure 12 HUB ARM DESIGN TRADEOFFS

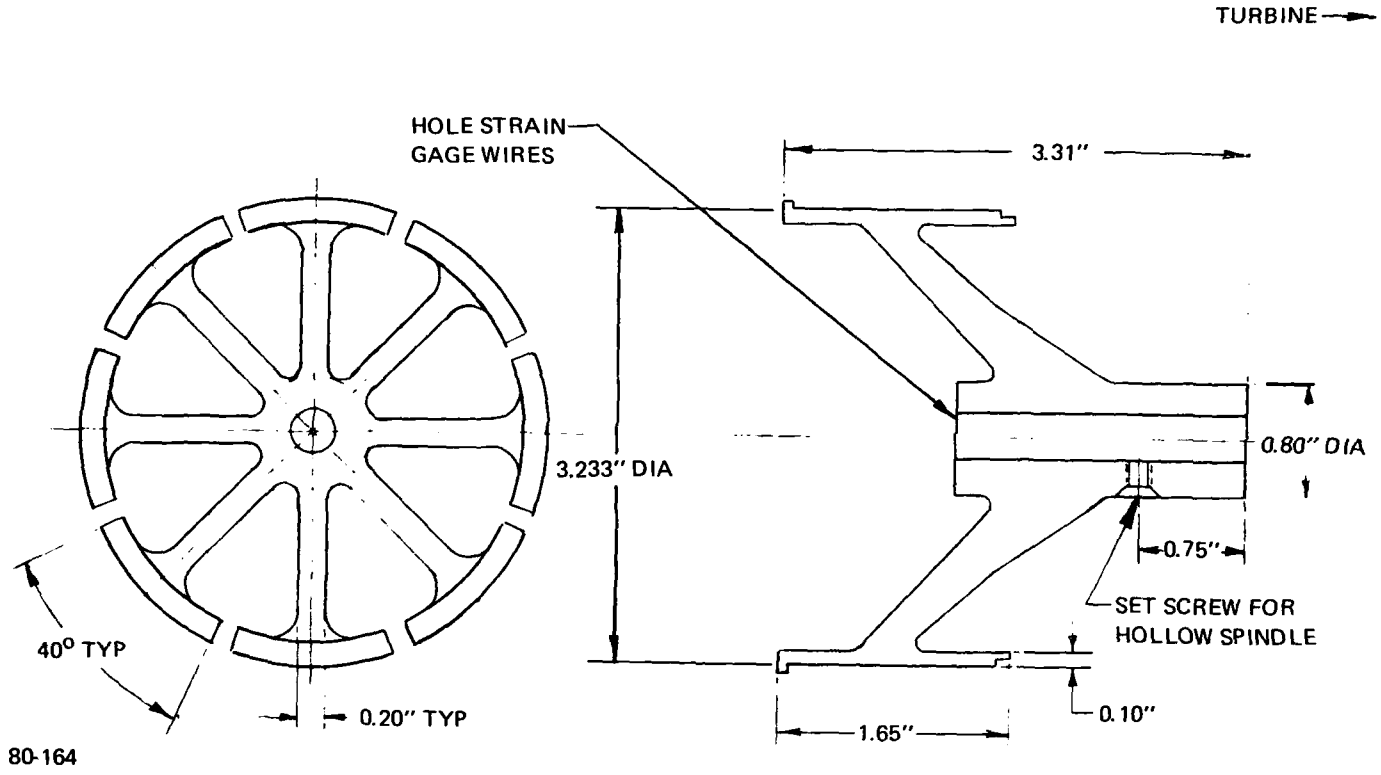

Figure 13 SPINDLE HUB FOR KEVLAR TEST

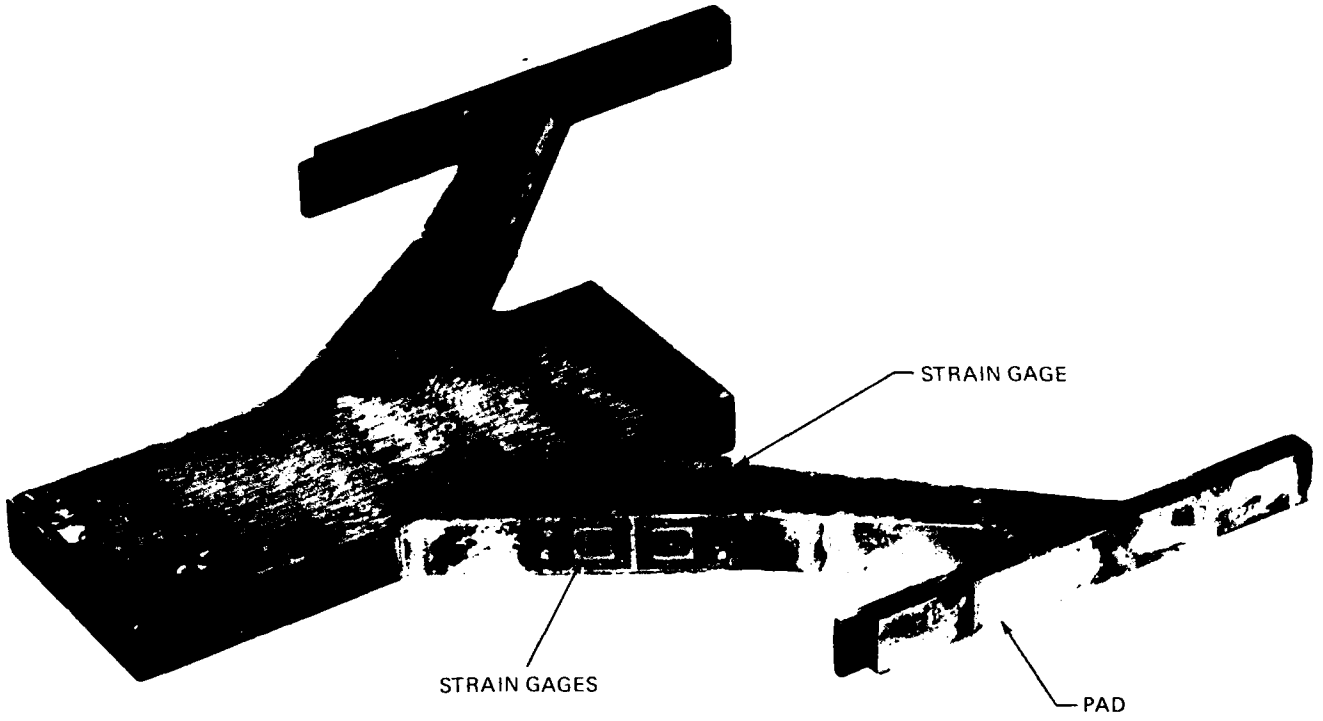

80-1530

29149-B

Figure 14 FLAT PIECE SPECIMEN

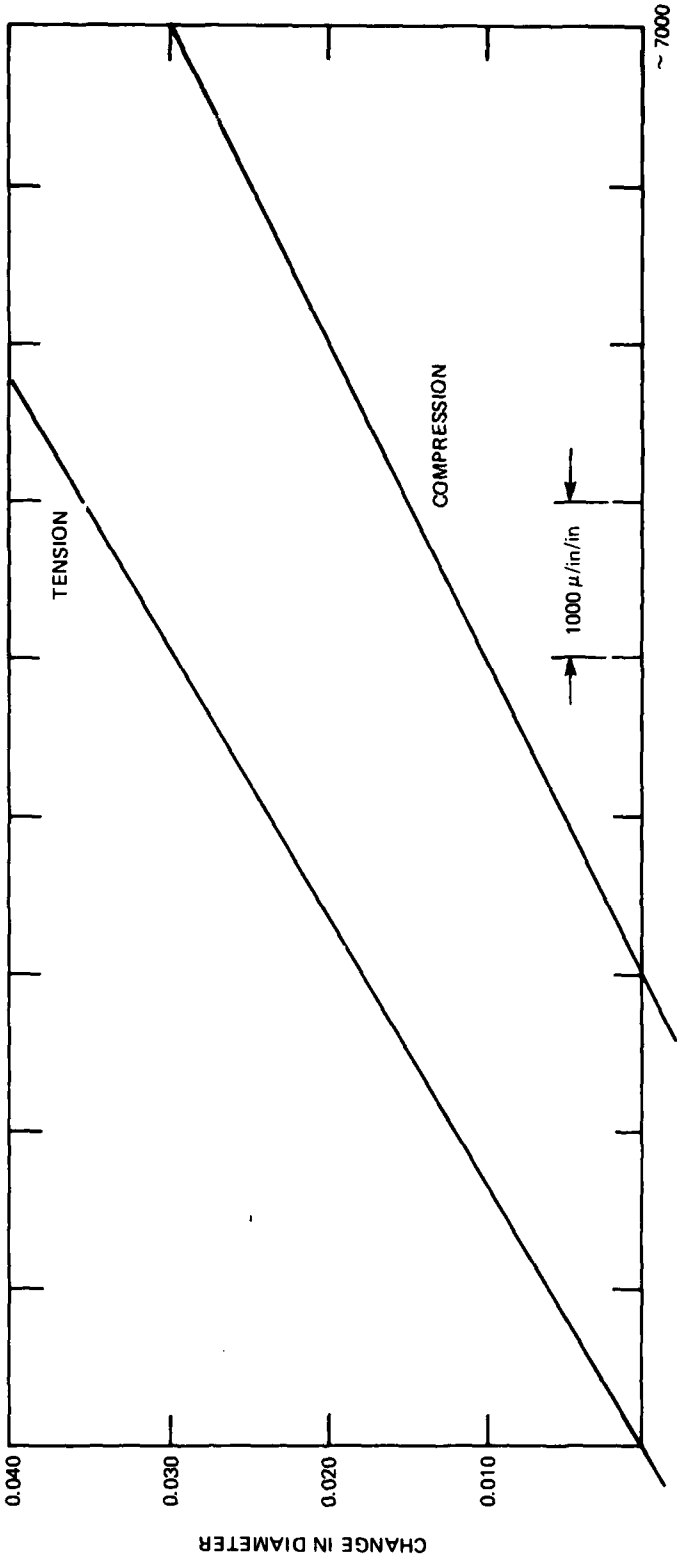

Figure 15 STRAIN vs. CHANGE IN HUB OB-FLAT PIECE SPECIMEN

With the design fixed (Drawing LA24216) special efforts were made by the test facility to raise the containment ring surrounding the flywheel in the test chamber to achieve a minimum value for "A", Figure 11. The final hub parameters were as listed in Table 2. Since they exceeded Case 10, only estimates were made of the resonant frequency. Comparing Cases 1 and 9 the difference is only in length A.

	Case 1	Case 9	Ratio
A inches	5.625	1.65	2.93 9/1
Frequency	33,600 rpm	106,700 rpm	3.15 1/9

$$\text{Frequency} \approx 1.1\ (1/A)$$

Comparing Cases 1 and 4, 2 and 5, 3 and 6, 7 and 8 the differences are in spindle length.

Case	Spindle Length (inches)	Ratio	Frequency rpm	Ratio
1	6.14	1.63	33,600	1.49
4	3.76		50,200	
2	6.14	1.63	38,900	1.43
5	3.76		56,000	
3	6.14	1.63	6,400	1.97
6	3.76		12,600	
7	6.14	1.63	28,000	1.59
8	3.76		44,600	

$$\text{Frequency} \approx 0.9\ (1/\text{spindle length})$$

Scaling the resonant frequencies of the hub from Case 10.

$$\text{Frequency} \doteq (87200)\ \frac{(6.14)}{(5.66)}\ \frac{(1.65)}{(0.99)} = 157658 \text{ rpm}$$

$$\text{Pendulum frequency} \doteq (720)\ \frac{(6.14)}{(5.66)}\ \frac{(1.65)}{(0.99)} = 1301 \text{ rpm}$$

The measured pendulum frequency was 1533 rpm indicating the scaled value was of the the correct order. To further increase the frequency the spindle-to-hub connection included a split collate to create high fixity. This was indicated as desirable by Cases 3 and 6.

4.1 ASSEMBLY SEQUENCE

The fabrication of the composite wheel and the design and fabrication of the hub were conducted in parallel, with the composite being completed well ahead of the hub. The machining of the ID and OD of the wheel was delayed until the hub tradeoffs were completed. After hub fabrication, the hub was squeezed (pre-stressed) into the wheel ID and the strain gages installed. The wheel was balanced, and its polar moment of inertia measured, after which the final gage wires were fished through the hollow hub, ready for test.

SECTION 5.0 INSTRUMENTATION

The flywheel was instrumented with strain gages to determine proof of Avco's constant stress design. Since constant stress meant stresses in both hoop and radial directions independent of radial or azimuthal positioning, six pairs of gages were placed about the top surface of the wheel: two each at one of three radial stations. Each pair measured strains in the hoop and radial directions. In addition, a single gage was emplaced on the bottom surface of one of the hub arms to monitor its displacement. The strain gage locations and strain channel designation are shown in Table 3. The companion hoop gage to Channel 11 was not connected due to limitations of the data collection system. With this exception, each hoop or radial measuremeant was duplicated at the same radial station but at another azimuth some 135 to 140 degrees away. Zero azimuth was chosen arbitrarily but aligned with the zero and 90^{o} orientation lines painted on the bottom of the wheel, which were to serve as bench marks for the pictures that were to be taken during failure. Figure 16 depicts a typical gage installation. Figure 17 is a close-up of the hub area. Micro Measurement gages EA-13-125TF-120S were used. To ensure lead wire attachment, Micro Measurement NiClad Cu Ribbon Wire GL92R-50 was bonded to the surface of the flywheel over the outer radial areas. These were connected to MM 127 AWN Nylon/Polyurethane coated wire at terminals near the ID and run down the ID of the flywheel between the hub arm pressure pads, on to the pads, and up the back surface of the arms to a terminal near the base of the arms. Since each pair of gages had two active and one common lead and there could only be 16 pickup points on the slip rings, a number of the commons had to be joined. The instrumentation was halted at this point to allow insertion of a special fixture into the hub for balancing.

TABLE 3. STRAIN GAGE LOCATIONS/ORIENTATIONS

Channel No.	Strain Direction	Radial Position	Azimuthal Position
1	Hoop	2.65 in.	90^{o}
2	Radial	2.65 in.	90^{o}
3	Hoop	5.65 in.	132^{o}
4	Radial	5.65 in.	132^{o}
5	Hoop	8.25 in.	222^{o}
6	Radial	8.25 in.	222^{o}
7	Hoop	5.70 in.	270^{o}
8	Radial	5.70 in.	270^{o}
9	Hoop	2.70 in.	315^{o}
10	Radial	2.70 in.	315^{o}
11	Radial	8.25 in.	0^{o}
12	Hub ARM	-	67.5^{o}

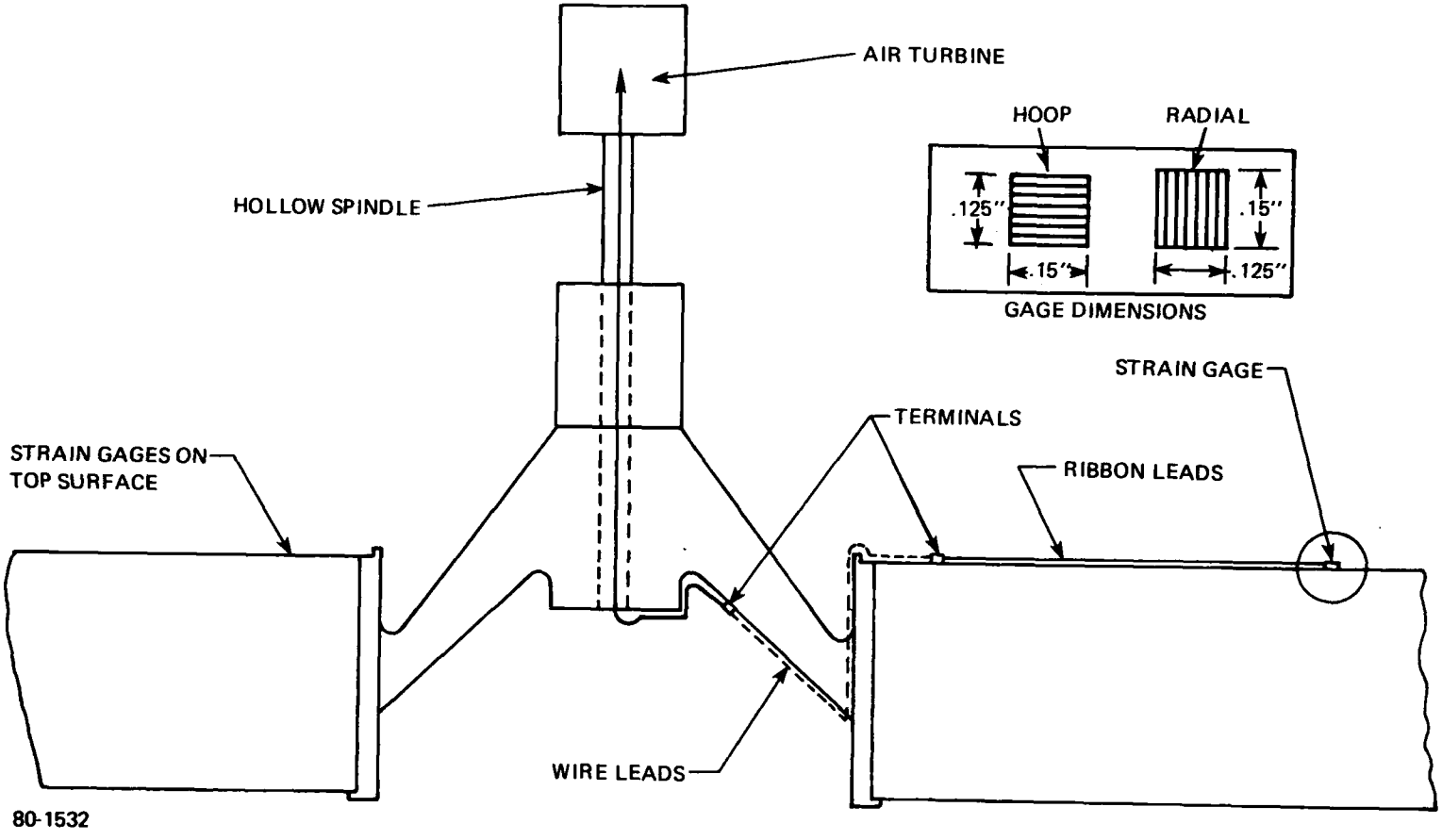

Figure 16 STRAIN GAGE SCHEMATIC

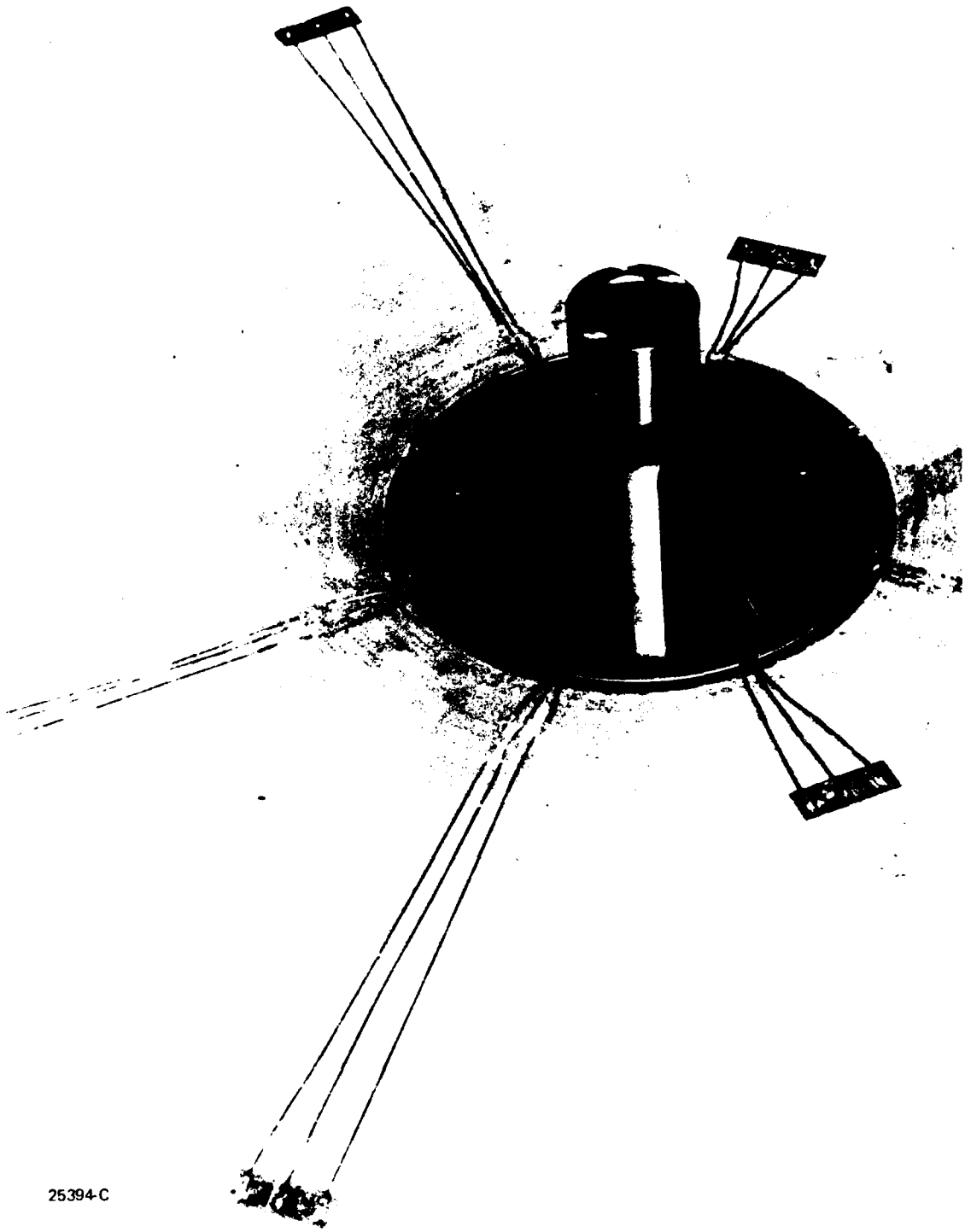

25394-C

Figure 17 STRAIN GAGE INSTALLATION NEAR HUB

After balancing, additional 127 AWG wires were fished through the hub and soldered at the terminals on the hub arms. During test setup, the gage wires were fished through the hollow spindle and connected by Naval Air Propulsion Center personnel to the recording system. The expected accuracy of the strain data was $\pm$ 150 μ strain.

In addition to the strain data, there were two speed pickups to measure turbine/flywheel speed and two orthogonal capacitance gages to monitor hub (neck) displacement. Drive and break air were recorded indicating when power to or from the turbine was applied together with chamber vacuum pressure and voltage measurements for the camera and cameral trip signal. All data were recorded vs. test time in 0.01 second intervals.

SECTION 6.0 BALANCING AND POLAR MOMENT OF INERTIA

To balance the flywheel the hub required a special fixture (Drawing LA24221) that could only be used prior to fishing the instrumentation lines through the central hole. Figure 18 shows this fixture and its assembly to the hub. The back (bottom in the spin test) face of the flywheel in its balancing configuration is shown in Figure 19. Figure 20 shows the flywheel being balanced. The metal disc was intended to be used to drive the wheel; however, in practice the torque loads were applied to the flywheel OD. After determining the balance weights needed by spinning the wheel at 400, 700 and 1500 rpm successively, the balance weights were applied similarly to the previous flywheels. Tungsten-loaded epoxy (2 gm/cc) was cast on the OD and allowed to harden overnight. The following day, the wheel was spin balanced by successively grinding down the balance weight material as with a metal wheel. The two plane maximum imbalance achieved was less than two gram-inches.

Since the hub position in the flywheel ID was mechanical (no bond) there was concern that it could be jarred out of line inadvertently so that there would be an angle between the hub axis and the flywheel axis. This would cause an undesirable wobble in the flywheel as it spun. This potential wobble was checked using deflection gages at the rim both before and after balancing (Figure 21). The apparent wobble varied azimuthally from one to three and a half mils. This method could not be used once the balancing fixture was removed to complete the instrumentation. Before removal, base data for hub alignment were taken using the special fixture shown in Figure 22 (Drawing EX26234). Two orthogonal measurements from the fixture to the spindle (which effectively extended the centerline of the hub) were made just after balancing. These measurements were duplicated just before attaching the flywheel to the turbine for spin testing.

Following removal of the balancing fixture, the flywheel with its axis vertical was suspended by a rod of known stiffness and length attached to the hub, similar to the attachment of the spindle. This is shown in Figure 23. The wheel was twisted and the period of oscillation timed to determine the polar moment of inertia; 2.33 $in\text{-}lb\text{-}sec^2$.

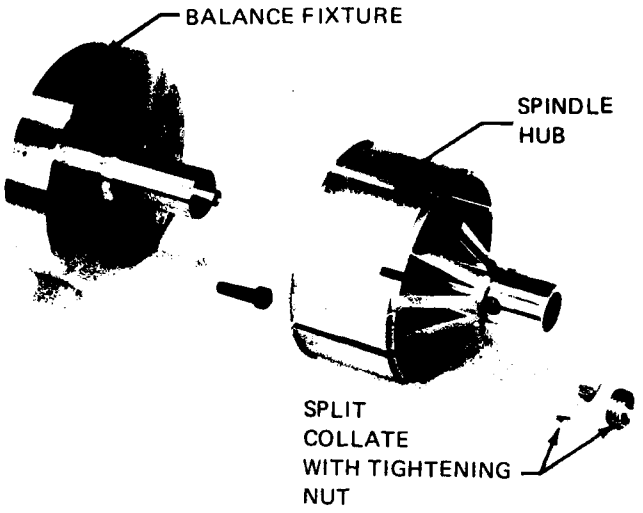

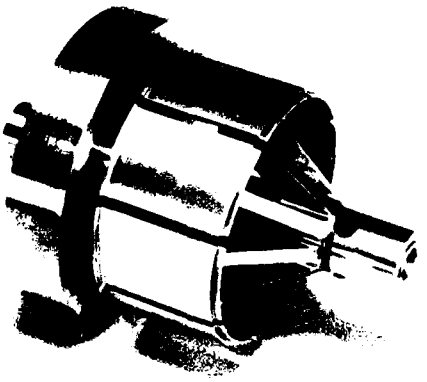

80-1533

Figure 18 BALANCING FIXTURE ASSEMBLED TO HUB

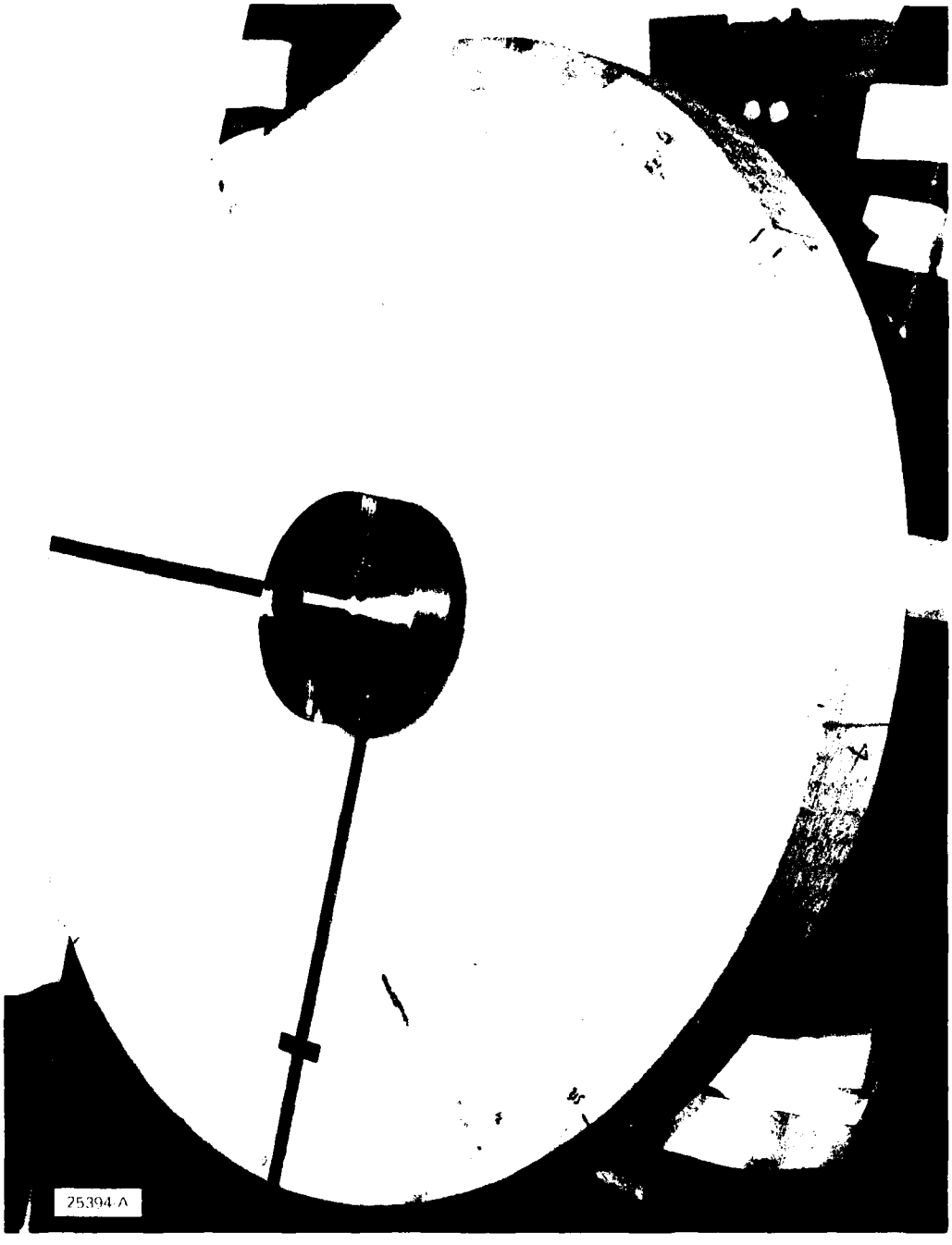

Figure 19 BALANCING FIXTURE ON FLYWHEEL

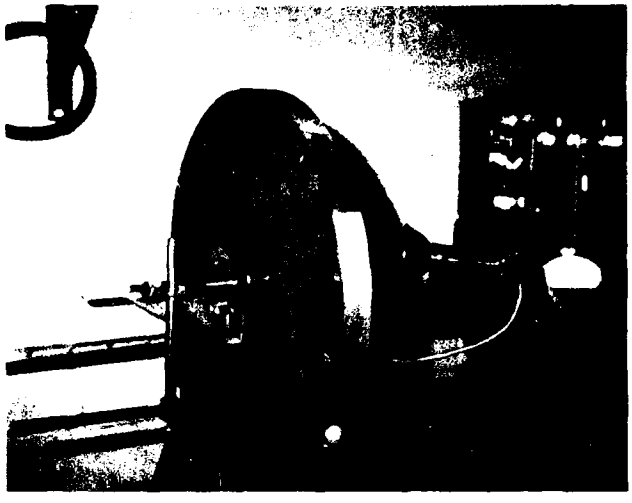

80-1534

Figure 20 FLYWHEEL BEING BALANCED

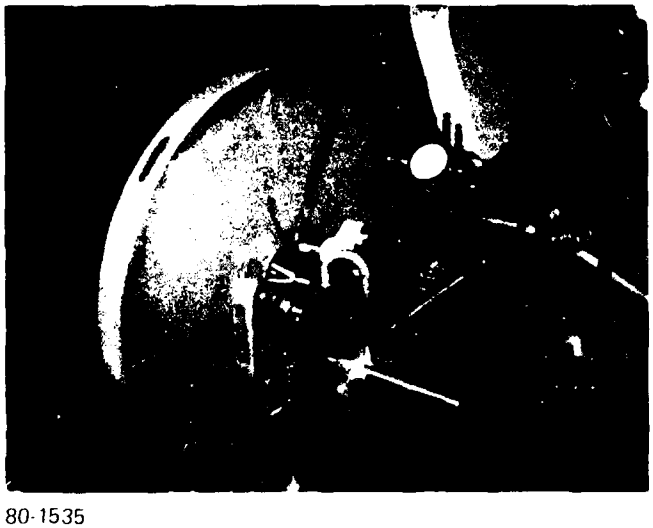

80-1535

Figure 21 ALIGNMENT (WOBBLE) MEASUREMENT

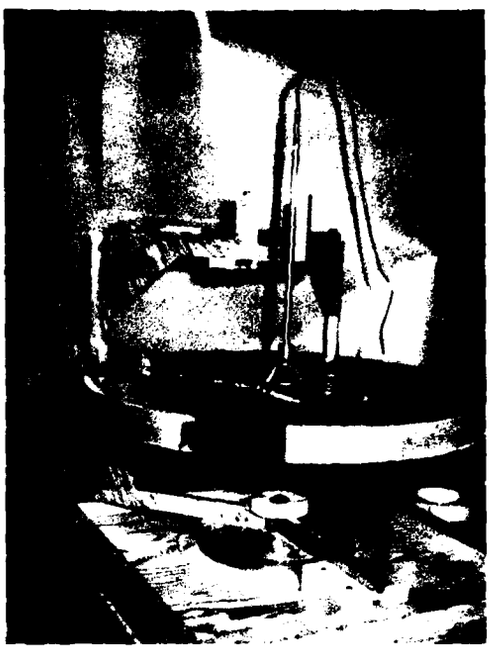

80-1536

Figure 22 HUB ALIGNMENT FIXTURE

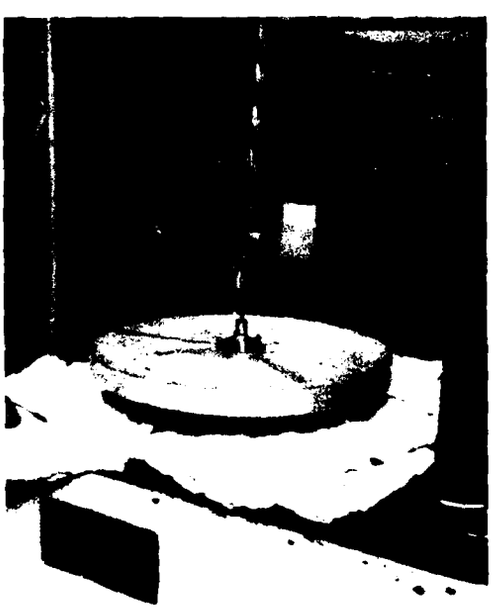

80-1537

Figure 23 POLAR MOMENT OF INERTIA MEASUREMENT

SECTION 7.0 SECOND KEVLAR FLYWHEEL TEST RESULTS

The second Kevlar flywheel was tested at NAPC, Trenton, New Jersey, over a one week period culminating in the burst test 9 July 1979. The large test chamber was used which enclosed a small chamber allowing a vacuum of approximately five microns to be drawn. A 4-inch Barbour Stockwell air turbine was used to power the spin test. Detailed description of the test set up can be found in the Phase I report. Figure 24 shows the bottom of the flywheel just before testing with the zero and 90 degree azimuthal lines. Also visable is one of the balance weights at about 180° azimuth. Figure 25 shows the flywheel about to be raised for turbine attachment.

There were two test runs. The first cycled the flywheel between 10,000 and 15,000 rpm as planned and then proceeded to spin up toward maximum burst speed. At about 24,000 rpm both speed gages failed and the test was stopped. These gages were repaired, and the second spin test to burst was conducted on 9 July 1979. Burst occurred at 38,741 rpm at an energy level of 32.3 Wh/lb. The raw data for these runs and a comparison of strain data from run to run are shown in Appendix A along with strain cycling data.

The significant test events are listed in Table 4. All events in this table occurred in the second burst run, except the initial strain data. The order of data presentation follows:

Event 1	- Constant Strain (Stress) Data
Events 2, 4, 5, 6, 7	- Hub Displacement
Event 3	- Apparent Strain Jump
Events 8, 9	- Burst Speed and Failure Analysis

TABLE 4. FLYWHEEL TEST EVENTS – SECOND RUN TO BURST

Time (sec)	Speed (rpm)	Event
*	0-16000	1. Constant Stress Design Evaluation
17.6	1533	2 Pendulum Mode, Hub Displacement 0.010 inch
256.23	31114	3. Strain Jump Channels 2, 6, 10, 11, 12
256.40	31137	4. Strain Channel 11 -1274.1 → 11511
285.79 - 285.84	33917	5. Hub Wobble Displacement to 0.050 inch
287.65	34119	6. Camera Light Trip Signal
287.98	34087	7. Strain Channel 2 699.93 → 212.33
342.58	38741	8. Burst at 32.3 Wh/lb
342.58 - 342.79	--	9. Failure Mode

*First Run Event

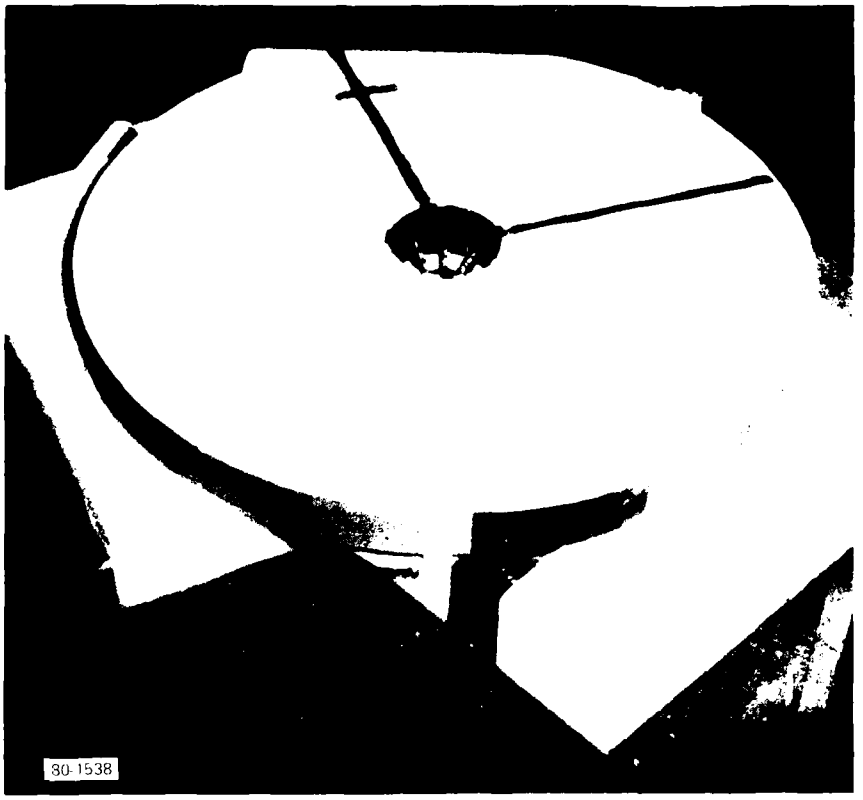

Figure 24 FLYWHEEL BOTTOM SURFACE WITH AZIMUTHAL REFERENCE LINES

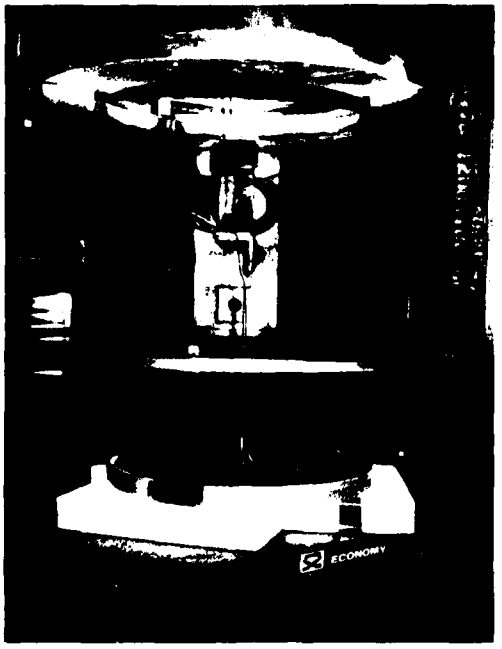

80-1539

Figure 25 FLYWHEEL BEING ASSEMBLED TO TURBINE

7.1 CONSTANT STRAIN DATA

The raw data of strain vs. speed in Appendix A for Run I were replotted and grouped according to type and radial location as follows:

Strain Measurement	Radial Location	Channel	Figure
Hoop	2.7"	1-9	26
Hoop	5.7"	*3-7	27
Hoop	8.25"	5	28
Radial	2.7"	2-10	29
Radial	5.7"	4-8	30
Radial	8.25"	6-11	31

*Run II

Strain data from Run II were plotted for Channel 3 as this channel did not operate properly during Run I. To validate this substitution, a comparison of Channel 7 (Runs I and II) is shown with Channel 3 (Run II) in Figure 32. It can be seen that there is excellent correlation between all data at each radial station independent of azimuthal position. These data are used to estimate measured strains at 16,000 rpm. This speed approximated the highest speed measured that was clear of any hysteresis effects or composite crazing effects. It was also sufficiently high to minimize the effects of hub pressure on the flywheel ID.

The hub was squeezed into the flywheel after gage installation. It was designed to expand with the inside diameter of the flywheel to maintain a positive contact throughout the test. A 2-D finite element model (radial-axial) was used to compute the pressure exerted on the ID by the hub as a function of spin rate. The results are shown in Figure 33. The pressure is nonzero at zero spin rate because of the press-fit assembly.

These hub loads must be included in any computations used for comparison with the strain gage measurements. Since these calculations were done using a 1-D radial-axisymmetric finite element code (the WHEEL code was developed at Avco), the hub loads shown in Figure 33 were averaged through the thickness and interpolated through the range 0 to 16 krpm (Figure 34).

7.1.1 Strain Data Analyses

Computations were carried out using the Avco WHEEL code (a 1-D axisymmetric finite element code) for spin rates of 16, 12, 8 and 4 krpm. The mesh and material properties were similar to those described in Reference 1, except that hub loading

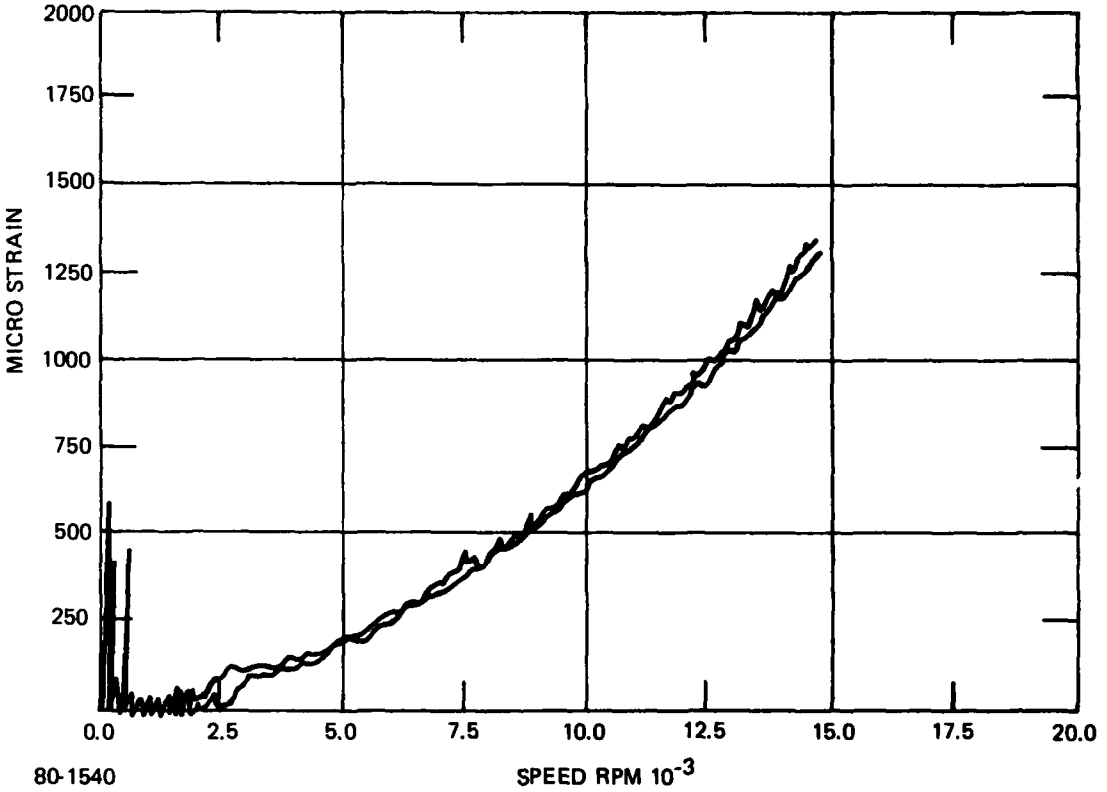

Figure 26 **CHANNEL 1 AND 9 – HOOP STRAINS AT 2.7-INCH RADIUS**

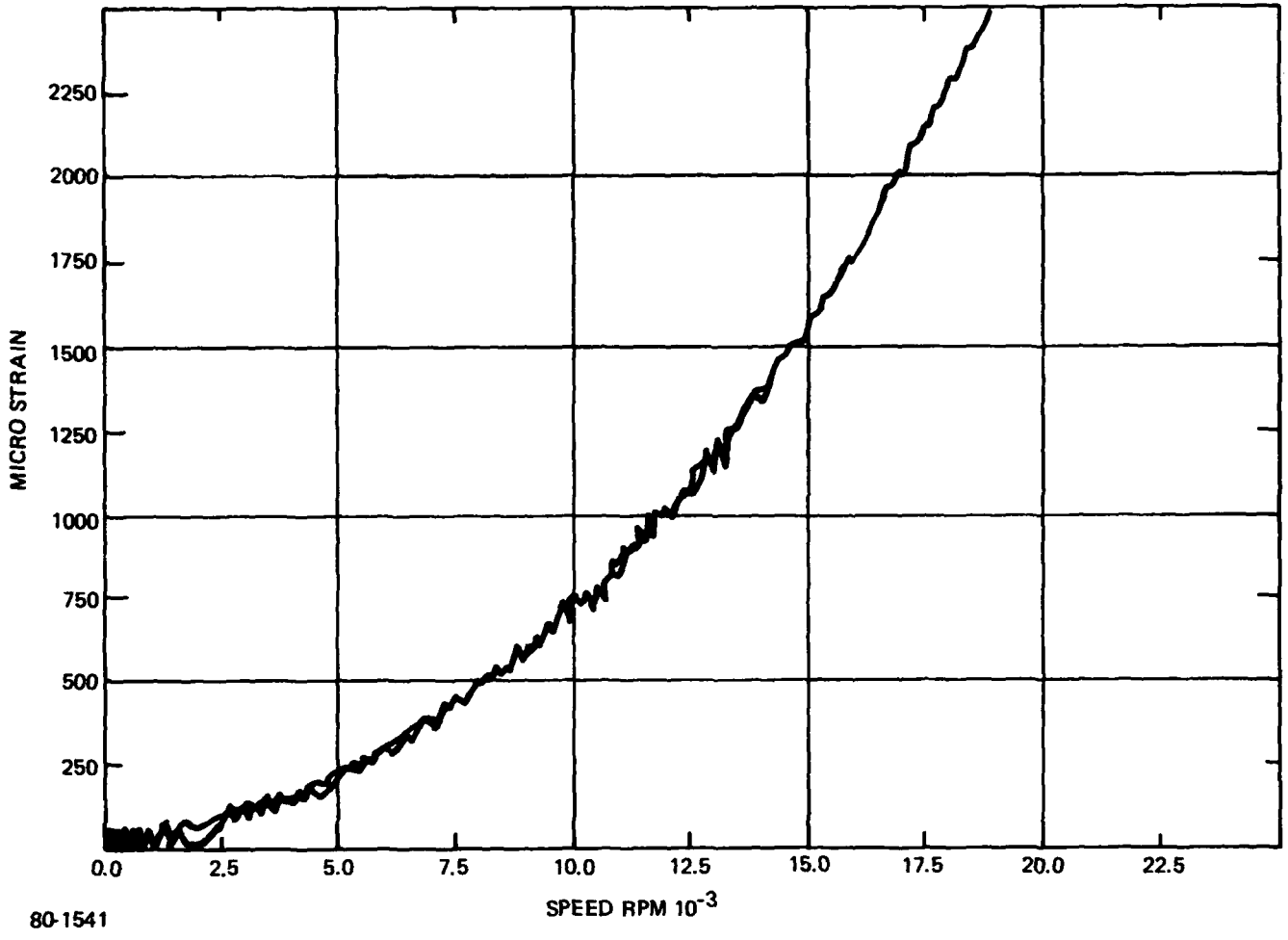

*SECOND RUN DATA

Figure 27 CHANNELS 3 AND 7 – HOOP STRAINS AT 4.7-INCH RADIUS (SECOND RUN DATA)

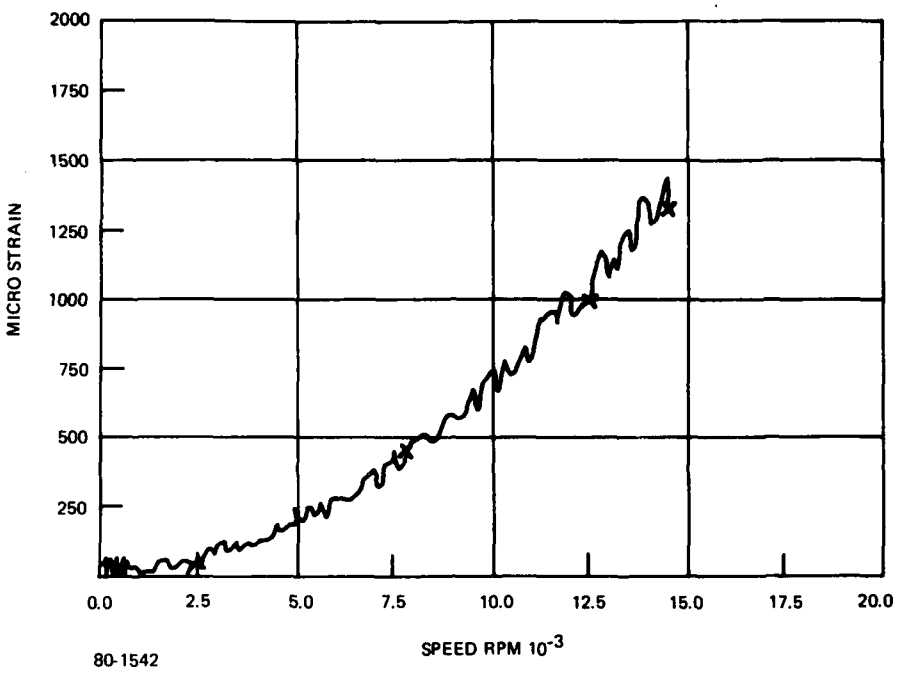

Figure 28 CHANNEL 5 – HOOP STRAIN AT 8.25-INCH RADIUS

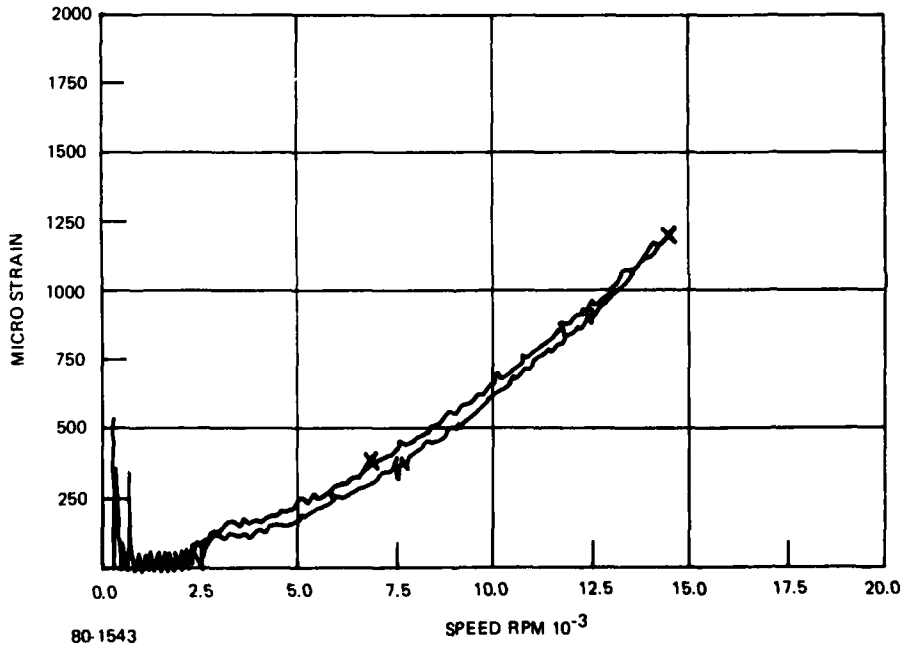

Figure 29 CHANNELS 2 AND 10 – RADIAL STRAINS AT 2.7-INCH RADIUS

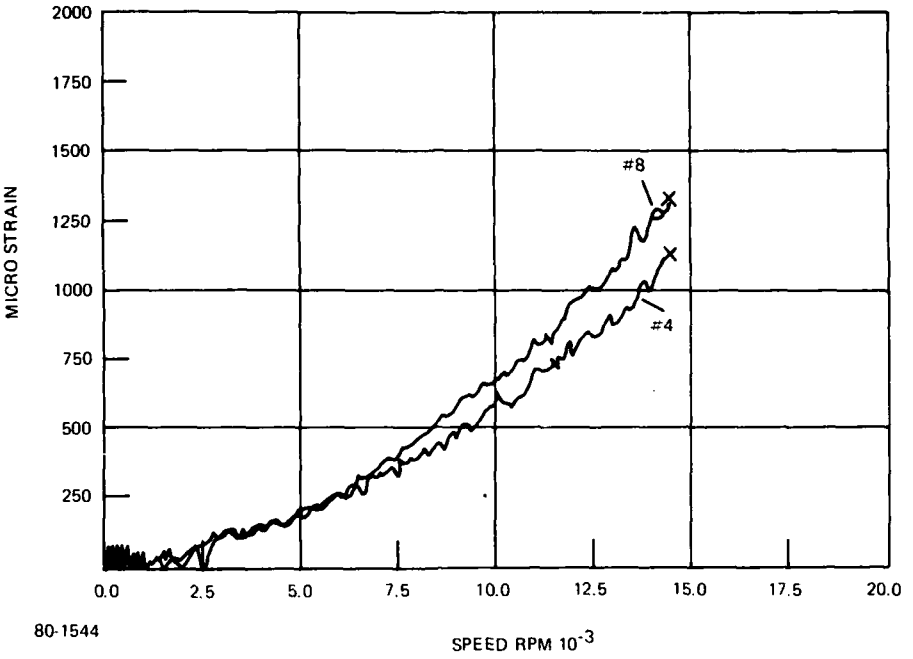

Figure 30 CHANNELS 4 AND 8 – RADIAL STRAINS AT 5.7-INCH RADIUS

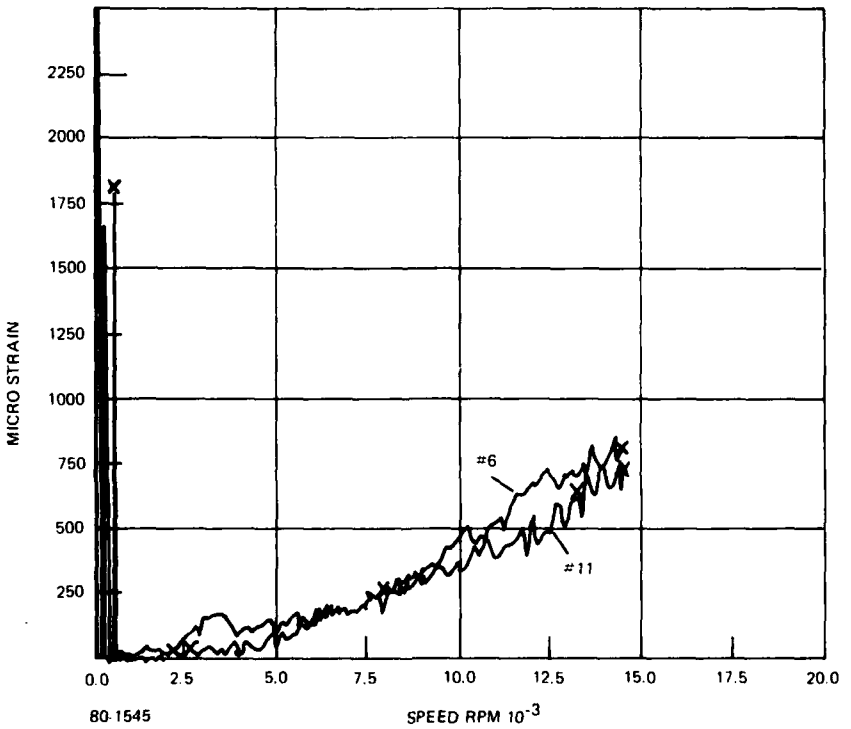

Figure 31 CHANNELS 6 AND 11 – RADIAL STRAINS AT 8.25-INCH RADIUS

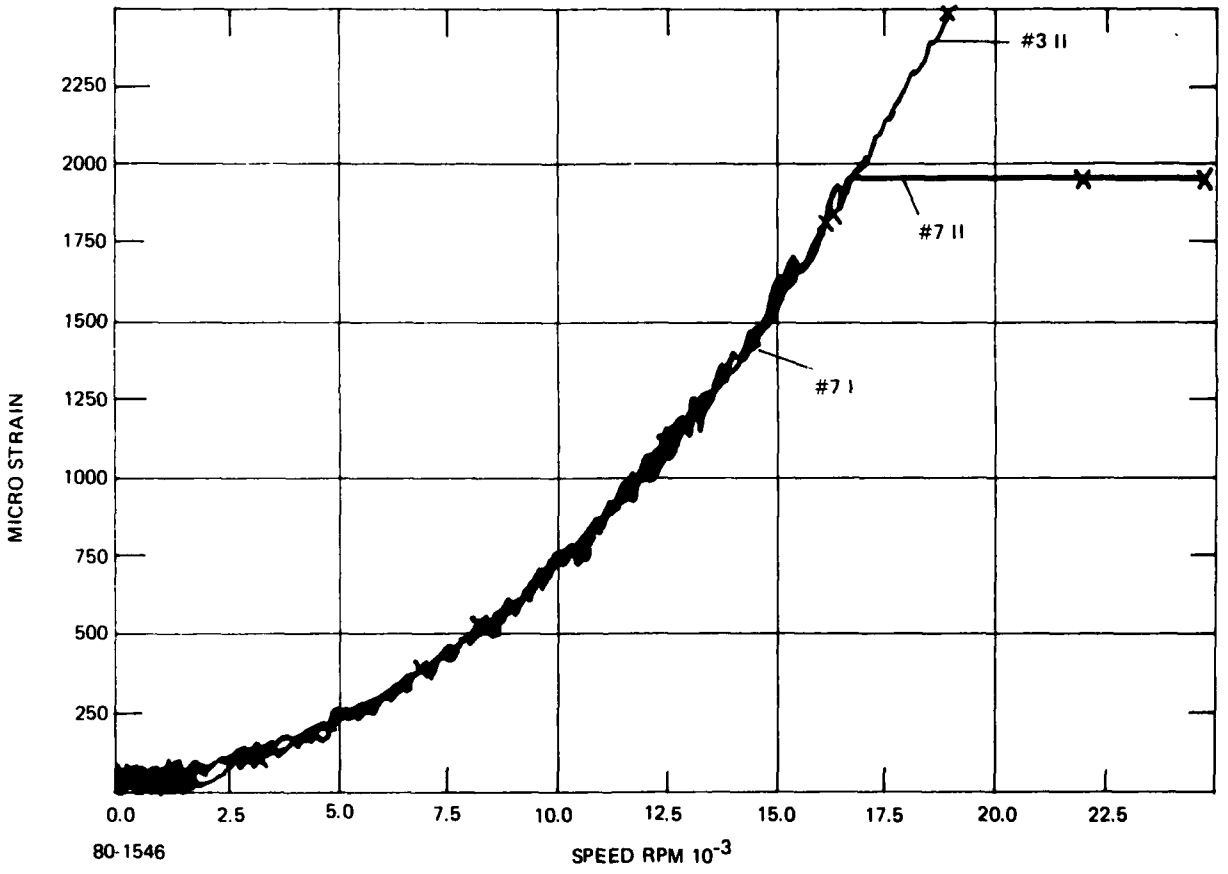

Figure 32 HOOP STRAIN DATA – STATION 2.7 INCHES (CHANNEL 7 FIRST AND SECOND RUNS; CHANNEL 3 SECOND RUN)

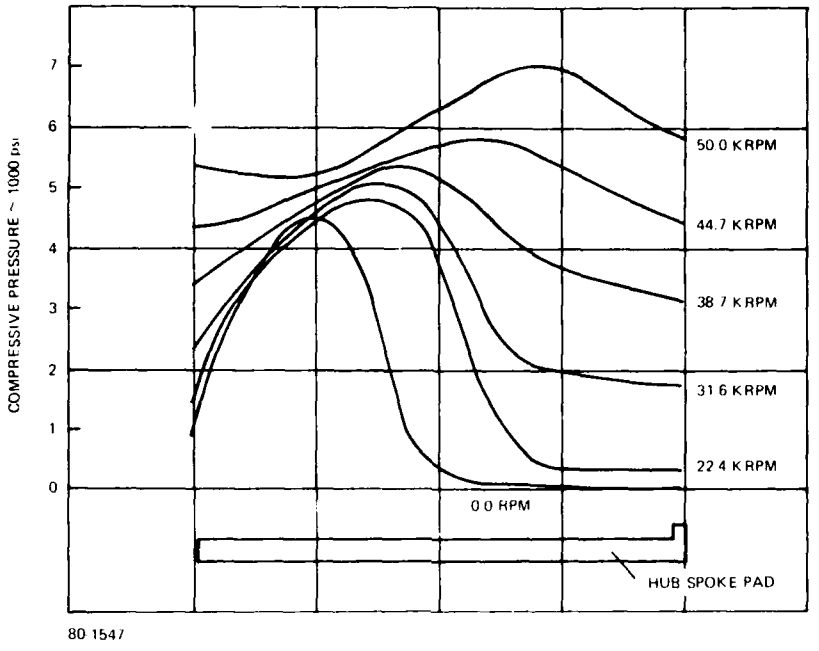

Figure 33 COMPRESSION PRESSURE BETWEEN BLYWHEEL ID AND HUB AS A FUNCTION OF SPIN RATE

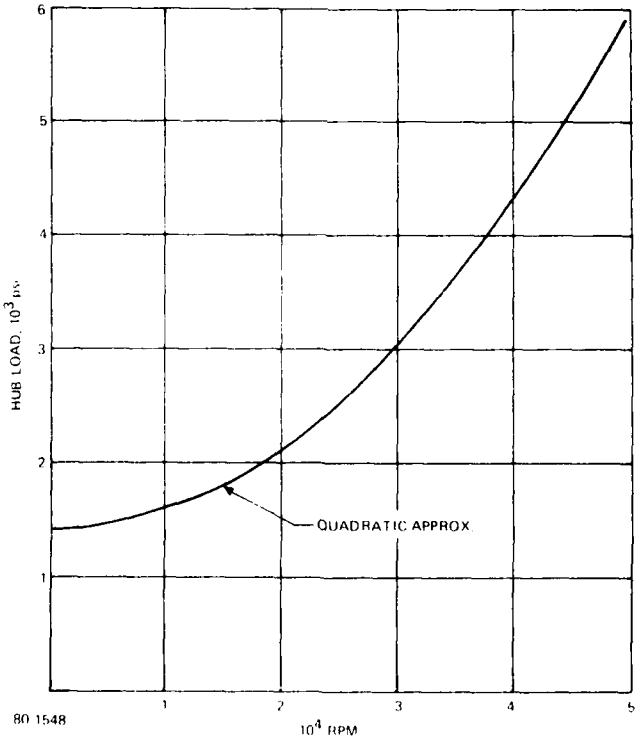

Figure 34 AVERAGE PRESSURE EXERTED BY HUB ON ID OF FLYWHEEL vs. SPEED

was included here. Because the WHEEL code allows loading via body forces only (i.e., the loading due to the radial accelerations of a spinning wheel), the hub loads were simulated by adding a ring of mass at the inner diameter. This mass had zero stiffness, and its density was tailored to give the specified hub loading at each spin rate.

Two material models were used in Reference 1: the undegraded and degraded models. The undegraded model is for the case where cross-fiber tensile strain is not yet high enough to cause crazing, so the cross-fiber stiffness is nonzero. The degraded model assumes zero cross-fiber stiffness due to the crazing caused by excessive cross-fiber strain. According to Reference 1, the cross-fiber failure strain for Kevlar is 0.22%, which should correspond to crazing at 19,275 rpm.

The flywheel is constructed of alternate layers with fibers in the hoop or radial directions. Where the 1 direction is the fiber direction and the 2 direction is the transverse (cross-fiber) direction, the material models used in the WHEEL code calculations are as follows:

weight density $\rho g = 0.0487$ lbf/in^3

undegraded stiffness:

$E_1 = 1.2 \times 10^7$ psi, $E_2 = 8 \times 10^5$ psi,

$\nu_{12} = 0.34$, $\nu_{21} = 0.0227$

degraded stiffness:

$E_1 = 1.2 \times 10^7$ psi, $E_2 = 0$,

$\nu_{12} = \nu_{21} = 0$

Results of these calculations at radii of 2.7, 5.7 and 8.25 inches and for spin rates up to 16 krpm are reported in Table 5. Hub loads are as shown in Figure 34. Calculations were carried out for both the degraded and undegraded properties; the strains, strain ratios and fiber direction stresses in the hoop and radial layers are reported. Note that the maximum strains at 16 krpm are all below the critical transverse strain of 2200 microstrain, so it is expected that crazing does not occur for 16 krpm and below. The undegraded material model should, therefore, give the best correlation with the measured strains.

TABLE 5. KEVLAR FLYWHEEL SPIN SIMULATION VIA 1-D AXISYMMETRIC FINITE ELEMENT CODE STRAINS AND STRAIN RATIOS

Strain Station (inches)	Speed (krpm)	ε_θ^d	ε_r^d	$\frac{\varepsilon_\theta^d}{\varepsilon_r^d}$	σ_θ^d	σ_r^d	ε_θ^u	ε_r^u	$\frac{\varepsilon_\theta^u}{\varepsilon_r^u}$	σ_θ^u	σ_r^u
2.7	4	160	-56	-2.86	1.92	-0.67	164	-58	-2.83	1.97	-0.65
	8	411	224	1.83	4.94	2.62	423	176	2.40	5.17	2.25
	12	831	674	1.23	10.0	8.1	855	565	1.51	10.5	7.1
	16	1419	1313	1.08	17.0	15.8	1460	1110	1.32	18.0	13.8
5.7	4	100	78	1.28	1.20	0.94	97	65	1.49	1.19	0.82
	8	365	353	1.03	4.38	4.24	347	303	1.15	4.29	3.76
	12	808	811	1.00	9.7	9.7	765	698	1.10	9.4	8.7
	16	1427	1451	0.98	17.1	17.4	1350	1251	1.08	16.7	15.5
8.25	4	95	85	1.12	1.13	1.02	87	56	1.55	1.06	0.70
	8	362	356	1.02	4.34	4.27	327	240	1.36	4.02	2.99
	12	807	807	1.00	9.7	9.7	728	546	1.33	9.0	6.8
	16	1431	1438	1.00	17.2	17.3	1289	974	1.32	15.9	12.1
2.7	0	Hub Loads					78	-136			
5.7	0						13	-14			
8.25	0						6	-5			

Notes:
1. ε_θ and ε_r microstrain.
2. σ_θ and σ_r are fiber direction stresses in the hoop and radial layer given in ksi (10^3 psi).
3. Superscript "d" indicates degraded stiffness properties.
4. Superscript "u" indicates undegraded stiffness properties.

The last group of figures in Table 5 are the strains produced by the initial hub loading at zero spin rate. They were calculated by using a low spin rate (1 radian/sec) and a thin ring at the inside diameter with a high density and zero stiffness. The spin loads induced by the flywheel are essentially zero when compared to the load generated by this ring. The strains in the flywheel are thus generated by the hub load alone. Because of the zero spin rate and relatively low value of the hub stress, strains were generated using the undegraded material properties.

The details of the calculation of the density of this ring of material are as follows: the axial height (h) of the ring and the flywheel are equal; the ring thickness (t) is equal to the first radial interval of the finite element mesh, which starts at the internal radius R_I = 1.625 in. The radial stress generated by the ring is thus its areal density multiplied by its radial acceleration. Where ρ is density and g is gravitational acceleration,

$$\sigma_r = \rho t \omega^2 R_I,$$

$$\rho g = \frac{\sigma_r \cdot g}{t \omega^2 R_I} = \text{weight density of ring material}$$

(The WHEEL code uses weight density.) For the case discussed previously,

hub stress σ_r = 1431 psi

g = 386.4 in/sec^2

t = 0.025 in

ω = 1 rad/sec

R_I = 1.625 in

ρg = 1.36 x 10^7 lbf/in^3

The density of the ring material drops off rapidly as the spin rate increases. Weight densities corresponding to hub loads over the range of spin rates are tabulated in Table 6. The hub loads are taken from Figures 33 and 34.

The strains induced by the zero spin rate hub load are important because the strain gages were mounted on the flywheel after the hub was press-fit into place. The actual strains were thus those recorded by the strain gages plus those due to the initial hub loading. Figure 35 shows the effect of the hub as a function of spin in terms of $\varepsilon_r/\varepsilon_\theta$. It is seen that at 16,000 rpm, just above the peak cycling speed, the hub effects are small. It is at this speed that measured-to-predicted strain comparisons were made.

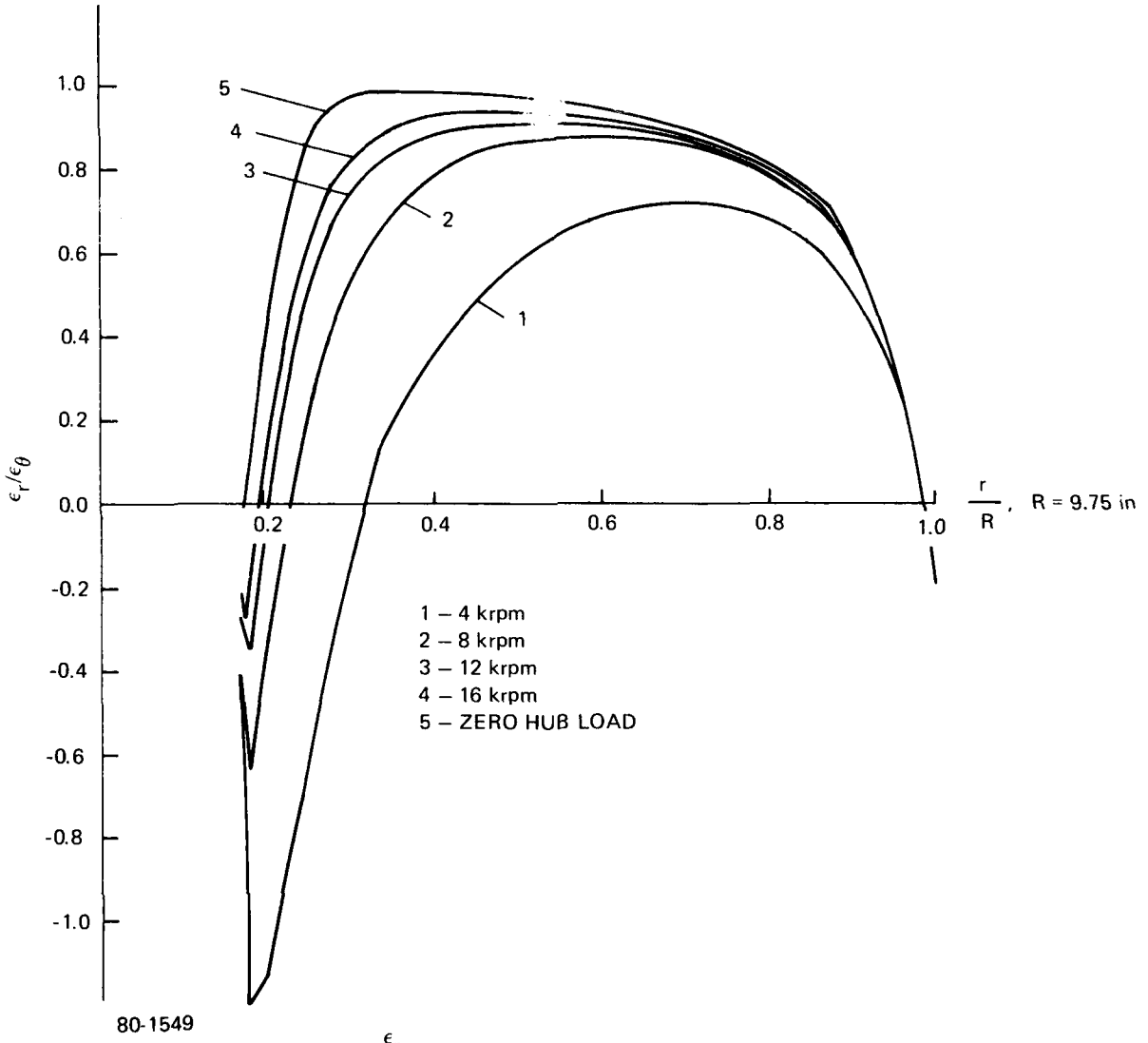

Figure 35 COMPUTED $\frac{\epsilon_r}{\epsilon_\theta}$ AS A FUNCTION OF RADIUS AND SPIN RATE WITH HUB PRELOAD

TABLE 6. INNER RING HUB LOAD SIMULATION

Spin Rate (krpm)	w (rad/sec)	Hub Stress σ_r (psi)	Ring Wt. Density ρg (lbf/in^3)
0	0	1431	1.4×10^7
4	419	1456	79.0
8	838	1539	21.0
12	1257	1682	10.1
16	1676	1884	6.4
22.4	2346	2331	4.0
31.6	3309	3190	2.8
38.7	4053	4191	2.4
44.7	4681	5071	2.2
50.0	5236	5994	2.1

Table 7 compares the predicted strains for 16,000 rpm to measured strains from Figures 26 through 31 extrapolated to 16,000 rpm. The near constant ratio of predicted to measured strains for the first two stations indicates that a gage factor and/or modulus correction is appropriate. Such gage factor corrections for composite materials have been found necessary for precise data and can only be determined by static test calibration using similar composite construction. This was not practicable for this test. Assuming a correction factor of 0.88, the variances are within 3 percent. If the same correction factor is applied to the 8.25-inch station, the deviation averages 15 percent. Table 7 also shows predicted and measured values of $\epsilon_r/\epsilon_\theta$. The same pattern exists; excellent correlation for the first two stations with some drop off in correlation at 8.25 inches.

The same strain data are treated another way. A comparison of the stress (or strain) state is made by normalizing the measured and predicted values to the 2.7-inch station value. This essentially introduces the above correction factor and presents a pattern of just how constant a strain was produced over the flywheel. The data are shown in Table 8 and plotted in Figure 36. The correlation for the first two stations is excellent, but again there is a variation at station 8.25 inches. If the predicted ratio is applied to the measured values, it is found that the measured hoop strain is 192 μ strain too high and measured radial strain, 178 μ strain too low. Since the function of the radials is to equalize the hoop strains, the drop off in radial strain (load) and increase in hoop strain (load) was suspected

TABLE 7. SUMMARY OF COMPARATIVE STRAIN (ε) DATA AT 16,000 RPM

Classification		Radial Strain Gage Station					
		2.7"		5.7"		8.25"	
		ε	$\frac{\varepsilon PRED}{\varepsilon MEAS}$	ε	$\frac{\varepsilon PRED}{\varepsilon MEAS}$	ε	$\frac{\varepsilon PRED}{\varepsilon MEAS}$
Hoop (ε_θ)	Predicted	1460	0.89	1350	0.92	1289	0.78
	Measured	1648		1468		1656	
Radial (ε_r)	Predicted	1110	0.86	1251	0.86	974	1.05
	Measured	1295		1454		932	
$\frac{\varepsilon_r}{\varepsilon_\theta}$	Predicted	0.76		0.93		0.76	
$\frac{\varepsilon_r}{\varepsilon_\theta}$	Measured	0.79		0.99		0.56	

TABLE 8. RELATIVE STRAIN DISTRIBUTION OVER FLYWHEEL AT 16,000 RPM*

Measured Strain Uncorrected			
Radial Station	2.7	5.7	8.25
Hoop	1545	1759	1648
Normalized to 2.7 Station	1	1.14	1.07
Radial	1475	1472	937
Normalized to 2.7 Station	1	1.00	0.64
Predicted Strain Undegraded Material No Hub Corrections			
Radial Station	2.7	5.7	8.25
Hoop	1357	1333	1281
Normalized to 2.7 Station	1	0.98	0.94
Radial	1290	1269	981
Normalized to 2.7 Station	1	0.98	0.76

*No Hub Effects

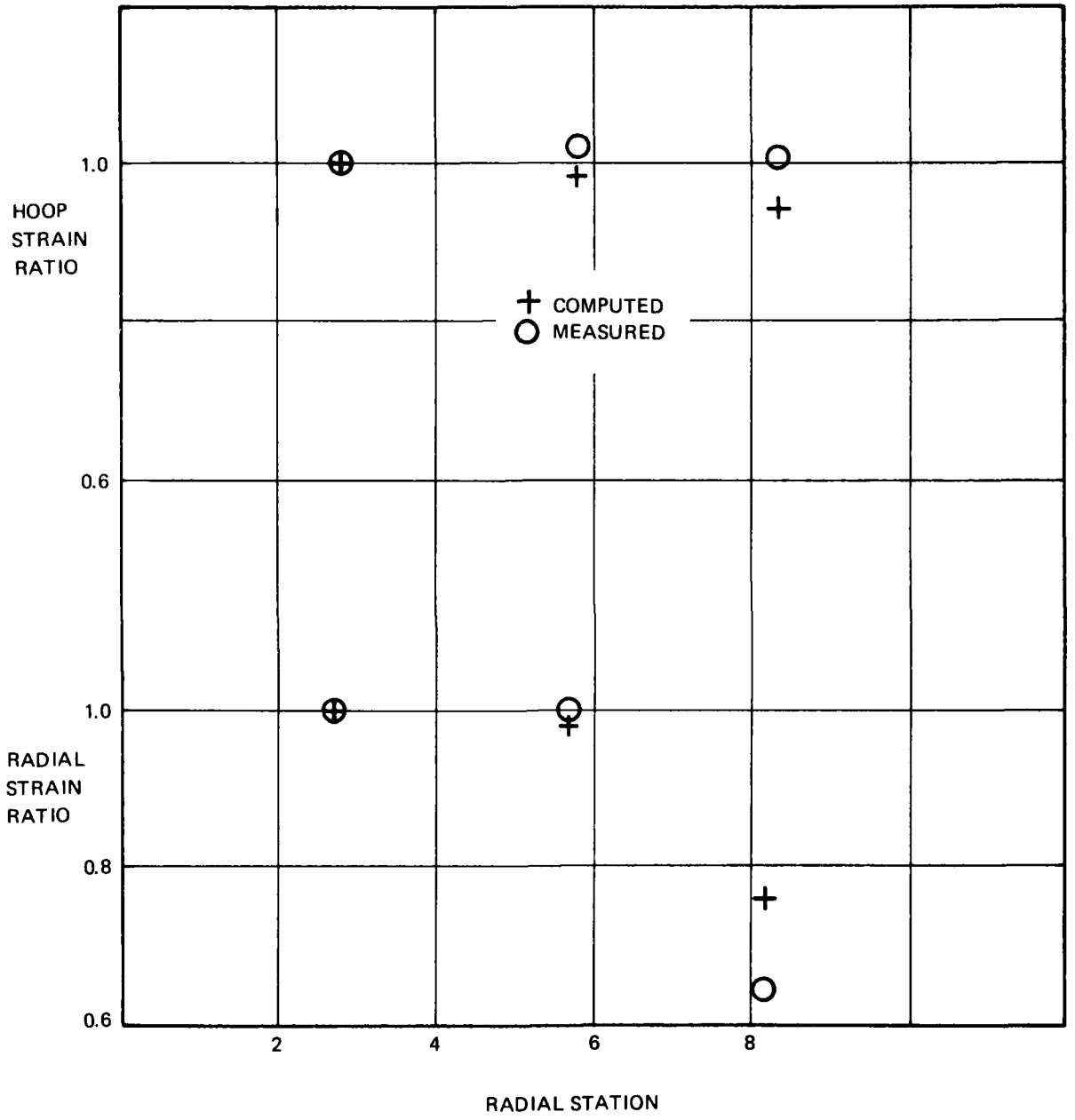

80-1550

Figure 36 RELATIVE STRAIN DISTRIBUTION OVER FLYWHEEL

of being systematic. First, to put the variations in perspective, the channels in question, 5, 6 and 11, did exhibit more noise than the others; an error band of at least ± 150 μ strain is indicated. Secondly, if the radial spacing is compared with strain gage size, (Figure 37) it suggests that the outboard gage position had a 2/3 chance of being over an unsupported hoop layer, and, as such, they may have had different effective gage factors than the inboard channels. For the same reason the gage factors at the 8.25-inch station may not have been same for both hoop to radial measurements.

To investigate the variance a variation in radial width outboard of station 5.7 inches was considered. The radial width was reduced 10%, but while in the right direction only a 1% strain was affected. Figure 38, which also evaluated radial width variations, shows a rapid drop in stress just outboard of station 8.25 inches but no increase in hoop strain. There is the suggestion that if the strain gages were located between radial supports then there could be a local increase in hoop strain due to a bowing out or "catenary" deflection. To account for the increased hoop strain the deflection would have to be about 1.5 mils, a plausible value. This would account, via Poissons ratio, for only a 65 μ strain decrease in radial strain, leaving a 113 μ strain to be accounted for. The deviations from the ideal are now within the accuracy of the data. It is suggested that a combination of the above explains the variances at the 8.25 inch station.

For completeness, it was decided to investigate the use of single parameter strain measure for the comparison of measurements to computations. One simple way was to use the square root of the sum of the squares of the strains:

$$\bar{\varepsilon}_1 = \left(\varepsilon_r^2 + \varepsilon_\theta^2\right)^{\frac{1}{2}}$$

However pleasing the results may be, this is not correct for orthotropic construction. A method which may be more physically reasonable is to look at the linear elastic strain energy density (V) in the flywheel as a function of radius, considering the radials to be spread evenly over the circumference. For plane stress ($\sigma_z = 0$) and axial symmetry;

$$\sigma_r = \frac{1}{\lambda}\left[E_r\varepsilon_r + \nu_{r\theta}E_\theta\varepsilon_\theta\right], \quad \lambda = 1 - \nu_{r\theta}\nu_{\theta r}$$

$$\sigma_\theta = \frac{1}{\lambda}\left[E_\theta\varepsilon_\theta + \nu_{\theta r}E_r\varepsilon_r\right],$$

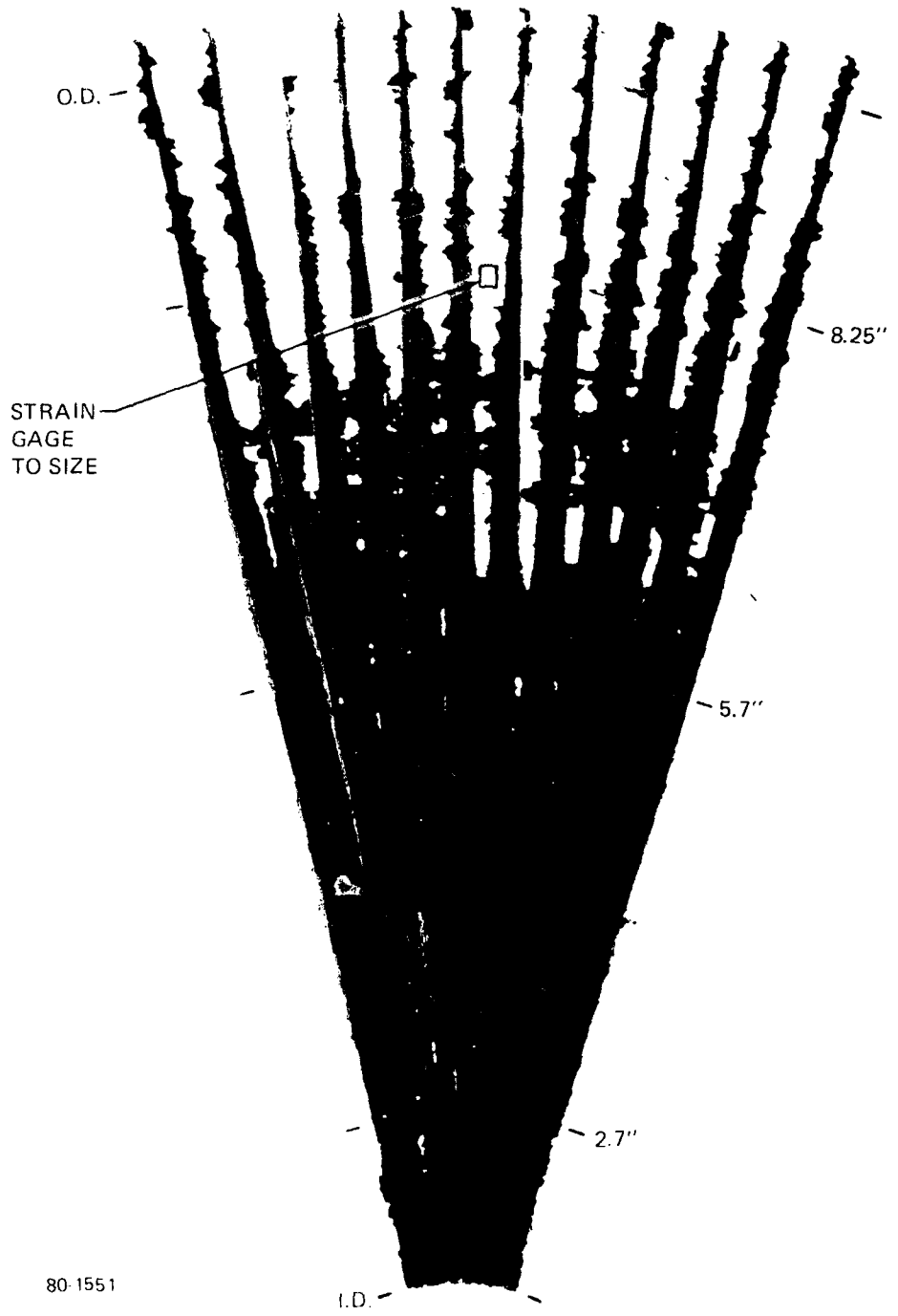

Figure 37 RADIAL SPACING vs. RADIAL STATION

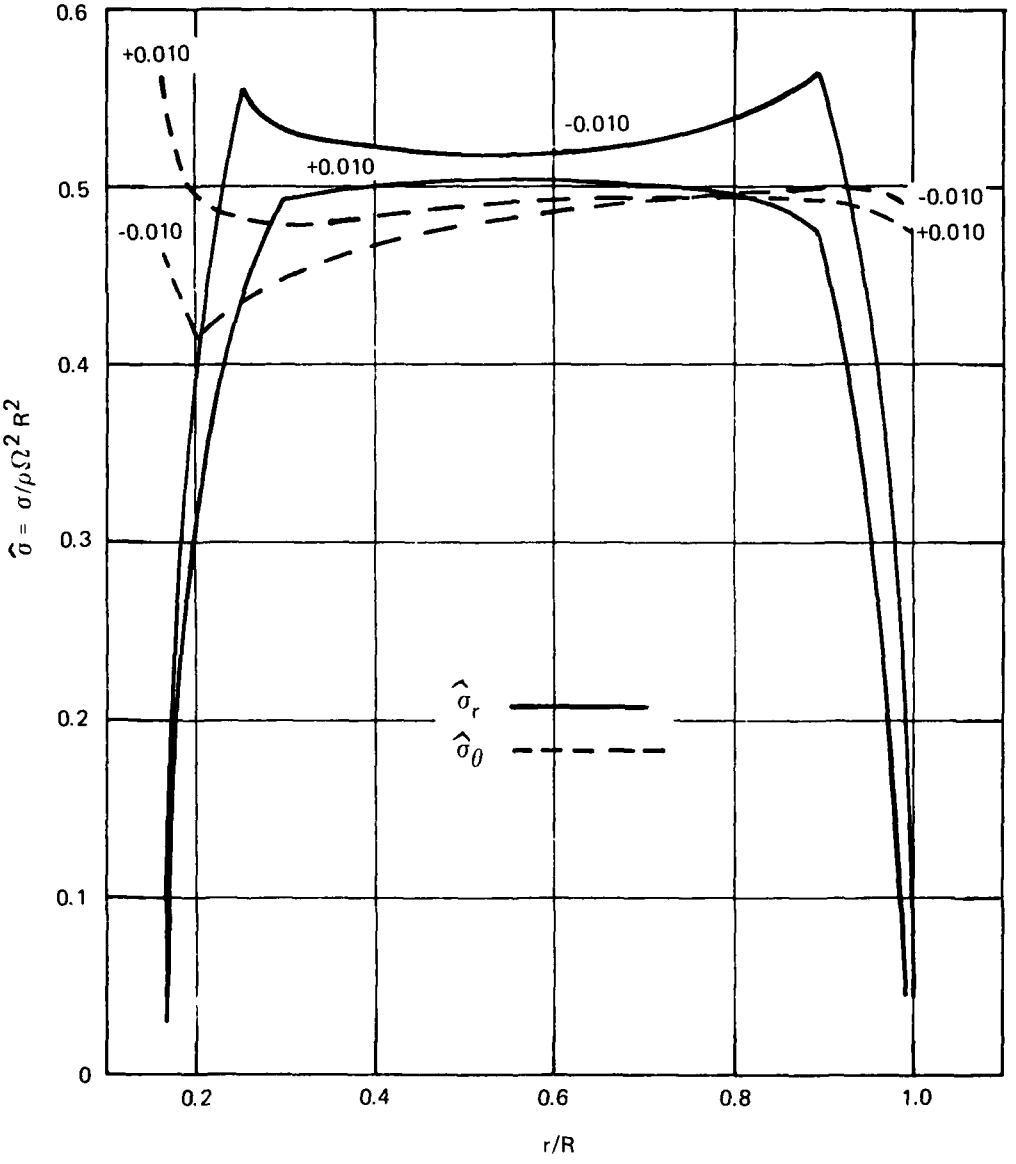

Figure 38 STRESS DISTRIBUTION vs. RADIAL-WIDTH VARIATIONS FOR +0.100 AND -0.010 INCH CHANGES IN RADIAL WIDTH

$$V = \tfrac{1}{2}\sigma_{ij}\varepsilon_{ij} = \frac{E_\theta}{2\lambda}\left(\varepsilon_r^2\,\frac{E_R}{E_\theta} + \varepsilon_\theta^2 + 2\nu_{r\theta}\varepsilon_r\varepsilon_\theta\right)$$

$$\nu_{\theta r} = \frac{-\varepsilon_r}{\varepsilon_\theta} \quad \text{for } \sigma_r = \sigma_z = 0,\ \sigma = \sigma_\theta$$

$$\nu_r E_\theta = \nu_{\theta r} E_r$$

Consider a tensile coupon with orthogonal hoop and radial materials of equal fiber percentage and different thicknesses (t_o, t_r). It can be shown, by applying σ_θ, setting the average transverse stress to zero, and constraining the layers to move together (equal strains), that

$$\nu_{\theta r} = \frac{\nu_{12}\left(1 + \dfrac{t_r}{t_\theta}\right)}{1 + \dfrac{E_1\,t_r}{E_2\,t_\theta}}$$

The subscripts 1 and 2 refer to the fiber and transverse directions of the laminate; E_1, E_2, and V_{12} are independent of thickness.

Using the data in Table 7 and Figure 39, where average thickness is proportional to fiber direction modulus, the quantities in Table 9 were calculated. Since the strain energy density is a function of the strain squared, the square root of the ratio of strain energy densities is included in the last column as being more equivalent to the ratio of the $\bar{\varepsilon}_1$.

The $\bar{\varepsilon}_1$ ratio gives what is at first glance the more satisfying numbers, since they vary the least with radius. We feel, however, that this ratio masks the real effect of construction on the strain gage behavior, and that the ratios of strain energy densities are more realistic. Note that

$$\bar{\varepsilon}_1^2 = 2V/E_\theta \text{ when } E_r = E_\theta \text{ and } \nu_{\theta r} = 0;$$

i.e., when the composite is a fiber net with equal fiber volume in the r and θ directions.

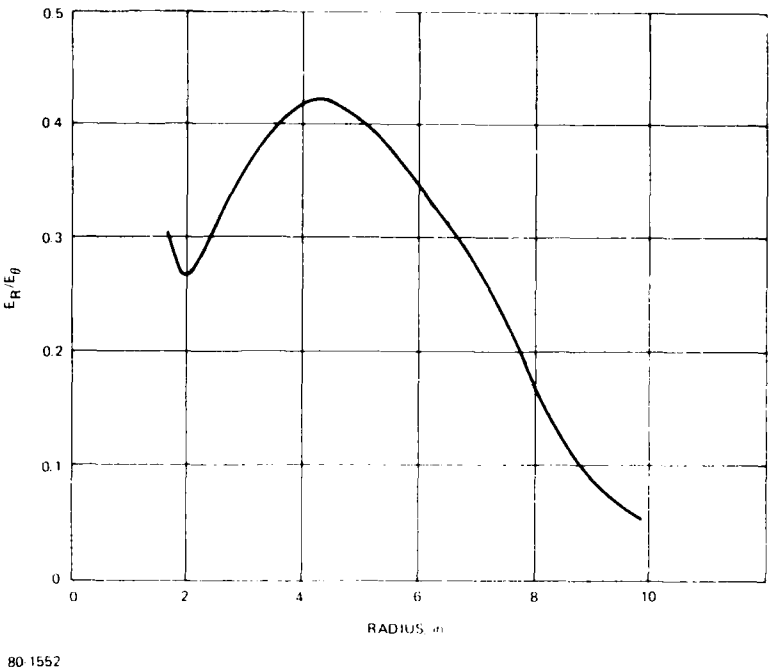

Figure 39 PETAL DESIGN – RELATIVE STIFFNESS vs. RADIUS

TABLE 9. STRAIN ENERGY DENSITY

r	Strain Type	microstrain ε_r		$\bar{\varepsilon}_1 = \sqrt{\varepsilon_r^2 + \varepsilon_1^2}$	$\frac{\bar{\varepsilon}_1 \text{ (pred)}}{\bar{\varepsilon}_1 \text{ (meas)}}$	$t_r/t_{..}$	ν_r	$1/E_{..} V, \times 10^{-6}$	$\frac{V \text{ (pred)}}{V \text{ (meas)}}$	$\sqrt{\frac{V \text{ (pred)}}{V \text{ (meas)}}}$
2.7"	Pred.	1110	1460	1834	0.875	0.333	0.0756	1.314	0.776	0.881
	Meas.	1295	1648	2096				1.694		
5.7"	Pred.	1251	1650	1841	0.891	0.366	0.0716	1.244	0.817	0.904
	Meas.	1454	1468	2066				1.523		
8.25"	Pred.	974	1289	1616	0.850	0.125	0.1330	0.913	0.628	0.792
	Meas.	932	1656	1900				1.454		

7.2 HUB ARM STRAIN

Channel 12, Figure 40, shows the hub arm strain up to 31,114 rpm. The strain before the strain jump (Event 3) was 5076 μ strain. It was not practical to calibrate the hub radial deflection vs. arm strain. However, using data from flat piece simulations (Figure 15) an estimate of 0.0124-inch radial growth attended an arm strain of 5076 μ strain. Extrapolating this approximate value to that at the predicted burst speed of 52,770 rpm, the radial growth would be 0.036 inch vs. the predicted 0.026. This increased growth indicates the Kevlar composite had a lower modulus by a factor of 0.72 than that used in predictions which was based on unidirectional tests, and/or there was some additional local strain due to the hub pressure on the ID. If one accepts the ratio of predicted to measured strains of 0.88, this calculates to a local radial crushing at the ID of 0.0024 inch, a plausible value.

7.3 HUB DISPLACEMENT (EVENTS 2, 4, 5, 6, 7)

Figure 41 is a plot of the hub (neck) displacement vs. speed. There are two large amplitudes observed. The first at 1533 rpm (Event 2) is clearly, from its shape, the first pendulum mode which was estimated from the hub resonant frequency trades to be 1301 rpm. The fact that the scaled frequency estimate for this mode was low is an indication that the next scaled resonance at 157,700 rpm was conservative; the second resonance point was well beyond the burst speed.

The second large displacement (hub wobble) at 33,917 (Event 5) is clearly, from its shape, not a natural resonance point. There was a near order of magnitude increase in amplitude in 0.05 seconds. Some trauma must have occurred which caused the wobble and most likely dislodged a small piece of the flywheel, which triggered the camera light (Event 6) less than two seconds later. The pictures taken at Event 6 show an undisturbed wheel rotation. The two nearest events which were considered were Events 4 and 7. Both involved large changes in strain signal over a short time. The first showed an abrupt (0.01 second) change from -1274.1 to 11511 μ strain but was some 20 seconds prior to the wobble. It was believed that this was the failure of the strain gage circuitry. Calculations quickly showed that loss of the gage and even some leads would not cause the resulting increased hub displacement. The second, two seconds after wobble, exhibited a slower strain change (over tenths of seconds). No strain gage removal was suggested here, so neither Event 4 or 7 were considered important to the hub wobble.

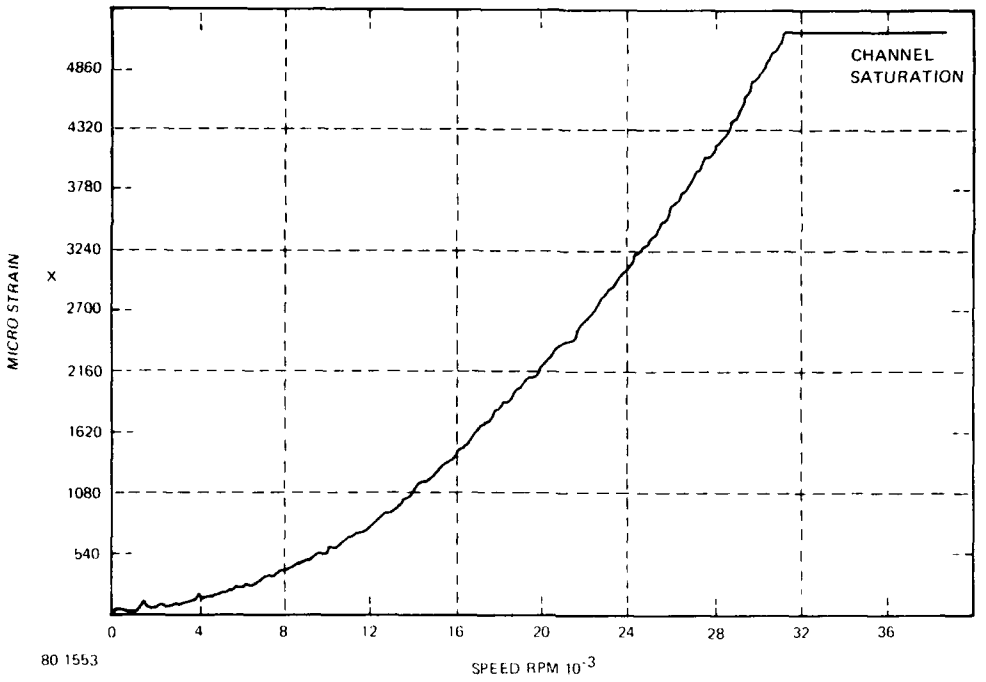

Figure 40 HUB STRAIN vs. SPEED – SECOND RUN

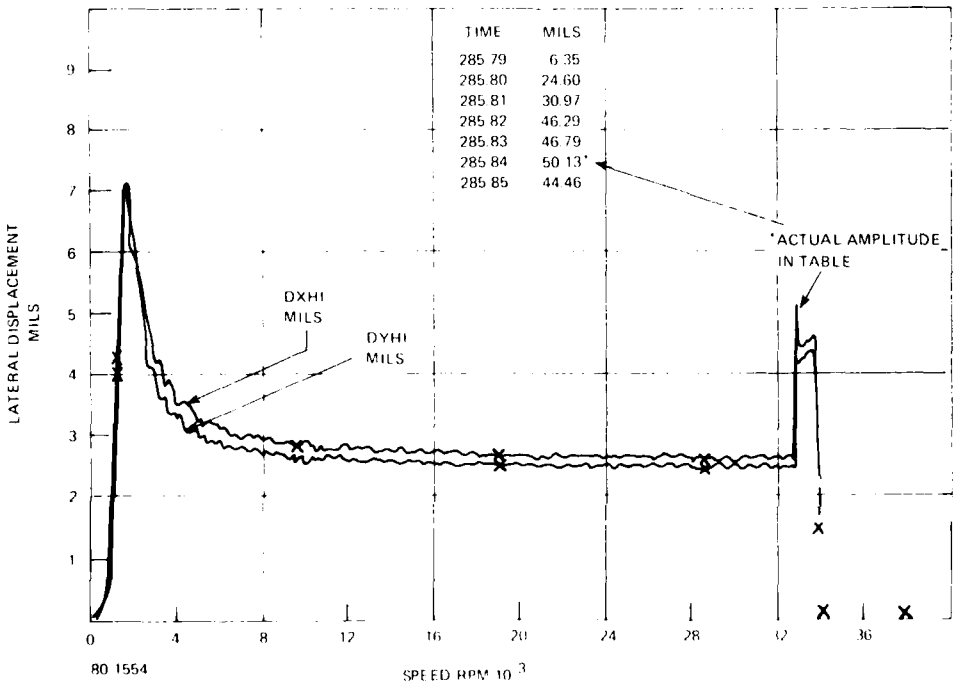

Figure 41 DISPLACEMENT PROBE DATA AT 33,917 RPM – SECOND RUN

No clear explanation of the hub wobble (Event 5) was obtained. What is known was that the real time gage readings failed at this point, indicating displacement gage failure. This is compatible with the gage readings of at least 0.050 inch and the initial setting of the gages with 0.050-inch gaps to the hub. Following gage failure, the flywheel appeared to be spinning correctly and went to a burst speed of 38,741 rps; some 14% higher or 30% higher stress level. To explain the events, it is suggested that the flywheel ID experienced a local crushing under the pressure load of the hub, which had a peak loading of over 5000 psi. This local deformation was asymmetric, and the hub-spindle structures adjusted to a new off-center hub position. In doing so, the peak pressures on the ID could only be increased. Following the local crushing, a small piece of material, probably from the ID top or bottom surface, was pressed out of plane and some two seconds later broke off and triggered the light switch.

7.4 STRAIN JUMP (EVENT 3)

At precisely 256.23 seconds, five strain channels experienced a step change in signal. These are shown in Figures 42 through 46. The other channels were saturated. The strain jump apparently occurred over the entire wheel (Figure 47) and, since there was no disturbance in the displacement gage readings, the strain jump was apparently symmetrical. It was decided to look at crazing as the possible explanation.

Composite crazing or going from an undegraded to a degraded composite is common and acceptable in structural composite design and can be predicted from 90° tensile data. In this case, crazing was expected to start under static loading at (2200 μ strain). This corresponds to roughly 19,000 rpm, based on the strain being proportional to the square of the spin rate. It is suggested that crazing does not necessarily occur at a precise stress level; further, since 19,000 rpm had been exceeded only once and only for a short time, that this phenomena was delayed, and when initiated at one point in the wheel at a stress value 2.5 times that at 19,000 rpm, crazing spread over the wheel with the speed of sound, much less than 0.01 second.

The stress and strain state (as calculated using the WHEEL code) due to a jump from the undegraded state to the degraded state at 31114 rpm, was investigated. Typical results for the 5.7-inch station are reported in Table 10. If the hoop strain is 284 μ strain, the radial jump at the ID would be

(1.61) (0.000284) = 0.00046 inch.

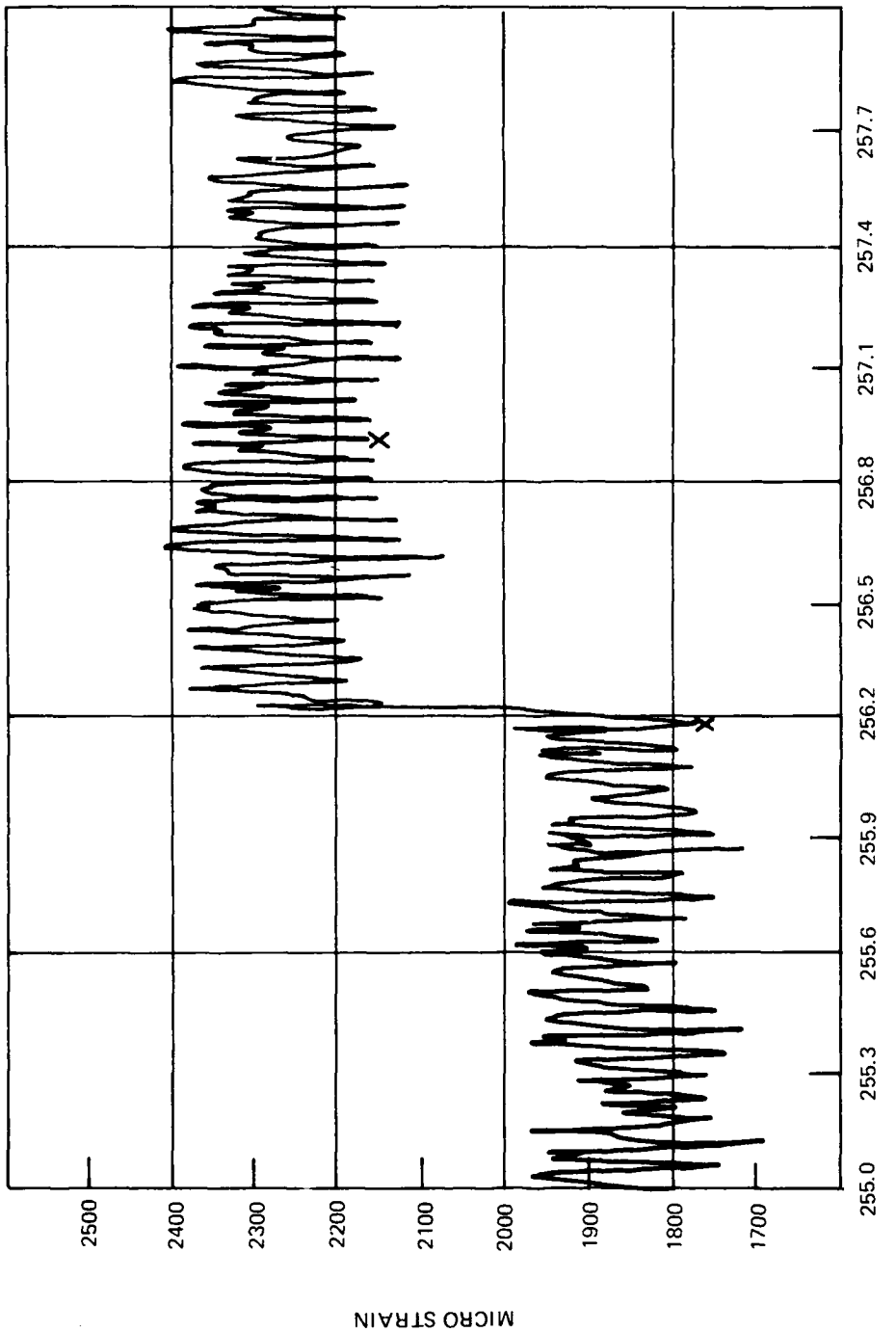

Figure 42 STRAIN JUMP AT 31,114 RPM (256.23 SECONDS) – SECOND RUN, CHANNEL 2 RADIAL

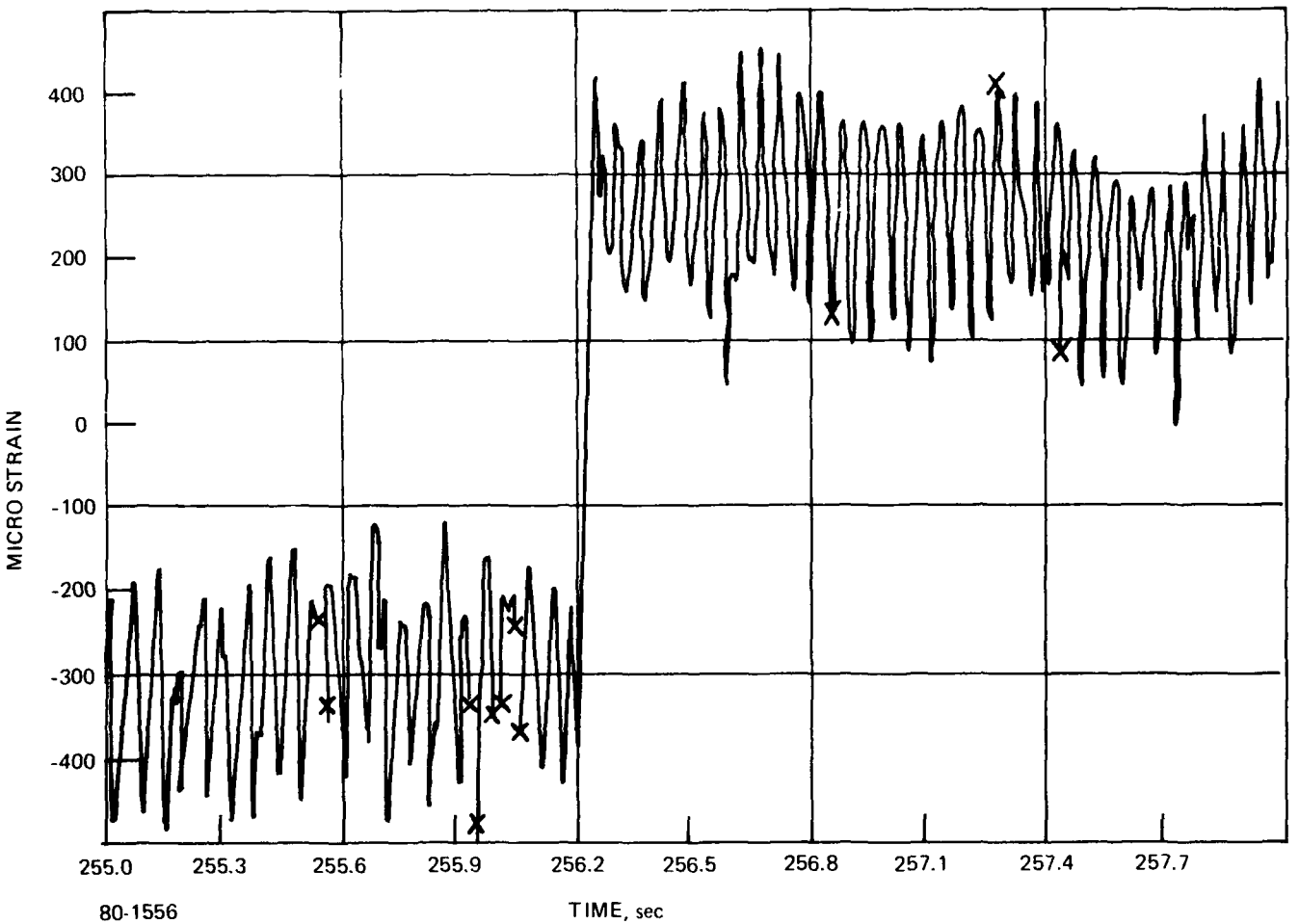

Figure 43 STRAIN JUMP AT 31,114 RPM (256.23 SECONDS) – SECOND RUN, CHANNEL 6 RADIAL

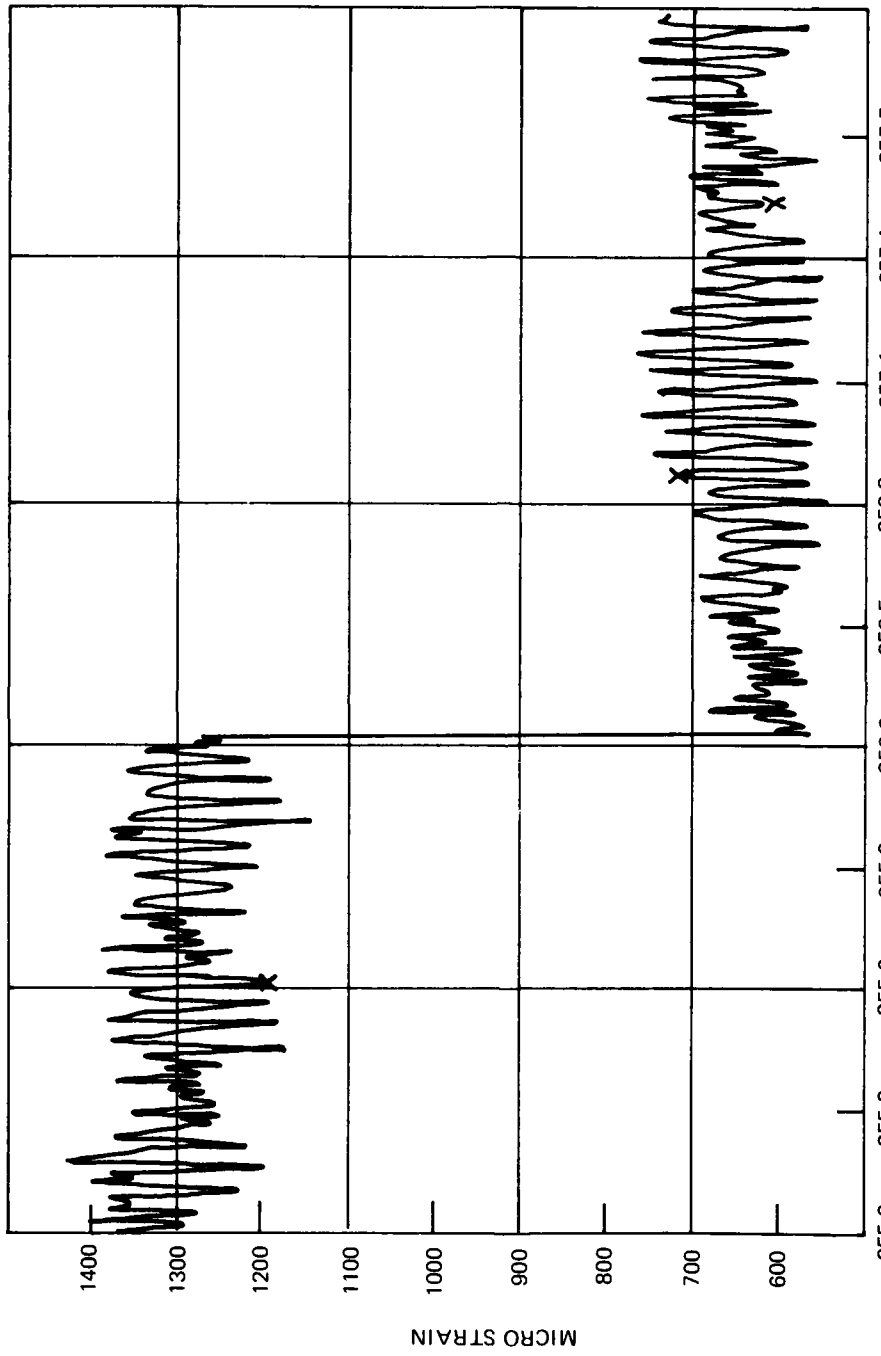

Figure 44 STRAIN JUMP AT 31,114 RPM (256.23 SECONDS) – SECOND RUN, CHANNEL 10 RADIAL

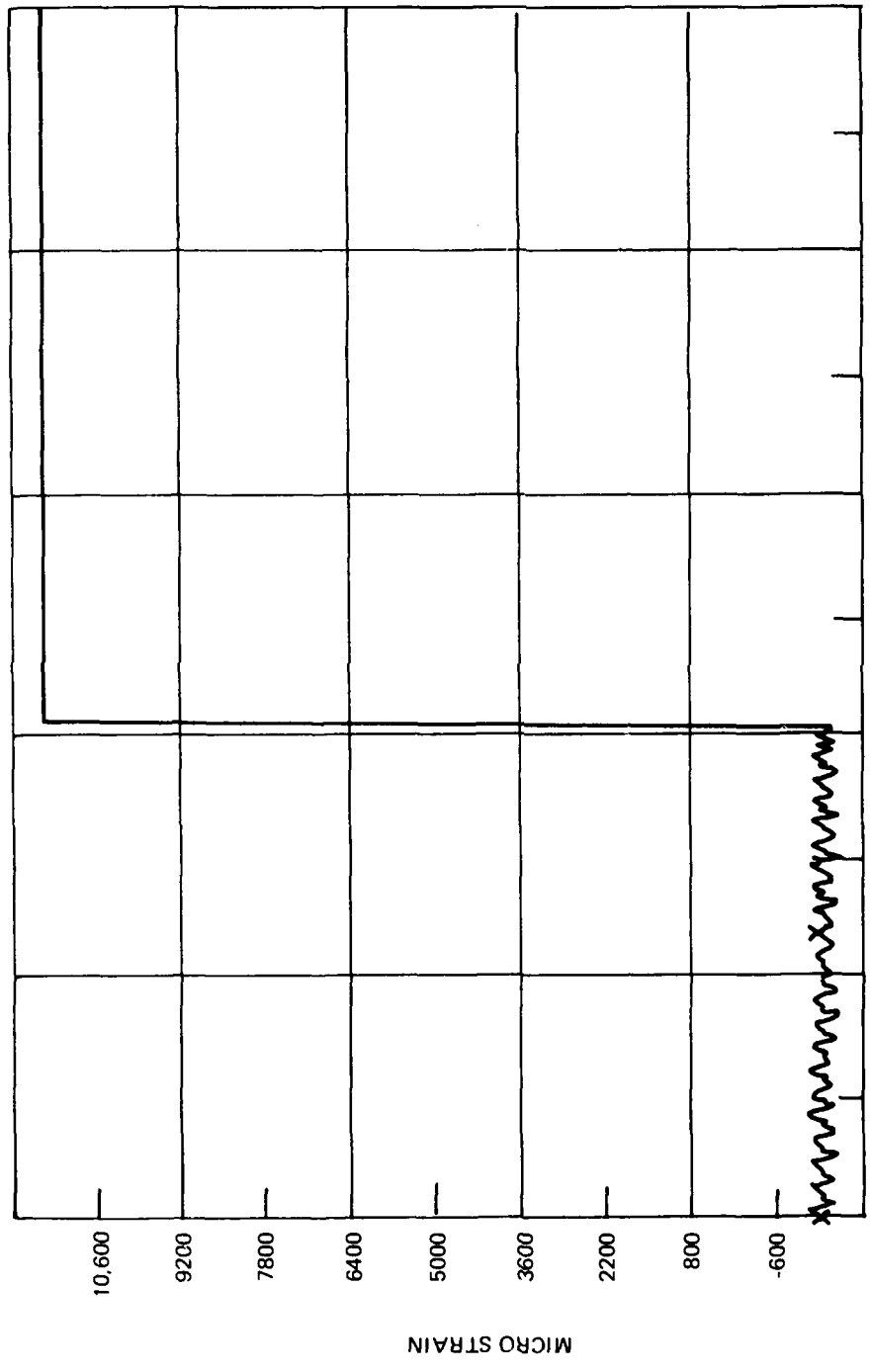

Figure 45 STRAIN JUMP AT 31,114 RPM (256.23 SECONDS) – SECOND RUN, CHANNEL 11 RADIAL

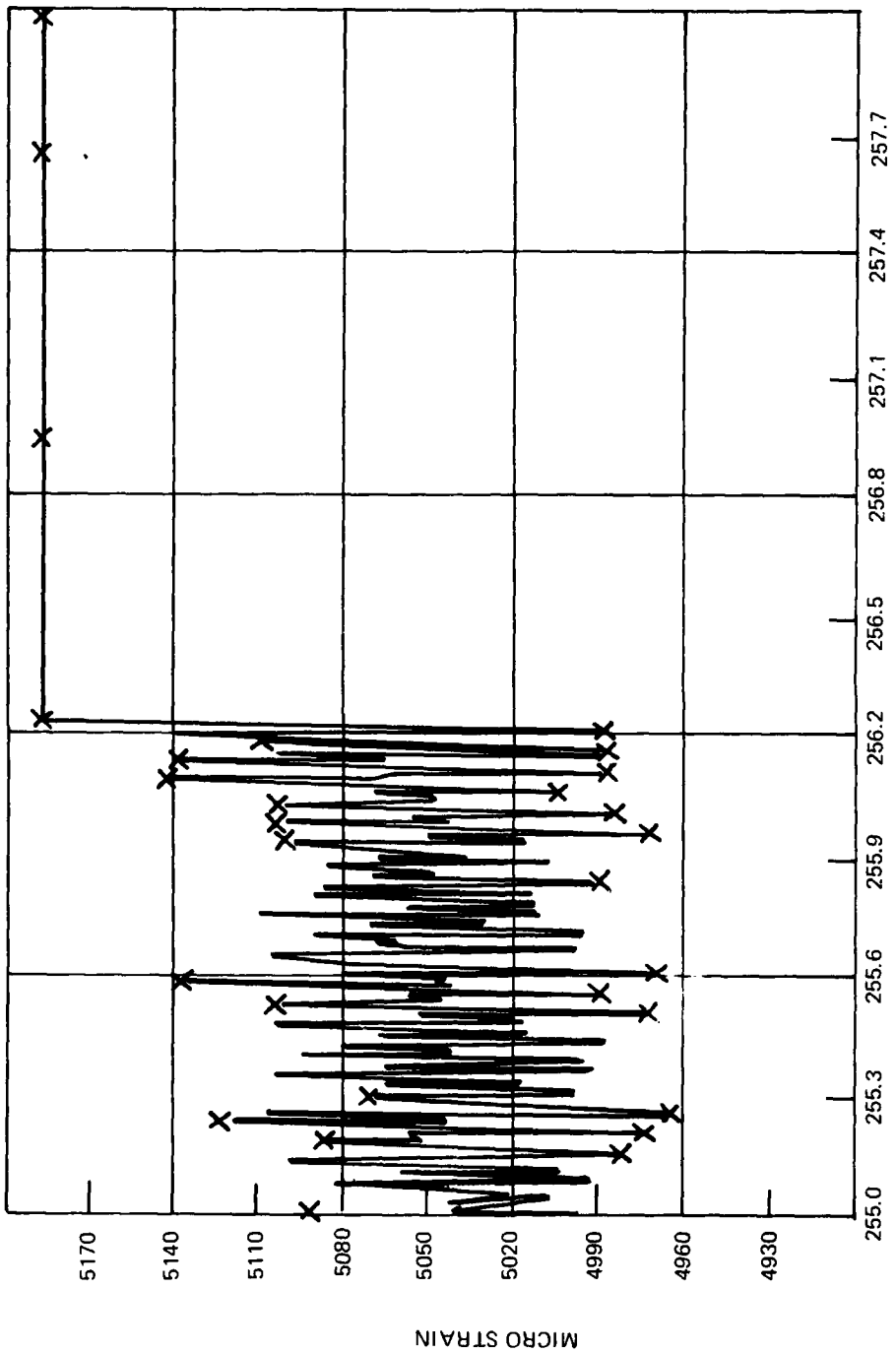

Figure 46 STRAIN JUMP AT 31,114 RPM (256.23 SECONDS) – SECOND RUN, CHANNEL 12 HUB ARM

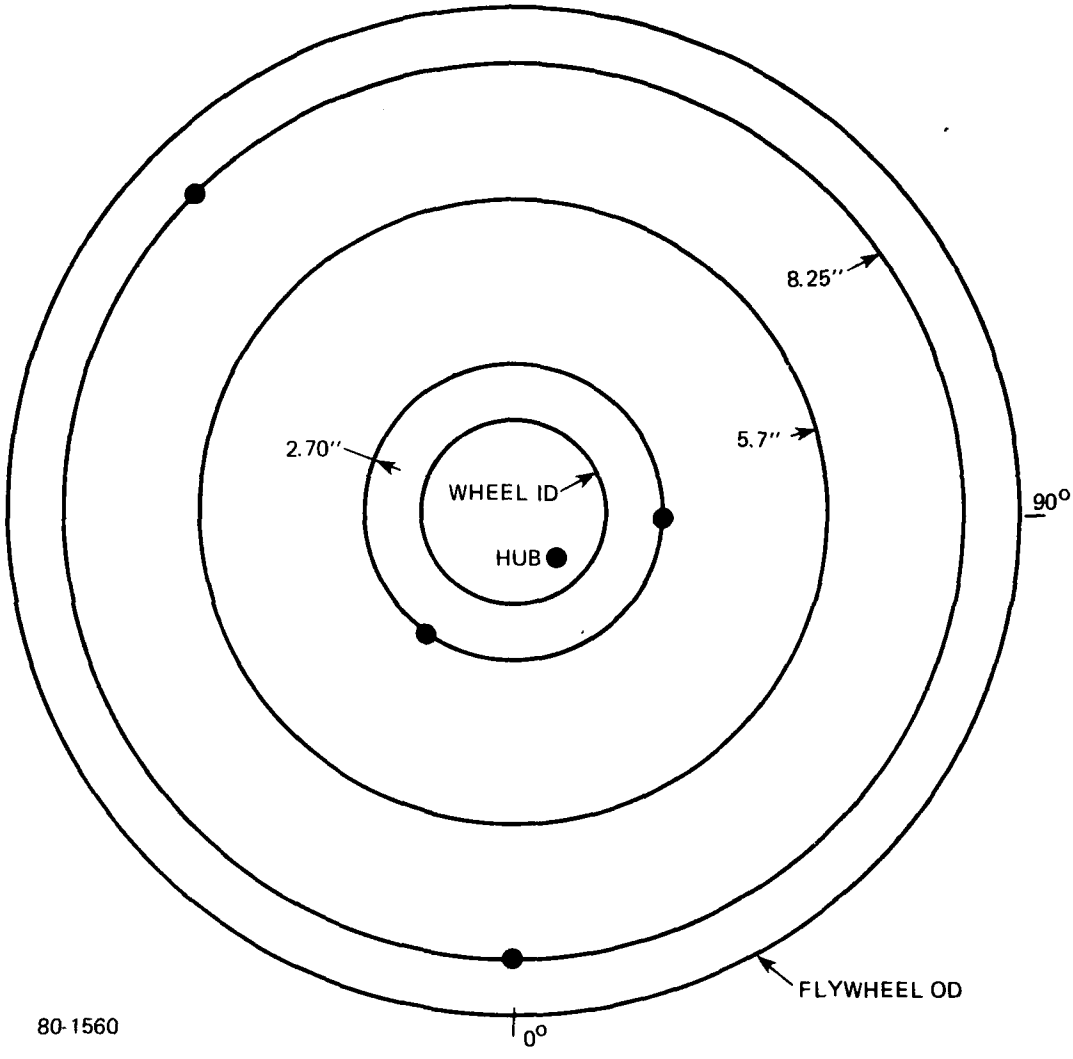

Figure 47 LOCATION OF STRAIN JUMPS AT 31,114 RPM

Scaling data from channel 12 (hub arm strain) the radial growth would be at least

$$\frac{125}{5076}\ (0.0124) = 0.00031 \text{ inch.}$$

TABLE 10. STRESS/STRAIN COMPUTATIONS AT 31,114 RPM, r = 5.7 INCHES

	Undegraded	Degraded	Change
ε_r (μ strain)	4606.00	5339.00	733.00
ε_θ (μ strain)	4904.00	5188.00	284.00
σ_r (radial), psi	57050.00	64062.00	
σ_θ (radial), psi	5056.00	0.00	
σ_r (hoop), psi	5214.00	0.00	
σ_θ (hoop), psi	60571.00	62254.00	

While none of the channels exhibiting the strain jump were saturated, all but Channel 12 were suspect and it is probable that the jump amplitude in this channel was obscurred (limited) by saturation. Nevertheless, the measured and predicted values are presented in Table 11.

TABLE 11. COMPARISON OF MEASURED VS. ESTIMATED STRAIN JUMP

Channel	Measured Jump μ Strain	Estimated Strain
2	400	733
6	550	733
10	-600	733
11	-1200*	733
12	125 minimum	284

*Channel 11 polarity might have been reversed in Run II (See Appendix A).

It is seen that if the above strains are considered in absolute values, not unreasonable considering the character of these channels at this point, there is a reasonable correlation. Accordingly, it is considered that the strain jump phenomena observed was due to a precipitous change from an undergraded to degraded state akin to precipitation in a supersaturated liquid.

7.5 BURST SPEED (EVENT 8) AND FAILURE MODE (EVENT 9)

A study of the computer data clearly indicates the burst speed. Figure 48 shows the computer plot of speed vs. test time with excerpts of speed (every 0.01 second) data taken from the computer printout. Burst was initiated at 342.58 seconds into Run II. The burst speed was 38,741 rpm and the specific energy at burst was 32.3 Wh/lb.

The slowdown after burst initiation is attributed to gradual break up and increasing moment of inertia of the flywheel while still restraining the hub. A further study of the strain channels showed that they were all saturated prior to failure and sequentially went, in general, from full positive saturation to full negative saturation. In each case, the step change was within 0.01 second. This type of change is typical of that which would occur from a break wire. Table 12 shows this strain data, and Figure 49 plots these data at the strain gage locations on the wheel. The initial failure point at "X" was suggested, and the distances from "X" to each gage location were measured and are shown in the last column of Table 12. These distances and failure (break wire) times are plotted in Figure 50 and show a trend of progressive failure from the ID to the OD. To support this analysis, the flywheel speed vs. time is superimposed on this plot. It is seen that the speed decrease, moment of inertia of flywheel size increase regime, held until 0.03 second after the last break wire.

TABLE 12. STRAIN CHANNEL READINGS AT AND POST FAILURE INITIATION

Channel	Type	Channel Reading	Time	Distance from X*
1	H	1971.2 → -1991.0	342.58	1.0
2	R	-4028.1 → 11525	342.58	1.0
3	H	2773.3 → 4493.4	342.75	4.6
4	R	1963.4 → -1964.6	342.65	4.6
5	H	1940.0 → -1954.1	342.72	9.8
6	R	1951.3 → -1934.7	342.75	9.8
7	H	1956.7 → -1936.0	342.79	10.7
8	R	1970.8 → -1984.0	342.74	10.7
9	H	1968.6 → -1983.8	342.74	4.7
10	R	1957.3 → -1956.3	342.78	4.7
11	R	11511 → -11426	342.79	8.4
12	Hub	5188.8 → -3816.7	342.78	--

*X - Assumed initial failure point

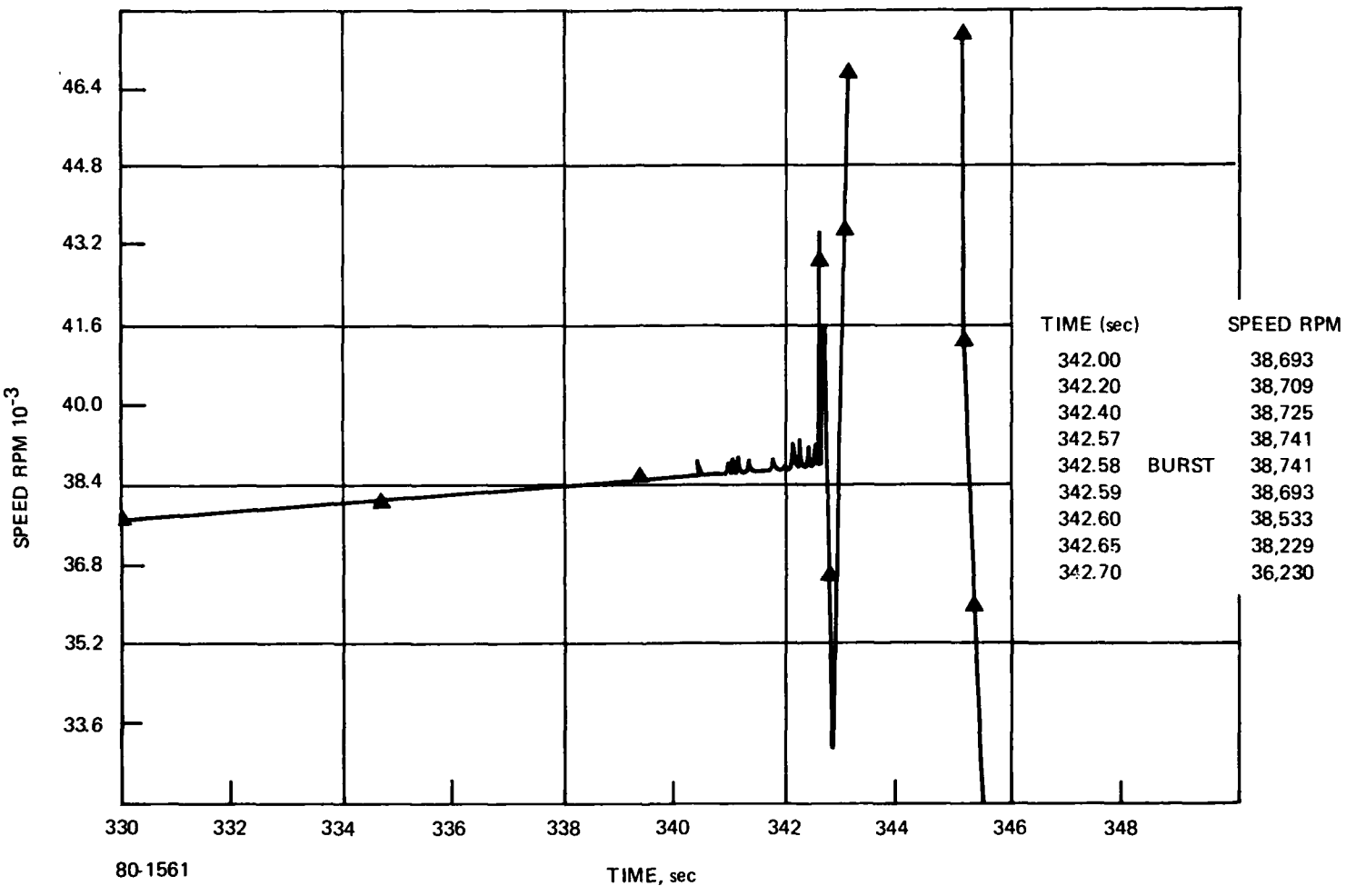

Figure 48 SPEED vs. TIME – SECOND RUN

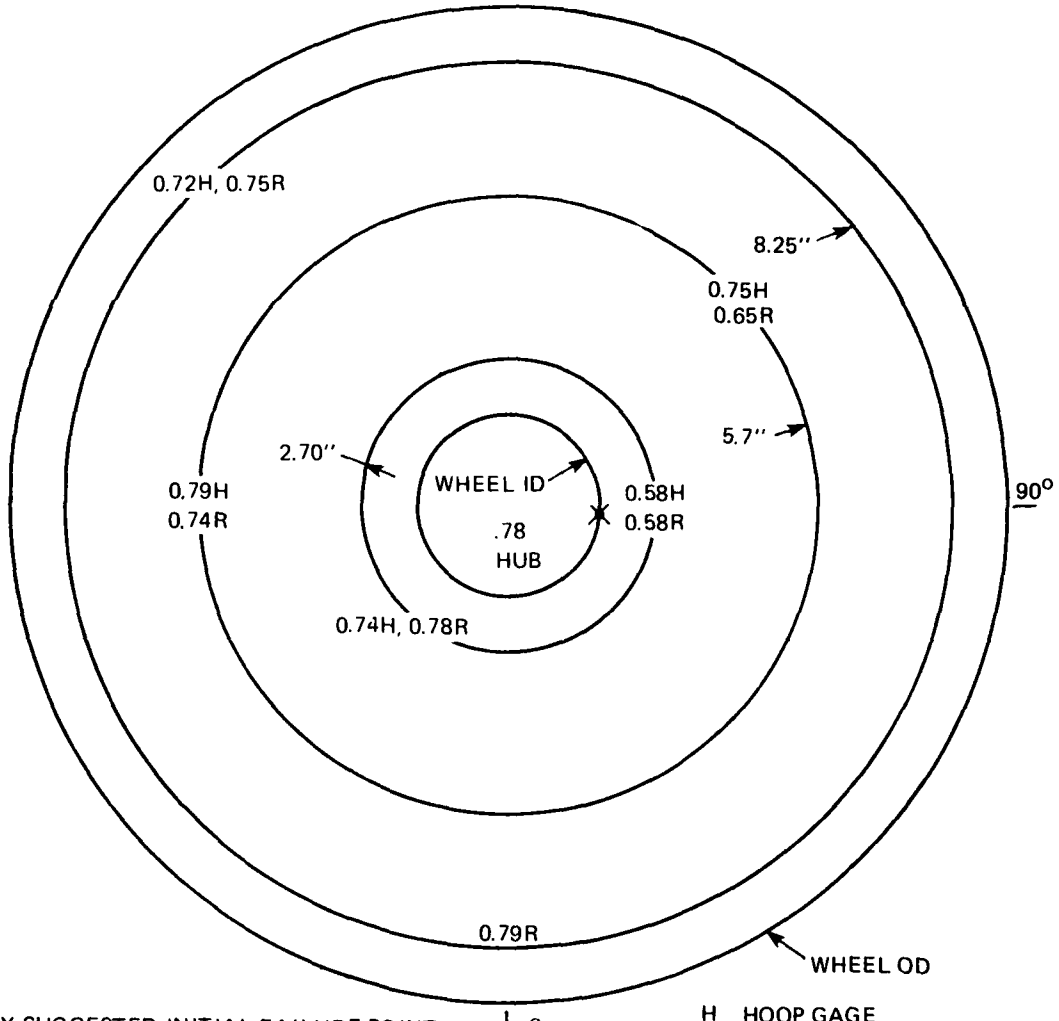

Figure 49 FAILURE SEQUENCE (STARTING AT 342.58 SECONDS) – SECOND RUN

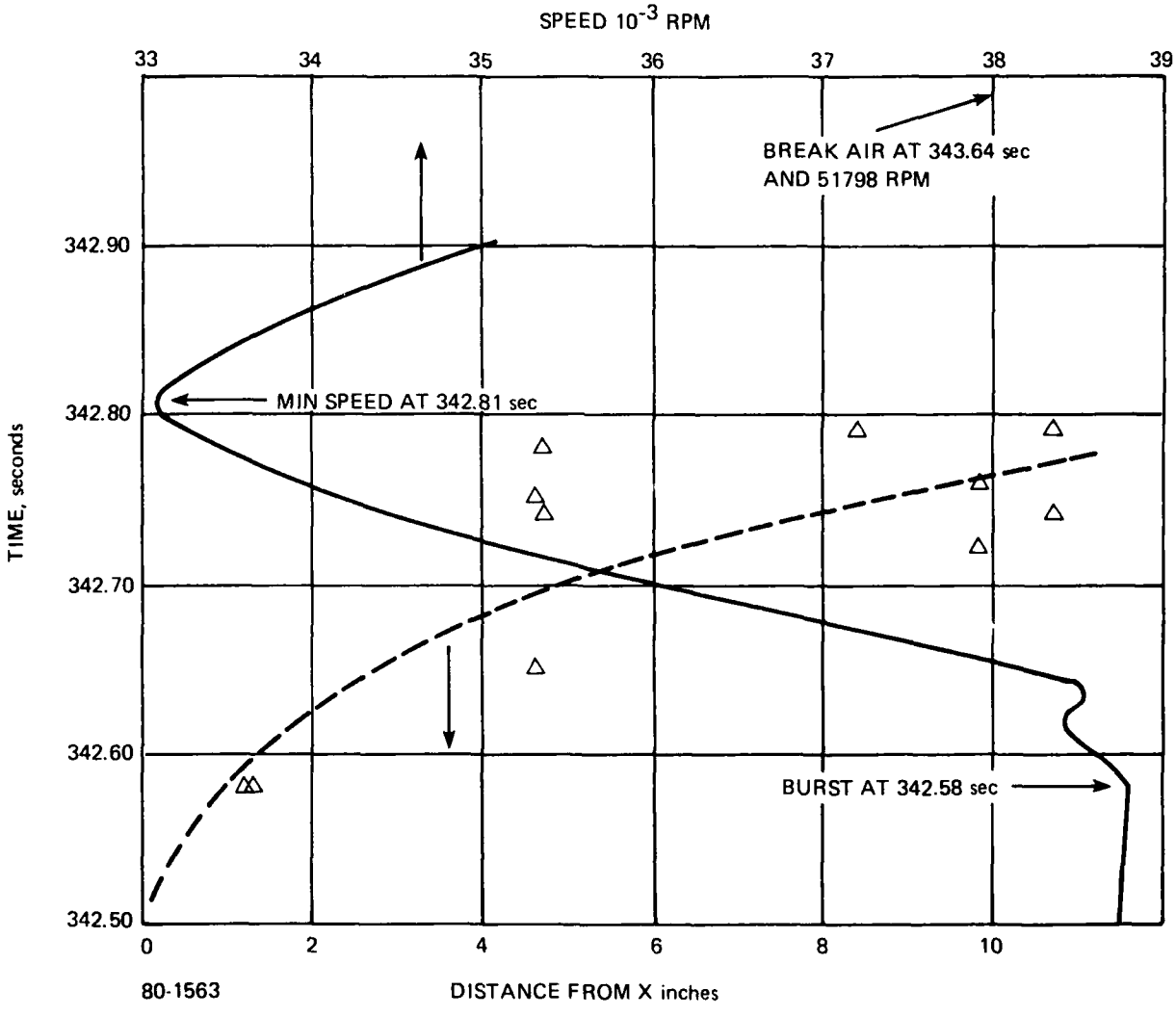

Figure 50 DISTANCE/TIME PATH FROM SUGGESTED FAILURE POINT X

Additional supportive evidence was obtained from the metal hub found in the Kevlar debris after test. Figure 51 shows the post hub yielded condition. From the bottom, the arms are bent clockwise. The rotation during test was counterclockwise. As the flywheel moment of inertia increased during failure, the system decelerated, applying a clockwise torque to the arms. An evaluation of arm loads due to this torque based on the turbine counter torque and moment of inertia, yielded less than 5000 psi lateral bending stress. If, however, the ID also grew during this time period, then the arms and pads would follow radially as they were designed to do, maintaining some pressure even beyond their yield points. It would be through this pressure and resulting friction that the counter torque would be applied to achieve slowdown; such a torque, which by itself produced low stresses, could have caused, in the post yield condition, the rather uniform clockwise twisting of the hub arms. The single broken arm appeared to have broken upon impact with the chamber wall.

While photographic data at failure was not obtained, the above data are considered strong evidence that wheel failure was initiated at the ID. Accordingly, an analysis of the state of stress at the ID was conducted. The analysis was applied to the hoop layer, which was fully stressed in tension at the inside radius. It incorporated measured stress allowables, stresses computed using the WHEEL code, and the Tsai-Hill failure criterion.

7.5.1 Failure Mode Analysis

The behavior of the radial fibers under the compressive hub loading is of central importance in determining the transverse stress in the hoop layer. Because the actual behavior is not well understood, three cases were investigated that cover the range of possibilities: (1) the radial fibers have the same strength and stiffness in compression as they do in tension, (2) fiber buckling results in zero stiffness in compression, and (3) fiber buckling results in the compressive radial stiffness of the radial layer being equal to the compressive radial stiffness of the hoop layer.

The failure speed was well above the speed at which crazing, i.e., degrading of material properties, were expected. (This speed is approximately 19,000 rpm.) However, under compression, some of the undegraded properties should reappear. In this analysis, degraded properties were used for tension loading, while undegraded properties were used when the loading was compressive. The transverse stiffness and transverse stress allowable for the hoop layer are thus nonzero. Similarly, the shear stress allowable is for undegraded material.

80-1564 29149 A

Figure 51 SPINDLE HUB – POST TEST

The Tsai-Hill failure criterion for a unidirectional fiber lamina (Reference 2) is

$$\frac{\sigma_1^2}{X^2} - \frac{\sigma_1\sigma_2}{X^2} + \frac{\sigma_2^2}{Y^2} + \frac{\sigma_{12}^2}{S^2} = \bar{\sigma}^2, \geq 1 \text{ for failure}$$

Where

σ_1 = normal stress in fiber direction

X = normal stress allowable in fiber direction

σ_2 = normal stress in cross-fiber direction

Y = normal stress allowable in cross-fiber direction

σ_{12} = shear stress in plane of lamina

S = in-plane shear stress allowable

$\bar{\sigma}$ = normalized equivalent stress

The values used for the stress allowables were taken from References 1 and 2.

X = 211,000 psi for an 8 ply sample
189,000 psi for a 2 ply sample

Y = 7690 psi

S = 7900 psi

The computed hoop layer stresses for the three cases of radial layer behavior are presented in Table 13. The shear stress was computed from the hoop stress as shown in Reference 4.

$$\sigma_{r\theta} = \frac{\pi\ (1-\gamma)}{N_r}\left(\rho\Omega^2 r^2 - \sigma_\theta\right)$$

γ = proportion of circumference in radial layer taken up by radial, at radius

N_r = number of radials

ρ = lamina density; $\rho g = 0.0487$ lbf/in^3

Ω = spin rate, rad/sec

r = radius

For Case 1, σ_r is as computed by the WHEEL code for undegraded material properties. It is positive in the hoop layer because the radials, when moving out, cause expansion in the hoop layer which is greater than the compression due to hub loading. For

cases 2 and 3, σ_r is computed from the area average hub load and the area fraction (AF) which resists the load:

hub load = -5350 psi at 38741 rpm

$$\sigma_r \text{ (hoop)} = \frac{-5350 \text{ psi}}{AF}$$

The Tsai-Hill criterion is applied for both fiber direction allowables, and the results are shown in Table 13. The last case considered (Case 4) was that for zero hub loading. Since the radial stress is non-negative in this case, the stresses were computed using degraded material properties. The low values of $\overline{\sigma}$ for this case show how important the compressive hub loading can be in causing failure. Note that the stress state in the hoop layer is fairly uniform with radius for zero hub loading (Reference 4) so the value of $\bar{\alpha}$ is also fairly uniform.

The results show that incipient failure occurs for the Case 3 properties. These seem to be the most reasonable physically, since the resin can be expected to retain its compressive stiffness when fiber buckling occurs. This is compatible with the suggested explanation of the hub wobble (Event 5) and camera light trigger (Event 6). Weakness or local crushing at the ID due to hub pressure also helps justify hub arm strain data with composite strain data at 16,000 rpm. The same hub loading on a composite with better transverse properties such as graphite or glass would have achieved a higher energy level.

TABLE 13. HOOP STRESS AT ID AT 38,741 RPM

Radial Condition	KSI					
	X	σ_θ	σ_r	$\sigma_{r\theta}$	σ^2	σ
1. Full Compression Stiffness	211.0	118.1	+1.900	-0.896	0.382	0.618
	189.0	118.1	+1.900	-0.896	0.458	0.677
2. Zero Compression Stiffness	211.0	118.1	-7.868	-0.896	1.394	1.181
	189.0	118.1	-7.868	-0.896	1.476	1.215
3. E_R (radials) = E_R (hoops)	211.0	118.1	-6.059	-0.896	0.963	0.981
	189.0	118.1	-6.059	-0.896	1.044	1.022
4. Zero Hub Load	211.0	108.5	0.00	-0.820	0.2752	0.524
	189.0	108.5	0.00	-0.820	0.3403	0.583

7.6 FLYWHEEL FAILURE MODE SUMMARY AND BURST CONTAINMENT

Unfortunately, because of a premature triggering of the camera, no photographs of the burst were obtained. There are several data that indicated a benign failure occurred.

First, the "failure wire" or strain channel data at failure, together with the speed decrease, indicated that failure progressed over almost a quarter of a second.

Second, the 600 pound steel containment ring surrounding the periphery of the flywheel merely rotated on its supports indicating a symmetrical burst. Past tests such as the graphite wheel failure at one fourth the stored energy dislodged the same ring.

Finally, as with all of the composite flywheels, the resulting debris such as seen in Figure 52 is dust and very small pieces.

Laminated crossplied composites such as the Avco flywheel are natural crack stoppers. Failure into large pieces is not expected. Since Avco's flywheel is also under constant stress, failure initiated at one or several points will redistribute the loads to adjacent areas, and the failure should progress analogous to crack growth over a very short time duration; this crack growth being constantly impeded by each new laminate. Moreover, it is expected that there is some residual strength at the crack provided by the resin and that these cracks represent potential slip planes resulting in a slow radial growth of the flywheel. It is suggested that this growth is not elastic or plastic or directly associated with the material properties but comprised of a series of discontinuous functions. A review of the slowdown at failure shown in Figure 50 shows that this slowdown or slow flywheel growth occurred over a 0.2 second period. The flywheel inertia increase that would cause the measured slowdown represents a uniform radial growth of 0.4 inch.

It is suggested that good use of this failure characteristic can be made by setting the gap between the flywheel rim and the ID of the containment ring (less than 0.5 inch) so that there is an interference at failure during the period of slow growth so that the energy to be contained is mostly rotational. Since the containment ring weight is primarily dictated by the remaining normal component of the translational kinetic energy, low containment weights are expected. The rotational energy can be dissipated in several separate or collective ways. These are friction along the composite ring interface, breakup of the composite, friction associated with rotation of the ring within the vacuum housing or allowing the vacuum housing to spin and windmill to a stop.

Figure 52 KEVLAR FLYWHEEL DEBRIS

SECTION 8.0 OPERATIONAL HUB DESIGN

8.1 DESIGN

As previously mentioned the major problem in Avco's constant stress flywheel design is the interface of the highly strained composite with a metal shaft experiencing essentially no strain. To do this with a hub of sufficient stiffness to eliminate critical resonances over the operating speed range of the flywheel, for a long time seemed almost impossible.

A new approach to the problem was taken. This approach was to configure a hub in a modified Stodola shape to produce a constant stress hub. If only the right material could be found to match the highly strained ID of the constant stress composite flywheel. A number of materials were evaluated with the key parameter being modulus over density. The lower this value the better the chances of developing a high hub strain with low radius. Strength of course was also a factor. From the data developed in Table 14, Durel and its equal counterpart Ardel were chosen (both are polyarylate polymers). A characteristic stress strain curve is shown in Figure 53. This curve shows an elastic rebound from 10% strain over a non linear function.

Analyses were conducted for a hub with a 12-inch OD required to match a fiberglass composite wheel. Because of its lower modulus (lower than graphite or Kevlar) this is considered a worst case design. The shape considered is shown in Figure 54. The resulting stresses are shown in Figure 55. The maximum hub strain level for the glass wheel (16 Wh/lb) was 1.8%. For comparison a 40 Wh/lb graphite wheel would exhibit a 1.8% strain; 2.9% in Kevlar. These are all acceptable values in this hub material.

This material is tough and quite resistant to fatigue. Available data is shown in Appendix B. Since no fatigue data were available directly applicable to our design (i.e., strain cycling), fatigue tests were conducted on standard dogbone specimens. One test covered a 0.5% - 1.8% strain range for 2000 cycles followed by a stress strain test to ultimate. There was no degradation in the stress strain data. The second had a 0.025-inch diameter hole drilled in the test section to simulate a worst case stress concentration. The strain bounds were 0.5% to 2.0% for 10,000 cycles of fatigue. There were no apparent effects such as change in modulus during the fatigue test. Upon examination after the test, small microcracks were found to have been initiated at the hole surface eminating radially approximately one radial

TABLE 14. HUB MATERIAL DATA

	$E \times 10^5$ psi	Tensile σ @ Yield ksi	Flex Strength ksi	Elongation @ Yield/Ultimate %		ρ g/cc	ρ #/in^3	E/ρ	Shear Strength ksi	Cost/ lb.
Vespel (Polyimide)	4.6	12.5		7.5		1.43	0.0517	8.9		
PPS R-120 (Polyphenylenesulfide)	7.0	10.3		2		2.67	0.0965	7.25		
Radel Polyphenylsulfone)	3.1	10.4	12.4	7	60	1.3	0.0470	6.6		$90
Kynar (PVF_2)	1.2	7.4		100		1.75	0.0632	1.90		
Durel* (Polyarylate)	3.0	10.0	15.0	8	30-50	1.2	0.043	7.00	6.0	$ 2.40
Torlon (Polyamide-imide)	6.6	7.5	30.5		12-18	1.4	0.0510	12.9	18.5	$12
DSC-40 (Polycarbodiimide)	2.64	10.8	16.0		7.3	1.2	0.043	6.14		
Ardel* (Polyarylate)	2.9	10.5	11.0	8	50	1.21	0.043	6.7	6.0	$ 2.40

* Inexpensive and in production.

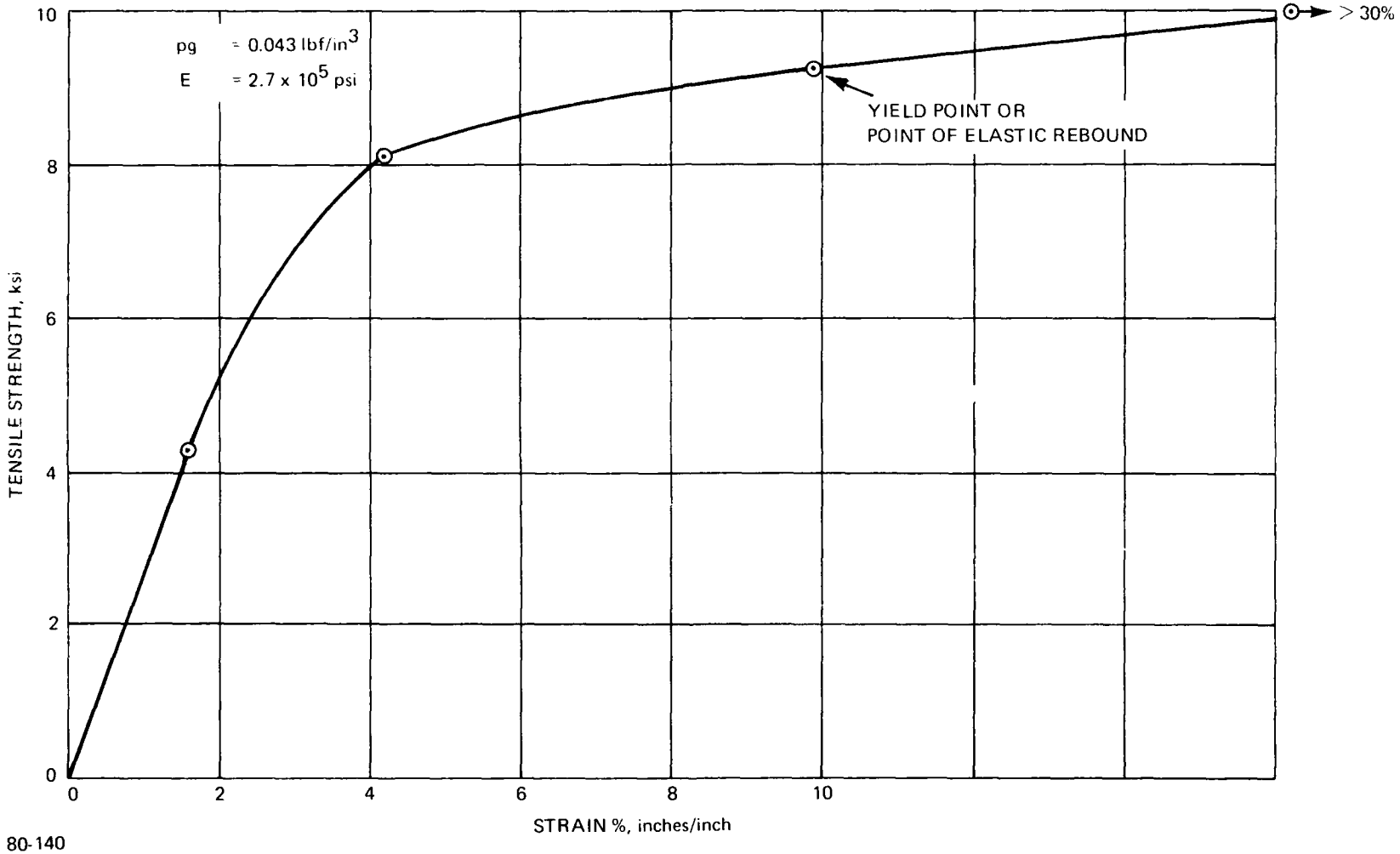

Figure 53 STRESS – STRAIN DATA FOR DUREL

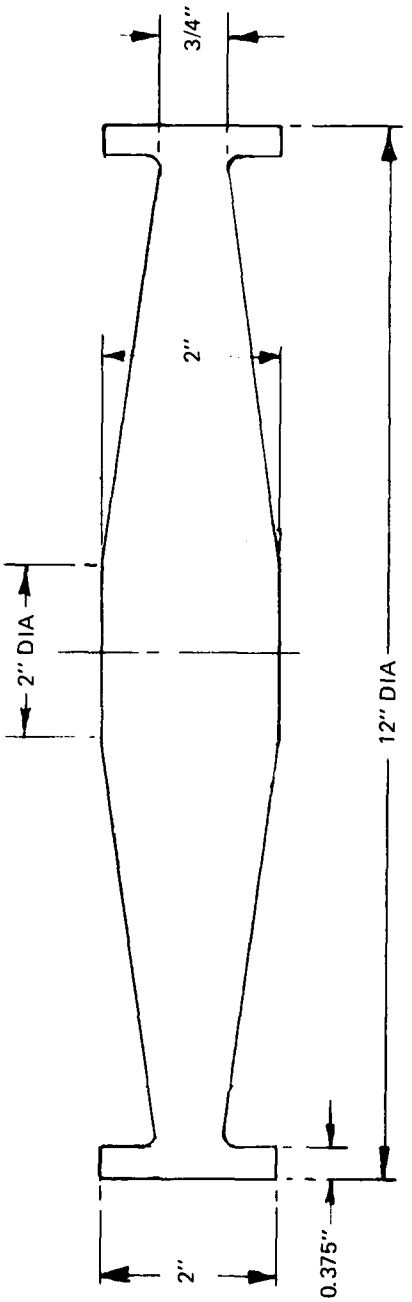

Figure 54 TYPICAL HUB DIMENSIONS

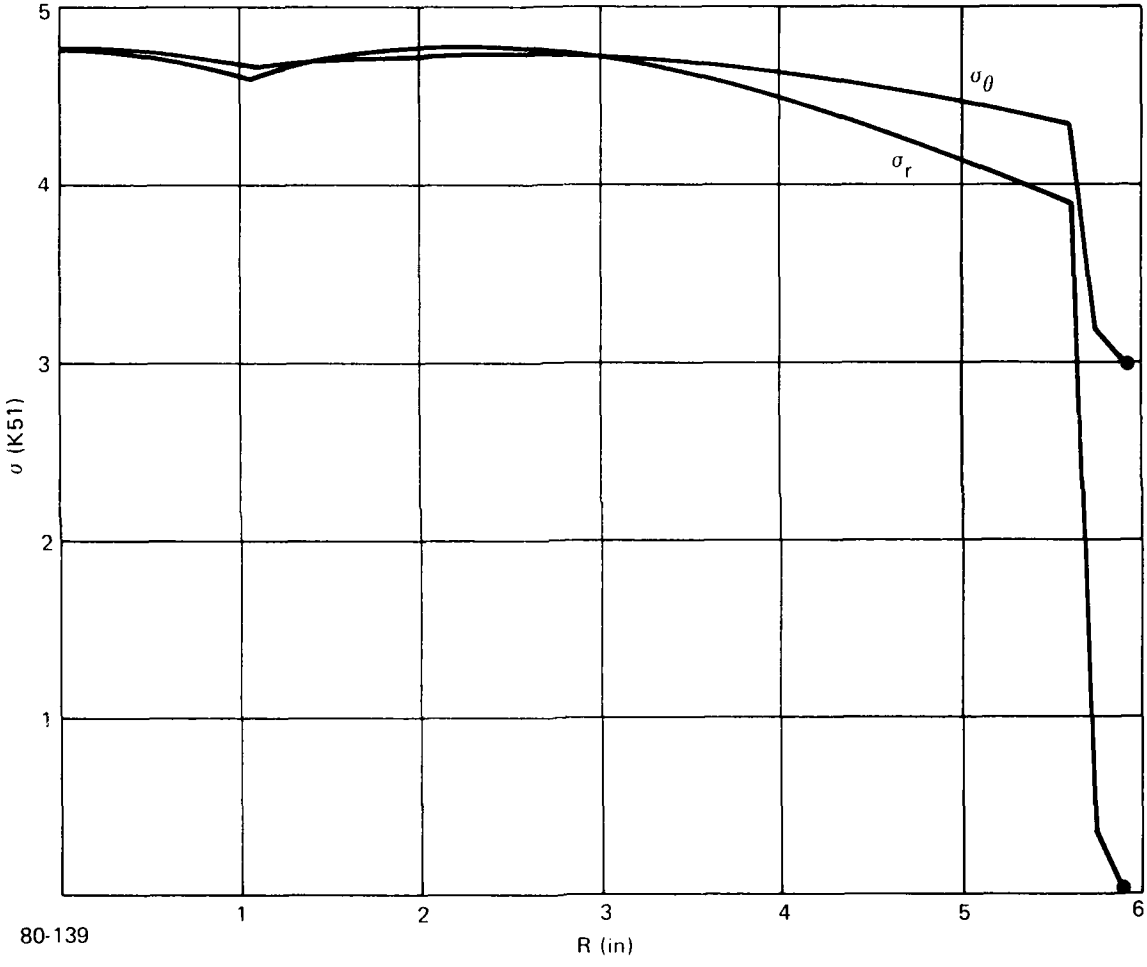

Figure 55 HUB STRESS vs. RADIUS

length. Since there are no holes intended for the hub design nor sharp geometric changes, the stresses generated at the test hole are considered ultra conservative.

8.2 DYNAMICS

Having established the viability of matching the composite ID growth and the resistance of the material to fatigue, the next steps to consider are resonant frequencies and allowable torques or power capability of the polyarylate hub.

When the flywheel is mounted on a shaft the dynamic problems encountered are somewhat different than when the wheel is hung from a spindle. The differences arise because of the vast differences in support stiffness, i.e., a typical shaft is many times stiffer than a spindle. In the case where the wheel is supported by a spindle the most important vibration modes occur when the hub vibrates as a distributed spring-mass system with the large mass of the wheel acting as a fixed boundary (ground). In the present case where the wheel is supported by a relatively stiff shaft the important modes involve the mass of the wheel with the hub providing only stiffness.

One of these modes occurs when the hub flexes as a plate with one nodal diameter (diametric mode). An approximate expression for the frequency in this case is given by

$$f_\theta = \frac{1}{2\pi}\sqrt{\frac{2gEt_{av}^3}{\alpha W R_i^2}}, \text{ hz}$$

where E = Young's modulus of hub material
t_{av} = average thickness of hub (Figure 1)
W = weight of flywheel
R_i^2 = radius of hub (Figure 56)
α = constant given (Figure 57)

Another mode occurs when the wheel vibrates in its own plane acting on the hub as a spring (lateral mode). An approximate expression for the frequency associated with this mode is given by

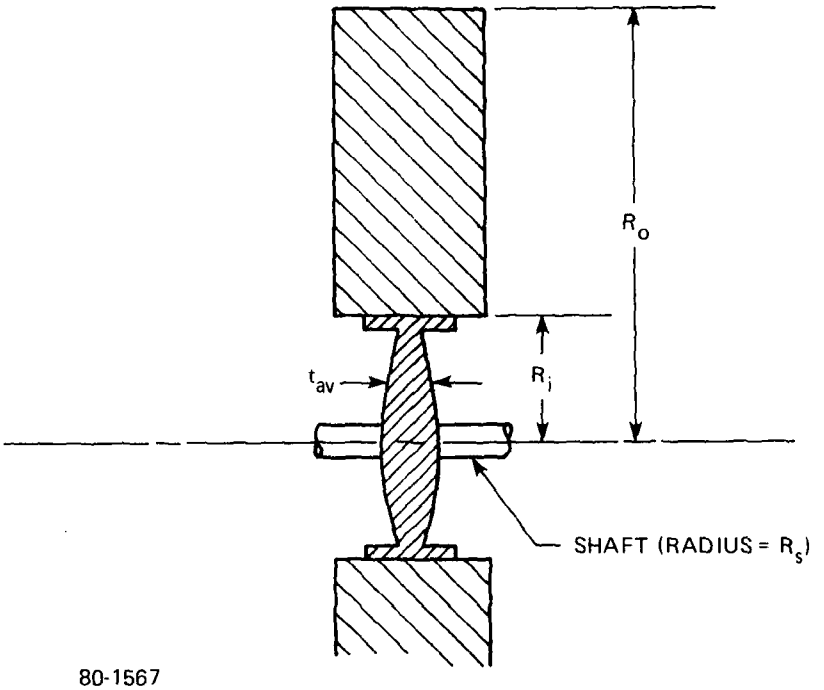

80-1567

Figure 56 FLYWHEEL GEOMETRY

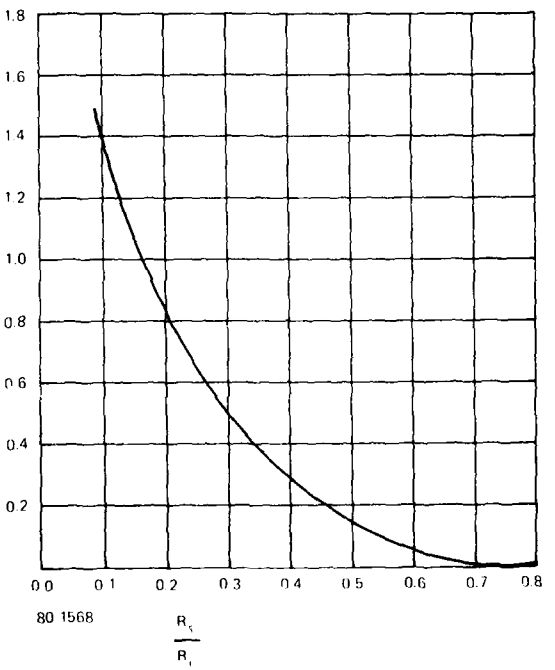

Figure 57 α vs. R_s/R_i

$$f_L = \frac{1}{2\pi}\sqrt{\frac{\pi(R_i + R_s)\, t_{av} E g}{(R_i - R_s)W}}\ , \text{ Hz}$$

where R_s = the shaft radius and the other constants are as defined previously.

The last mode of importance is sometimes called the "umbrella mode" and consists of an axisymmetric deformation of the hub into a dish-like shape. An approximate expression for the frequency of this mode is given by

$$f_u = \frac{1}{2\pi}\sqrt{\frac{R_s D g}{w R_i^4 \beta}},\ \text{Hz}$$

where D = hub bending stiffness, $\frac{Et_{av}^3}{12(1-\nu^2)}$

w = wheel weight per unit length of hub circumference.

β = numerical constant depending on geometry.

This mode can be demonstrated on a shake table but it rarely, if ever, appears in practice as there are no meaningful excitation forces in the axial direction.

Resonance calculations were made for two sample wheels; a 40-lb subscale wheel and a 750-lb wheel. Each had a polyarlyate hub. The shape and dimensions are shown in Figure 58. The results of these calculations are given in Table 15.

TABLE 15. FREQUENCIES FOR SAMPLE FLYWHEELS

Weight Wheel, lb	f_θ (Hz)	f_L (Hz)	f_u (Hz)
40	668	883	198
750	245	389	123

Table 16 shows frequency parameters in rpm for the second Kevlar flywheel and the representative 40 and 750 lb flywheels. Only f_θ is used as it is lower than f_L, and f_u for all practical purposes is hypothetical. It is seen that the projected

COMPOSITE FLYWHEEL				HUB (DUREL)				
lbs. WEIGHT	in. ID	in. OD	in. THICKNESS	in. a	in. b	in. c	in. d	lbs. WEIGHT
40	8	21	2.5	2.5	2	2	1	3
750	17	50	7.5	5	9	12.5	5.25	95

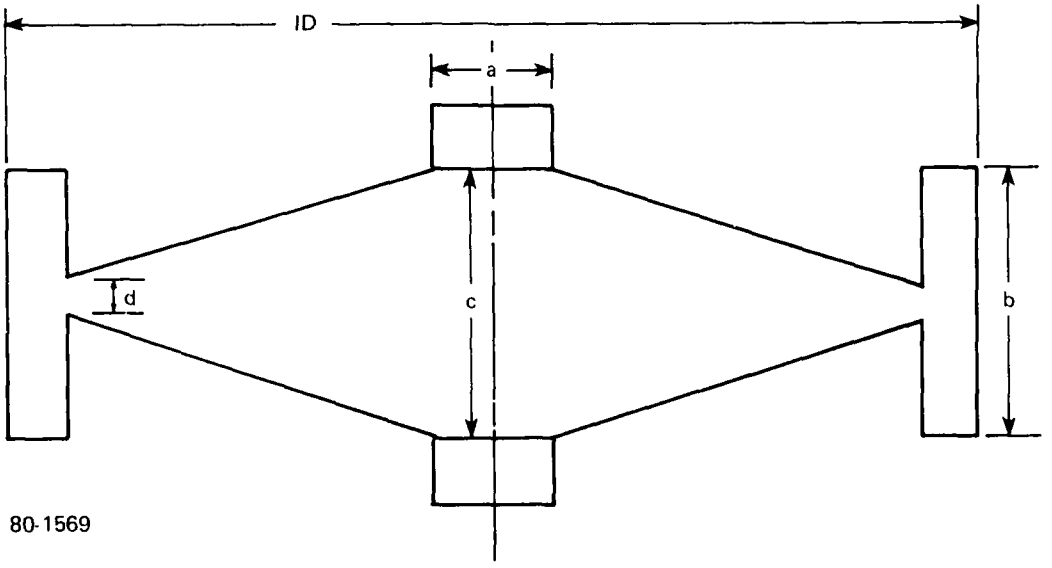

Figure 58 REPRESENTATIVE FLYWHEEL/HUB DIMENSIONS

speed ranges of interest will not encounter critical resonances. There is also considerable design flexibility in raising f_θ.

TABLE 16. COMPARISON OF OPERATING SPEEDS AND CRITICAL RESONANCES

		Test Data		Scaled Speeds		Computed Critical Resonances
Flywheel	OD Inches	Speed rpm	Wh/lb	20 Wh/lb - Speed rpm	40 Wh/lb - Speed rpm	Lowest resonance rpm
Second Kevlar test	19.5	38741	32.3	30485	43112	large
40-lb Subscale	21			28307	40033*	40080
750-lb Full Scale	50			11889	16814	23520

*To increase resonance by $\sqrt{2}$ requires increase in dimensions c and d by $(\sqrt{2})^{2/3}$ or 1.26.

A second hub design factor is its ability to deliver power or sustain torque. Analyses for the full scale 750-lb wheel were made.

If one assumes a shaft of 5-inch diameter is used in a 750-lb wheel, the torsional moment of inertia is given by

$$J = \frac{1}{2}\pi R^4 = 61 \text{ in}^4$$

With a shear allowable of 6000 psi in the polyarylate shaft, the allowable torque is given by

$$T = \frac{\tau J}{R_s} = 147{,}600 \text{ in-lb}$$

The stub shaft must be long enough to give sufficient bond area to transmit the above torque. If L is the stub shaft length and the bond strength is assumed to be 2000 psi then

$$L = \frac{147{,}600}{(2000)(2\pi R_s)} = 1.9 \text{ in.}$$

At 147,600 in/lbs of torque and 16,814 rpm, the deliverable power is

$$\frac{(147{,}600 \text{ in lbs})}{(12)\ 737.6}\ \left(\frac{16{,}814}{60}\right) 2\pi = 29362 \text{ kW},$$

almost 10 times the goal power for the program. It should be noted that hub stiffnesses used in dynamic calculations were estimated from static loadings of various circular plates given in References 5 and 6.

8.3 OTHER DESIGN CONSIDERATIONS

There are several additional comments that should be made regarding the hub flywheel interface. The first is that the relative ID to OD of the wheel should be increased to allow sufficient hub material to spread the radial growth of the composite ID. Values from 1/3 to 1/2.5 are suggested so that the use of the swept volume is reduced from 97 percent; as for the second Kevlar wheel, to as low as 85 percent, a very acceptable value.

While in this design the pressure on the ID can be markedly reduced from that developed by the metal hub used in the second Kevlar test, serious consideration should be given to composites with better cross fiber characteristics, especially for bi-directionally reinforced composites. This suggests fiberglass or graphite. Graphite is indicated for high performance flywheels because of its superior fatigue properties. Because of its high modulus, it will also exhibit the lowest ID growth. Graphite, Kevlar and glass are all competitive in their strength/density or potential energy density properties. While glass is the lowest in cost, industry data suggest that pitch graphite fibers will be competitively priced.

SECTION 9.0 CONCLUSIONS AND RECOMMENDATIONS

The following conclusions are made:

(1) All strain channels provided useful data for analysis of the flywheel and hub performance.

(2) Strain data faithfully followed the predictions of constant stress. This justifies the validity of applying the small effort required to re-optimize any specific flywheel design using both 1-D and 2-D finite element analyses.

(3) The strain measurements on the flywheel and on the hub arm suggest that the effective modulus of the composite was at least 10% less than that obtained from unidirectional fiber composite tests.

(4) The strain measurements on the flywheel and on the hub arm suggest that crazing will occur precipitously at a stress level some two to three times that predicted and can be expected in early runs of any bidirectional composite flywheel.

(5) Strain measurements on the flywheel and hub arm suggest that the hub pressure on the ID was instrumental in producing increased defection at the ID due to local crushing (some 0.0024 inch at 16,000 rpm).

(6) From speed data and strain data, the flywheel failed at 38,741 rpm, a specific energy level of 32.3 Wh/lb.

(7) From speed data, strain data and the failure analysis, the failure was initiated at the ID by the hub pressure.

(8) Reduction of hub pressure at high speed and/or substitution of fibers with higher cross fiber properties than Kevlar, such as fiberglass or graphite, will affect a meaningful increase in specific energy.

(9) Displacement gage data verify the resonant frequency predictions for the metal hub and show that the failure was not connected with a resonance.

(10) Displacement gage data suggests that the hub wobble and subsequent camera trip were caused by small local asymmetric crushing of the 1-D due to hub pressure.

(11) There is a logical linkage between conclusions 5, 7, 8 and 10.

(12) Based on post test debris, failure analysis of the second Kevlar wheel and burst photographs of similar laminated composite flywheels, Avco's design failed in a benign mode relative to burst containment design requirements.

(13) The new hub design using molded polyarylate material will markedly reduce hub pressure on the 1-D and provide sufficient stiffness to raise flywheel resonances above operating speeds. This design is also capable of delivering the required power.

(14) Based on cross-fiber properties, modulus, strength-to-weight ratio, fatigue properties and projected cost, high performance composite bidirectional flywheels should more thoroughly investigate the use of graphite pitch fibers.

(15) Based on using Avco's constant stress flywheel design with a polyarylate constant stress hub and pitch fibers, a composite flywheel can be built to fill some 85% of its swept volume and attain specific energy levels at burst greater than 50 Wh/lb.

It is recommended that:

(1) A pitch fiber graphite subscale flywheel integrating the hoops and radials in each laminate be built and tested to demonstrate successively hub design, 5000 cycle endurance at 40 Wh/lb, burst energy and failure mode pertaining to burst containment requirements.

(2) Following subscale demonstration, two full-scale flywheels be built for demonstration tests.

(3) In parallel to the above efforts, exploratory analyses and design be conducted on an advanced laminated design capable of increased energy density and combination with a motor generator.

SECTION 10.0 REFERENCES

1. Johnson, D. E., Laskaris, A. T., and Sapowith, A. D., "Phase I - Interim Report High Energy Density Composite Flywheel Program," Avco Systems Division, *MERADCOM report DAAG* 53-75-C-0269, June, 1976.

2. Jones, R. M., "Mechanics of Composite Materials," Scripta Book Co., 1975.

3. Chiao, T. T. and Chiao, C. C., "Aramid Fibers and Composites," VCRL Preprint No. 8040, December 21, 1977.

4. Johnson, D. E., "Structural Analysis and Testing for Composite Flywheel Development," Avco Systems Division, AMMRC report DAAG46-77-C-0017, September, 1977.

5. Roark, R. J. and Young, W. C., "Formulas for Stress and Strain," 5th Edition, McGraw Hill Book Company, 1975.

6. Timoshenko, S. and Wornowsky-Krieger, S., "Theory of Plates and Shells," 2nd Edition, McGraw Hill Book Company, 1959.

AD-A087 076 AVCO SYSTEMS DIV WILMINGTON MA F/G 11/4
HIGH ENERGY DENSITY COMPOSITE FLYWHEEL PROGRAM.(U)
MAY 80 A D SAPOWITH, A L GURSON, J A MCELMAN DAAG53-75-C-0269
UNCLASSIFIED AVSD-0170-80-RR NL

2 OF 2
AD A
087076

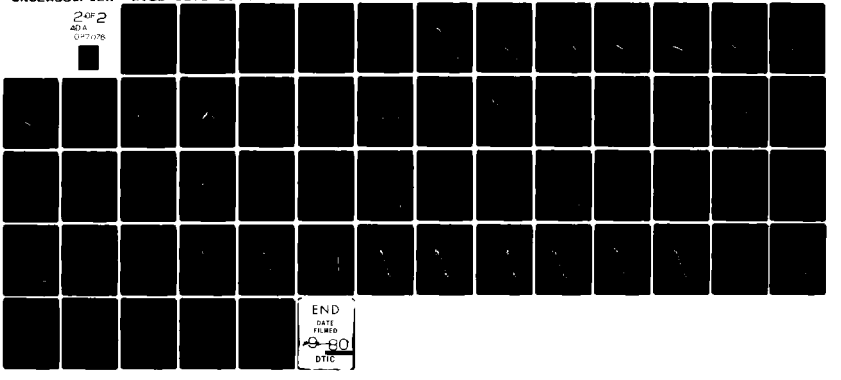

APPENDIX A

ADDITIONAL STRAIN DATA

APPENDIX A ADDITIONAL STRAIN DATA

This Appendix presents additional data and discussion pertaining to the high energy density composite flywheel. Table 3 in the body of the report lists the strain gage channels and descriptions reproduced here as Figure A1. Figures A2 through A13 show the speed and raw strain data for Run 1. The data are representative until approximately 25,000 rpm, when the speed gages become faulty. For clarity only strain data to this point are shown. Channels 2, 4, 6, 10 and 11 all exhibited a decreasing strain or drop off starting at 17,000 to 23,000 rpm. Channel 8 was saturated at this level.

Figure A14 shows the speed data for Run 2. Figure A15 shows the Run 2 hub displacement data, and Figure A16, the hub displacement data for Run 1. All displacement data indicate the pendulum resonance at approximately 1500 rpm. The first run data indicates a small Run 1 disturbance at 16,000 rpm somewhat similar to that at 34,000 rpm, Run 2. Figures A17 through A28 show that the drop-off in radial channels was not repeated, although some abnormalities are seen (Table A1).

TABLE A1. RADIAL CHANNEL OBSERVATIONS

Channel	Run 1	Run 2
2	Drop-off ~ 23,000 rpm	Drop-off ~ 31,000 rpm
4	No dip ~ 17,000, Saturated ~ 21,000 rpm	No drop-off, Saturated ~ 27,000 rpm
6	Drop-off ~ 22,000 rpm	No pattern discernible
8	No drop-off, Saturated ~ 16,000 rpm	No drop-off, Saturated ~ 19,000 rpm
10	Drop-off ~ 17,000 rpm	No drop-off until negative jump at 31,000 rpm. General increase until drop-off ~ 34,000 rpm
11	Drop-off ~ 17,000 rpm	Polarity change, apparent compressive strains

Prior to evaluating the strain data numerically, a comparison of Run 1 to Run 2 was made to check the validity of the data. This is shown in Figures A29 through A39. All hoop channels repeated the same response, Run 1 to Run 2 as did Radial Channel 8. The balance of the radial channels all exhibited lower strain per speed. Since these channels were placed on a hoop layer, it is possible that there was some slippage or local strain effects that caused the drop off behavior. It appears to have been initiated between 17,000 and 23,000 rpm. Perhaps this is associated with the beginnings of crazing, predicted at 19,000 rpm. In any case, in validating those

gages to be used for the strain analyses, all gages were found to be useful below 17,000 rpm on the first run. This is shown in Table A2. While they were not functioning properly at 31,000 rpm, Channels 2, 6, 10 and 11 were not saturated at this point and it is felt that they were able to provide useful data pertaining to the strain jump in Run 2.

TABLE A2. STRAIN GAGE USE SUMMARY

Channel	1st Run	2nd Run	2nd Run Jump Indication	2nd Run Failure Sequence
1	good*	good		x
2	good	bad	x	x
3	bad	good		x
4	good	bad		x
5	good	good		x
6	good	bad	x	x
7	good	good		x
8	good	good		x
9	good	good		x
10	good	bad*	x	x
11	good	bad	x	x
12 (hub)	good	good	x	x
Useable strain channels	11	7		

*For relative strains

Run 1 was cycled 0 to 15,000 to 10,000 to 15,000 to 10,000 rpm toward burst. The speed readings were lost at ~ 25,000 rpm (Figure A40). The Brake Air and Drive Air functioned to respectively slow down and accelerate the flywheel speed. The strain cycling for Run 1 is amplified in Figures A41 through A51. The data are compared for strain at 16,000 rpm on the first leg of Run 1 to strain at 16,000 rpm on the third and last leg of Run 1. The variances are of the order of the noise level. (It is noted that the Brake Air deceleration contained noticeably more noise than Drive Air.) For hoops, there was an average increase of 80 microstrain at 16,000 rpm and an average decrease of 15 microstrain for radials. This should indicate a radial set at the ID of (1.61) (80 10^{-6}) inches = 0.00013 inch.

If the same effects are examined on Channel 12 (Figure A52) there is a corresponding decrease in strain of ~500 microstrain. Since the hub arm was pre-stressed inward, strain readings represent changes in strain from the initial pre-stressed condition. The 500 microstrain decrease indicates that the arm at 16,000 rpm on the last leg was at a smaller radial distance than on the first leg of the run. The flywheel ID was expected to, and apparently did, slightly increase in size with working, leaving a discrepancy of 500 + 80 microstrain, which represents (580/5076) (0.0124) = 0.0014 inch (See Section 7.2). The only explanation proffered here is that perhaps this 1.5 mil displacement was a result of asymmetric local crushing of the Kevlar at the ID. This would explain the small hub wobble detected at ~ 16,000 rpm on Run 1.

CHANNEL NO.	STRAIN DIRECTION	RADIAL POSITION	AZIMUTHAL POSITION
1	HOOP	2.65"	90°
2	RADIAL	2.65"	90°
3	HOOP	5.65"	132°
4	RADIAL	5.65"	132°
5	HOOP	8.25"	222°
6	RADIAL	8.25"	222°
7	HOOP	5.70"	270°
8	RADIAL	5.70"	270°
9	HOOP	2.70"	315°
10	RADIAL	2.70"	315°
11	RADIAL	8.25"	0°
12	HUB ARM	–	67.5°

80-1570

Figure A1 STRAIN GAGE LOCATIONS/ORIENTATIONS

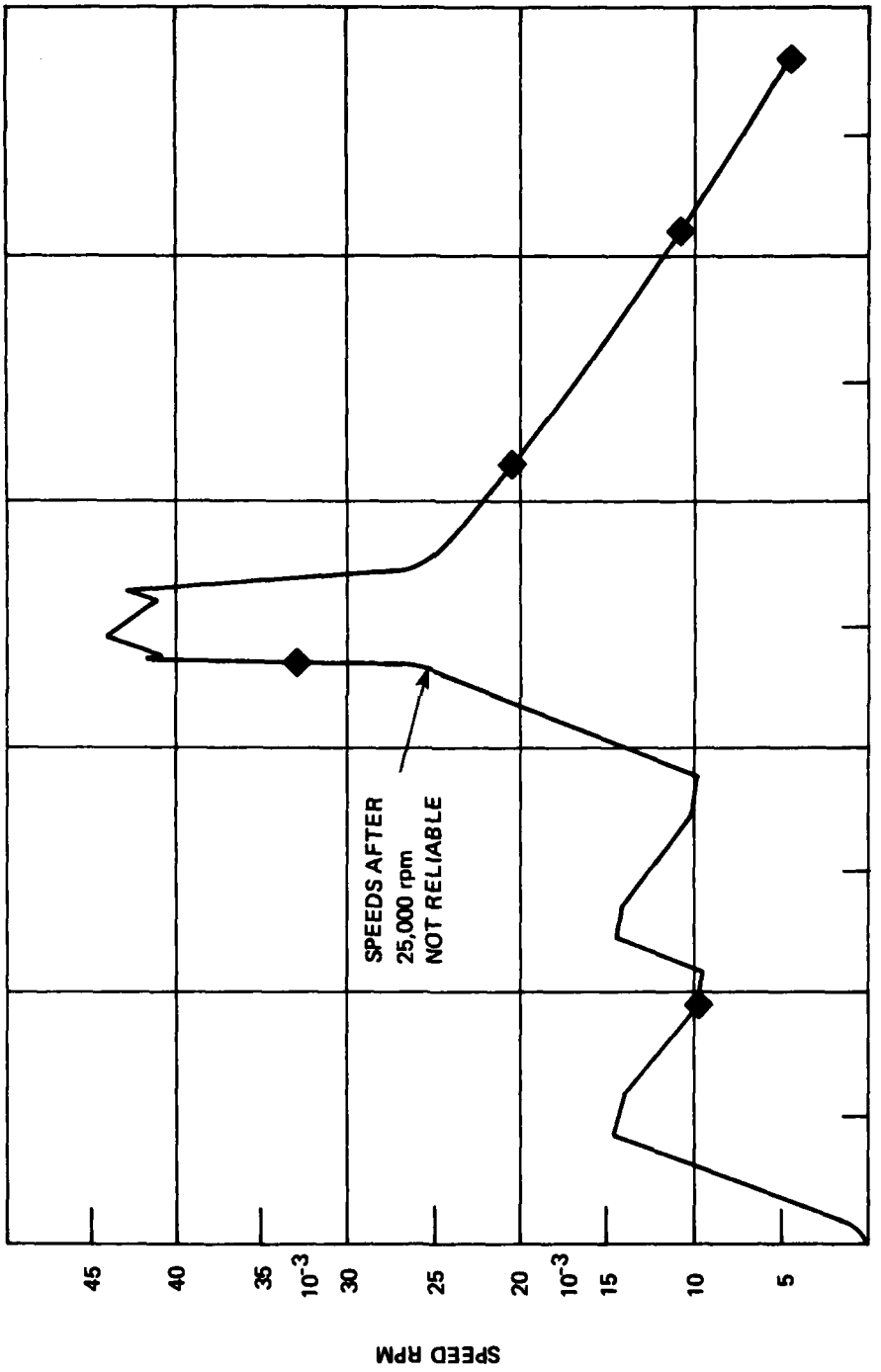

Figure A2 SPEED vs. TEST TIME, RUN 1

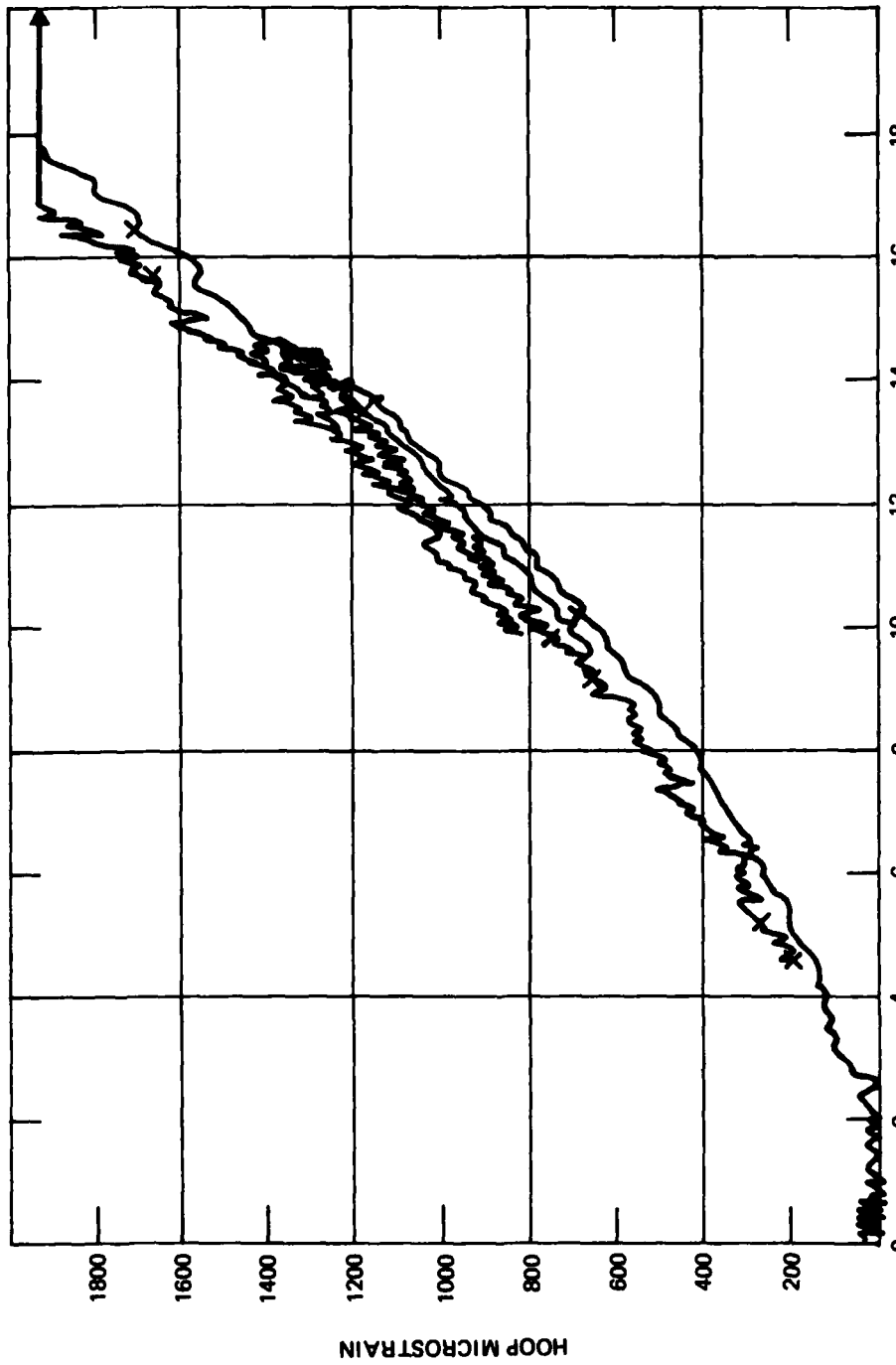

Figure A3 STRAIN vs. SPEED, CHANNEL 1

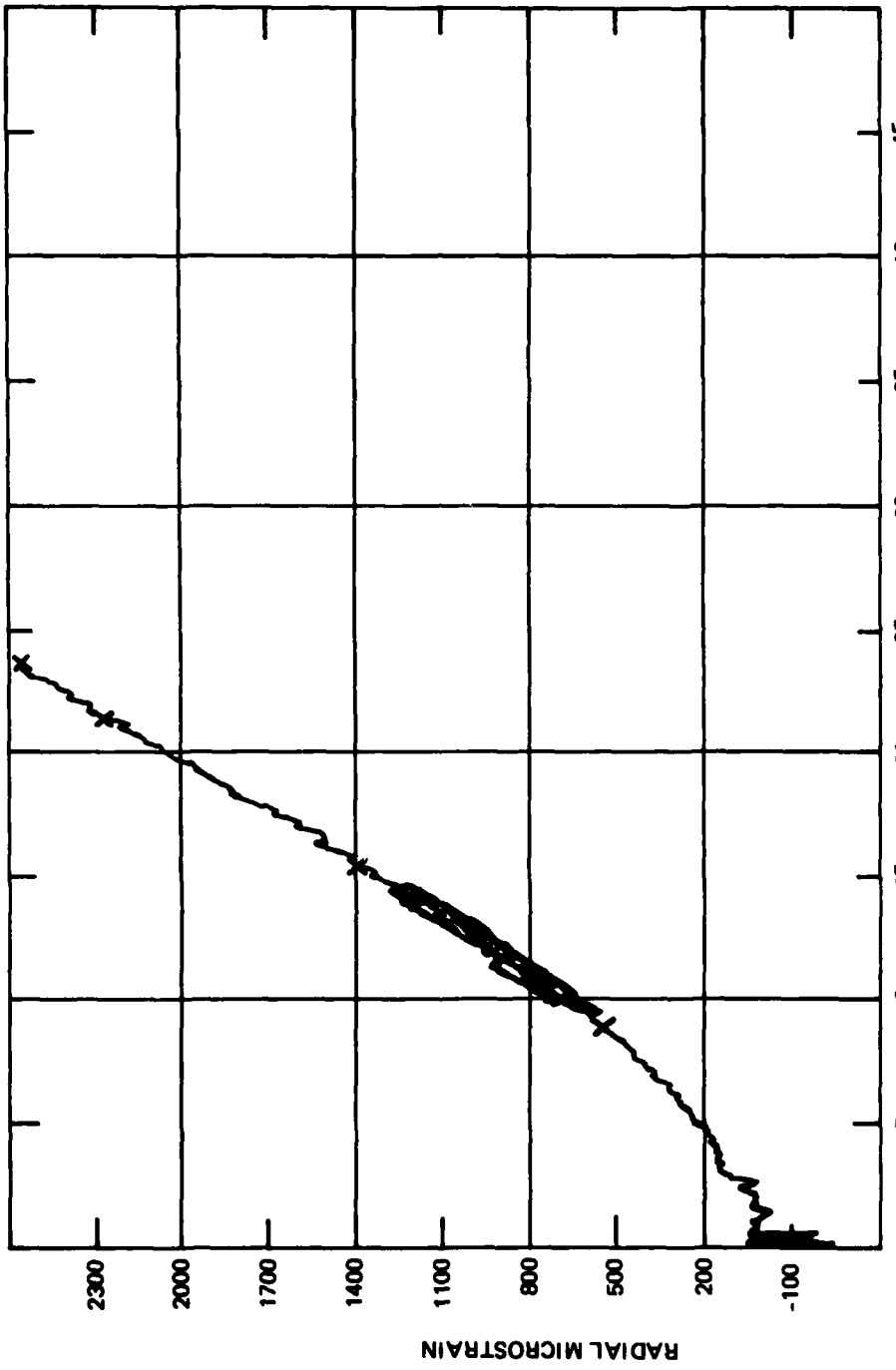

Figure A4 STRAIN vs. SPEED, CHANNEL 2

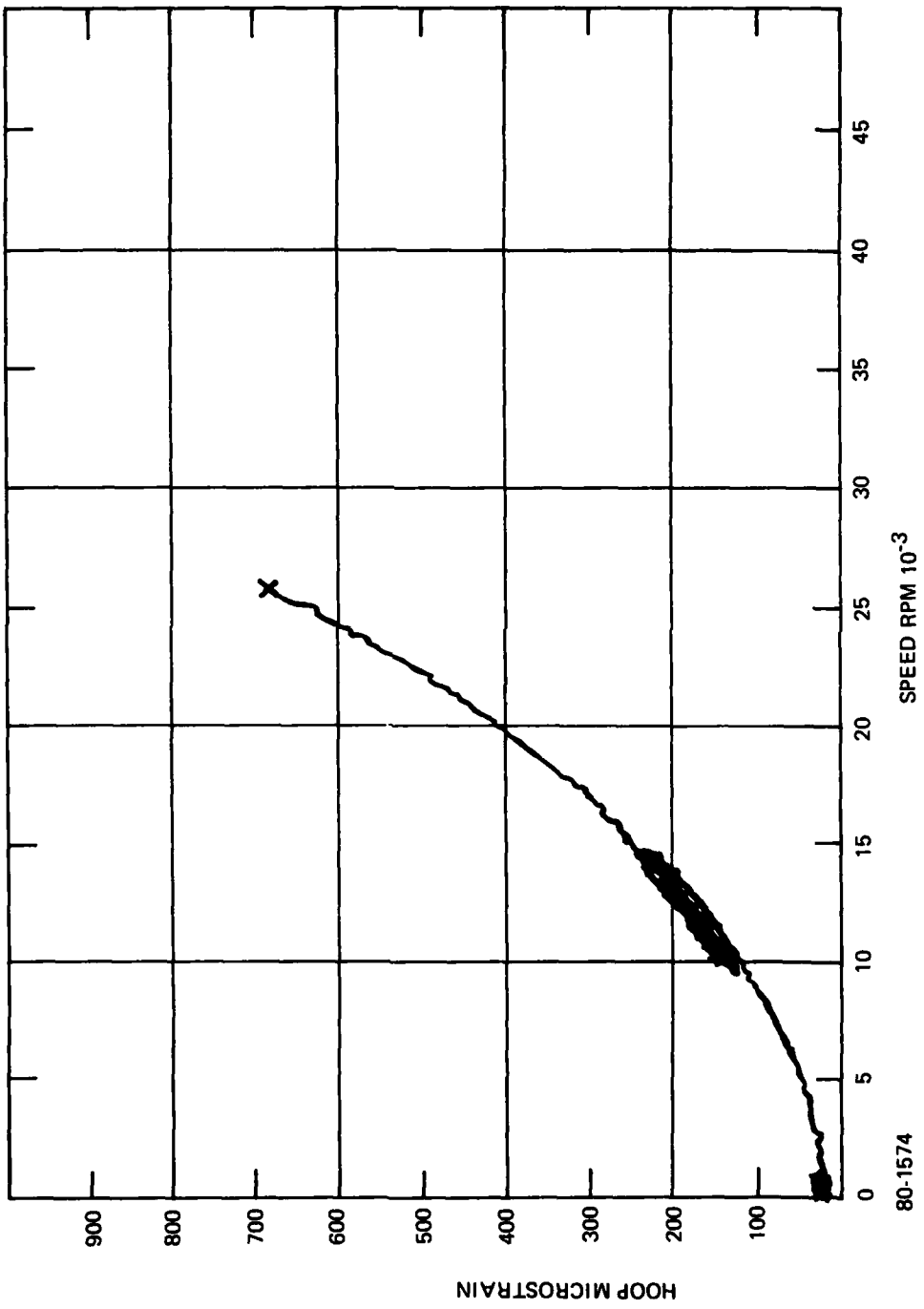

Figure A5 CHANNEL 3 vs. SPEED

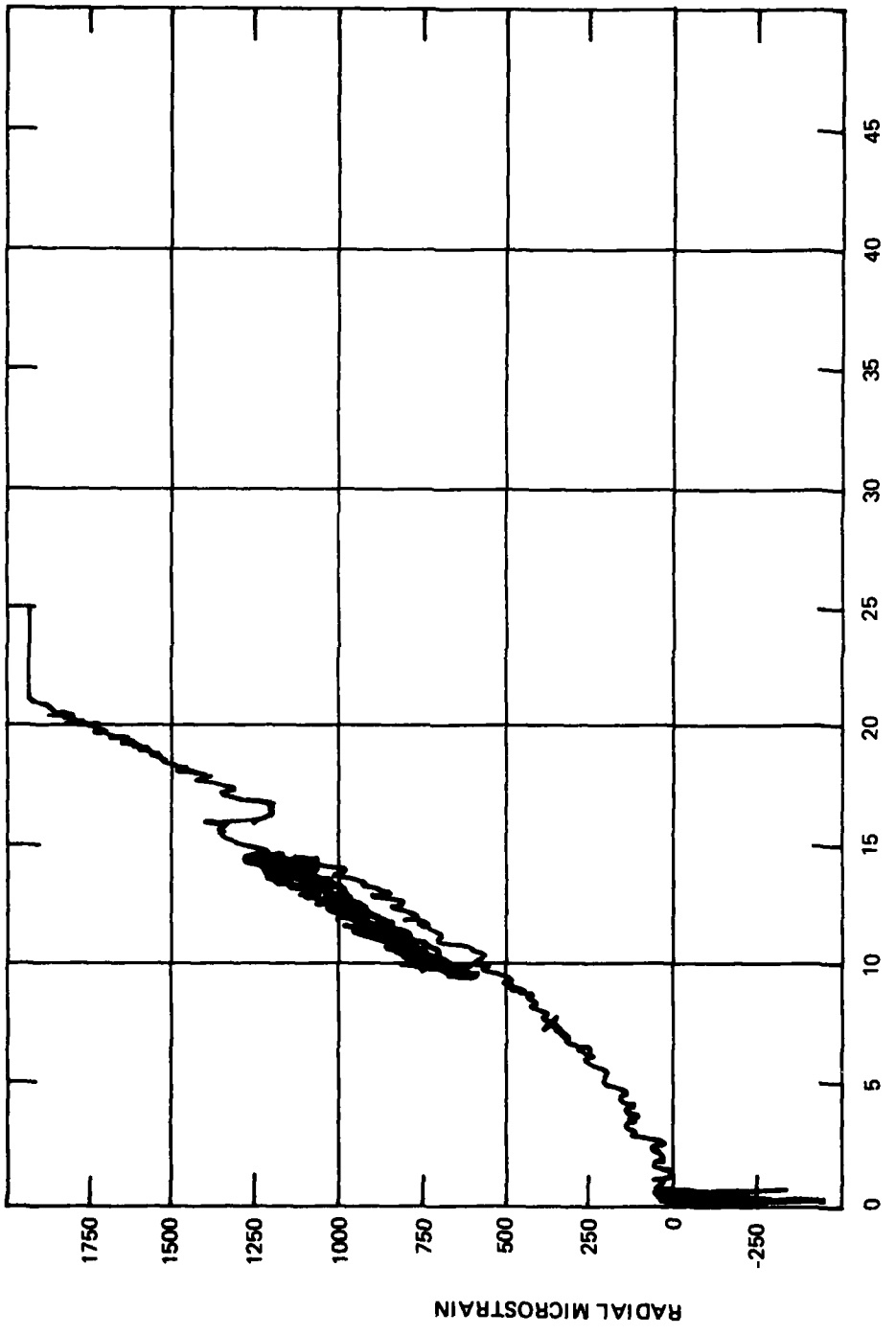

Figure A6 **STRAIN vs. SPEED, CHANNEL 4**

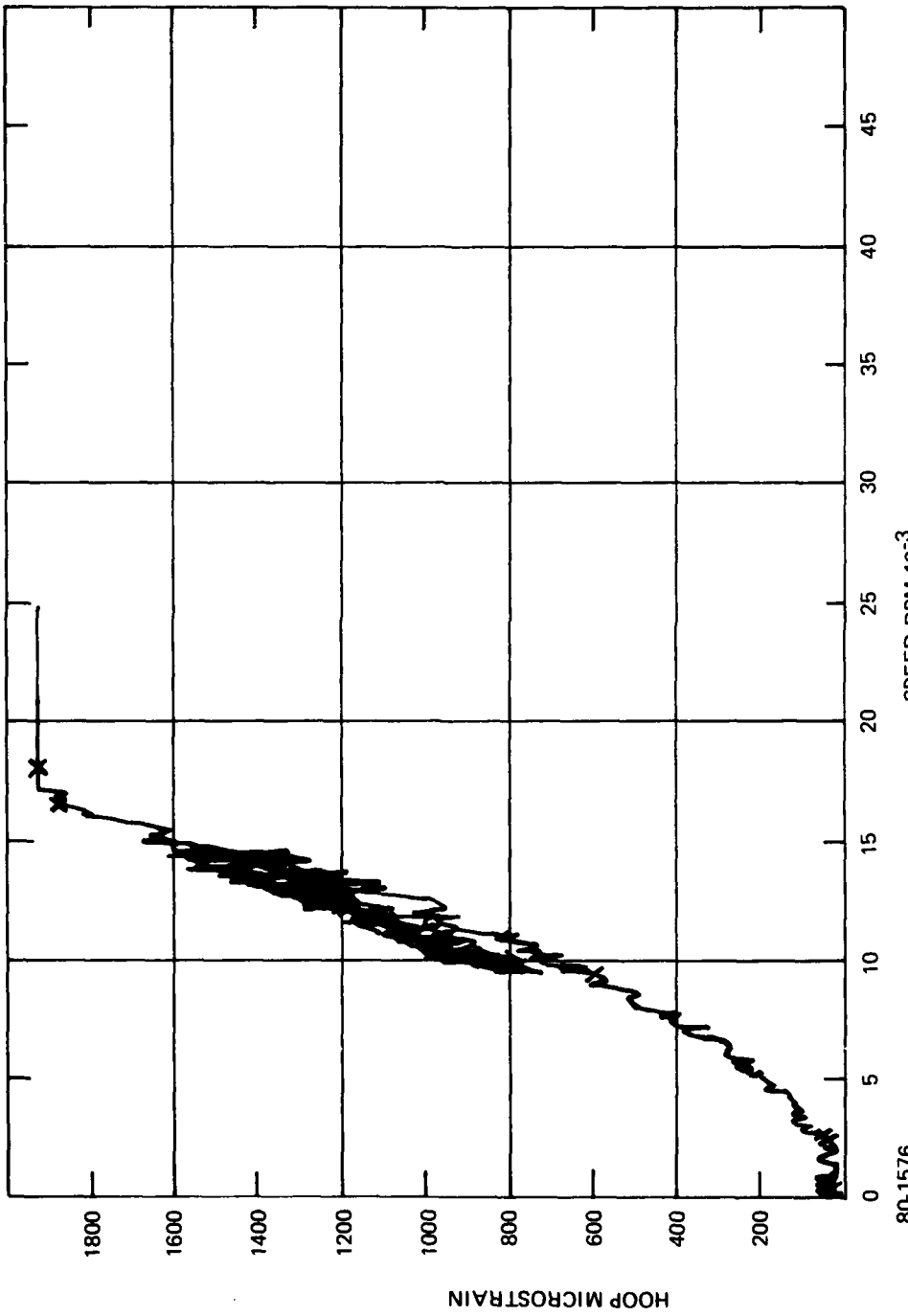

Figure A7 STRAIN vs. SPEED, CHANNEL 5

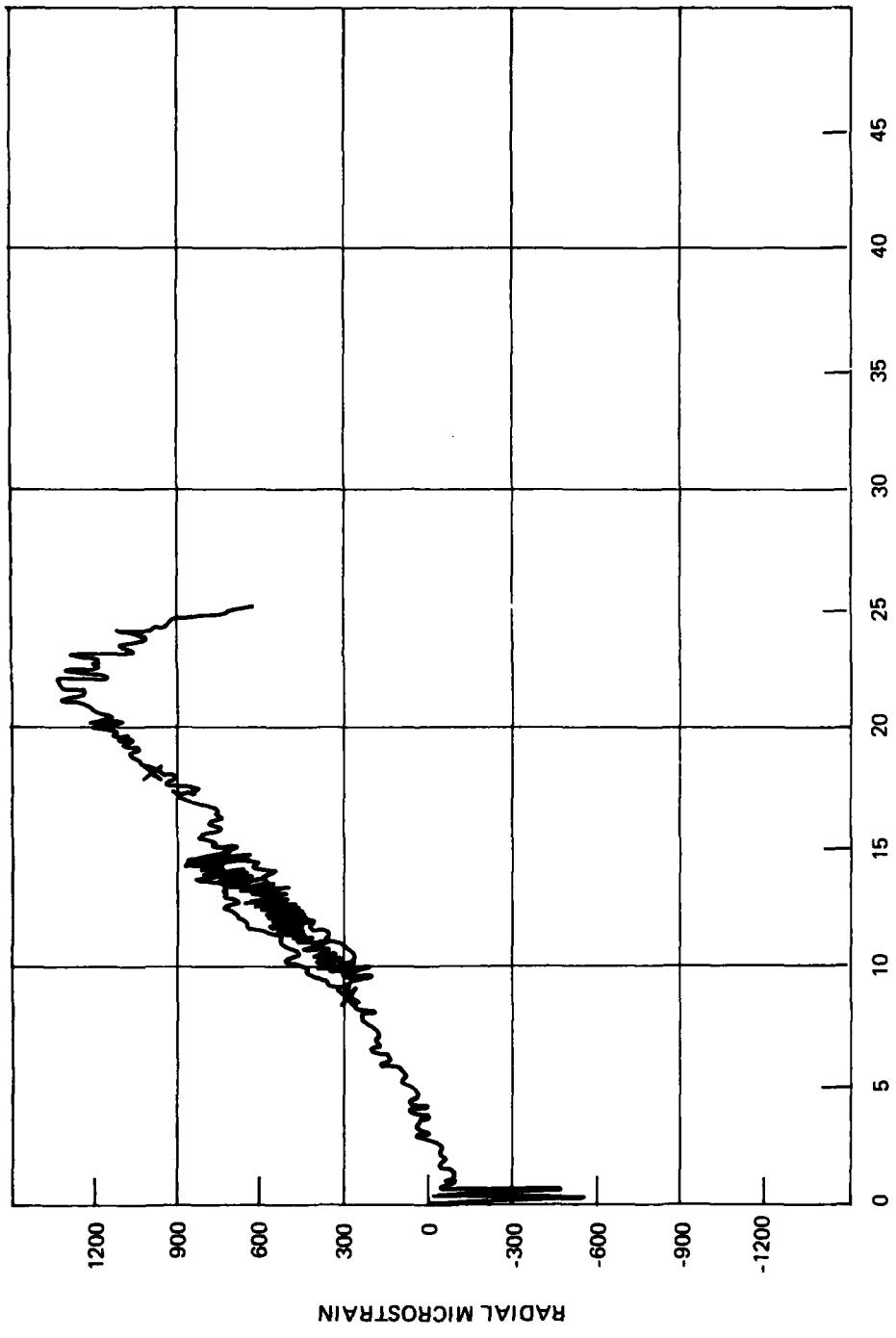

Figure A8 STRAIN VS. SPEED, CHANNEL 6

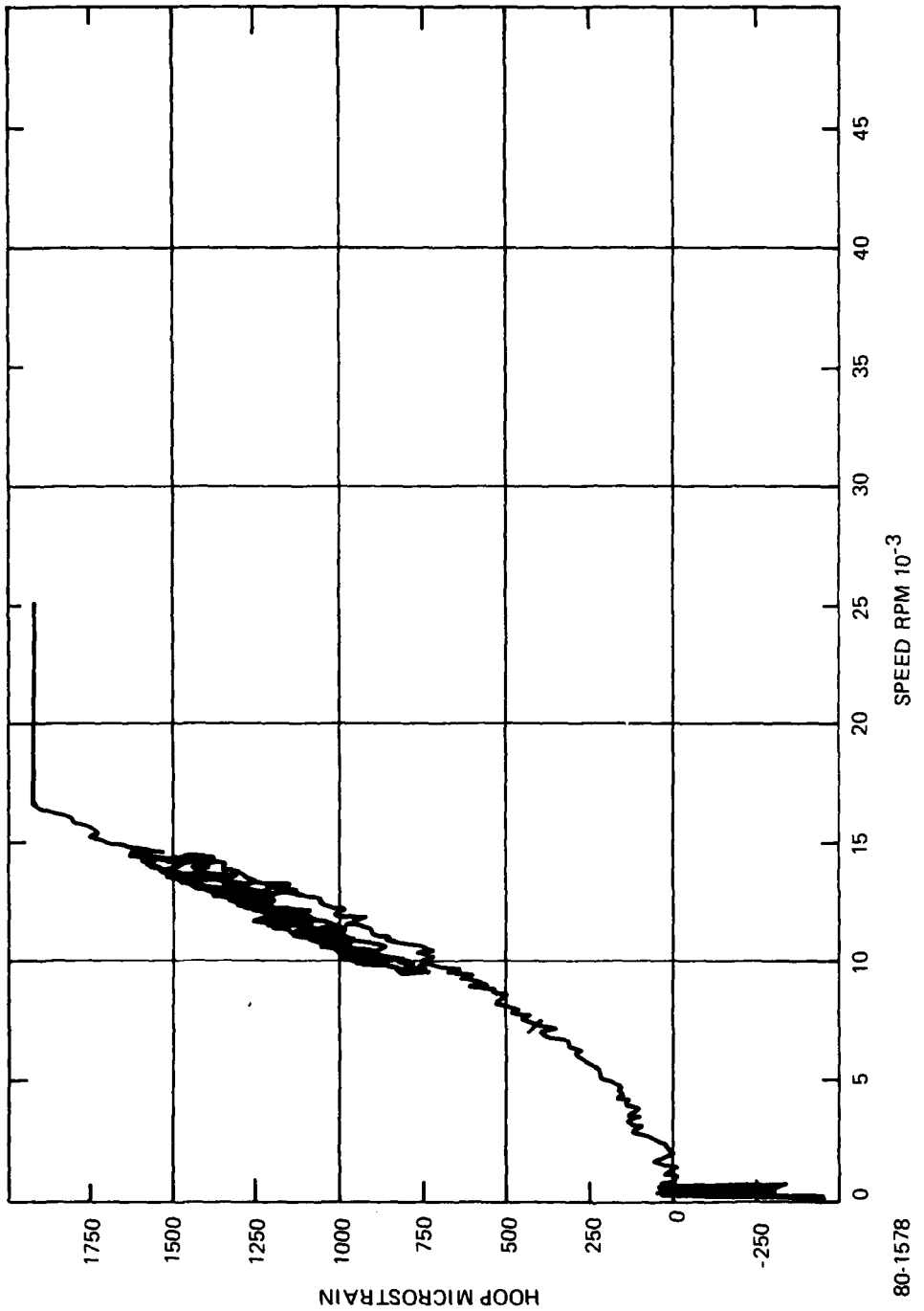

Figure A9 STRAIN vs. SPEED, CHANNEL 7

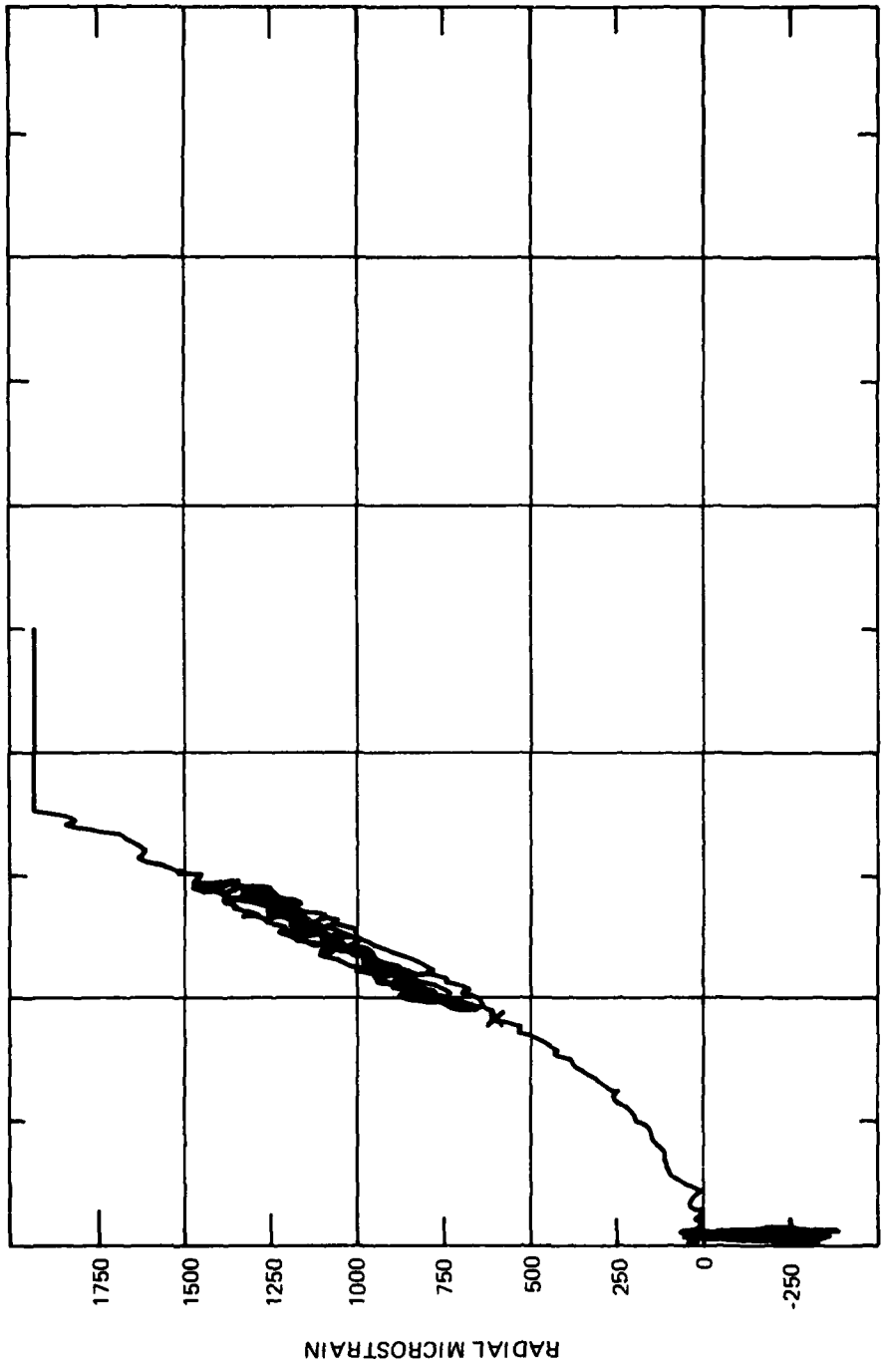

Figure A10 STRAIN vs. SPEED, CHANNEL 8

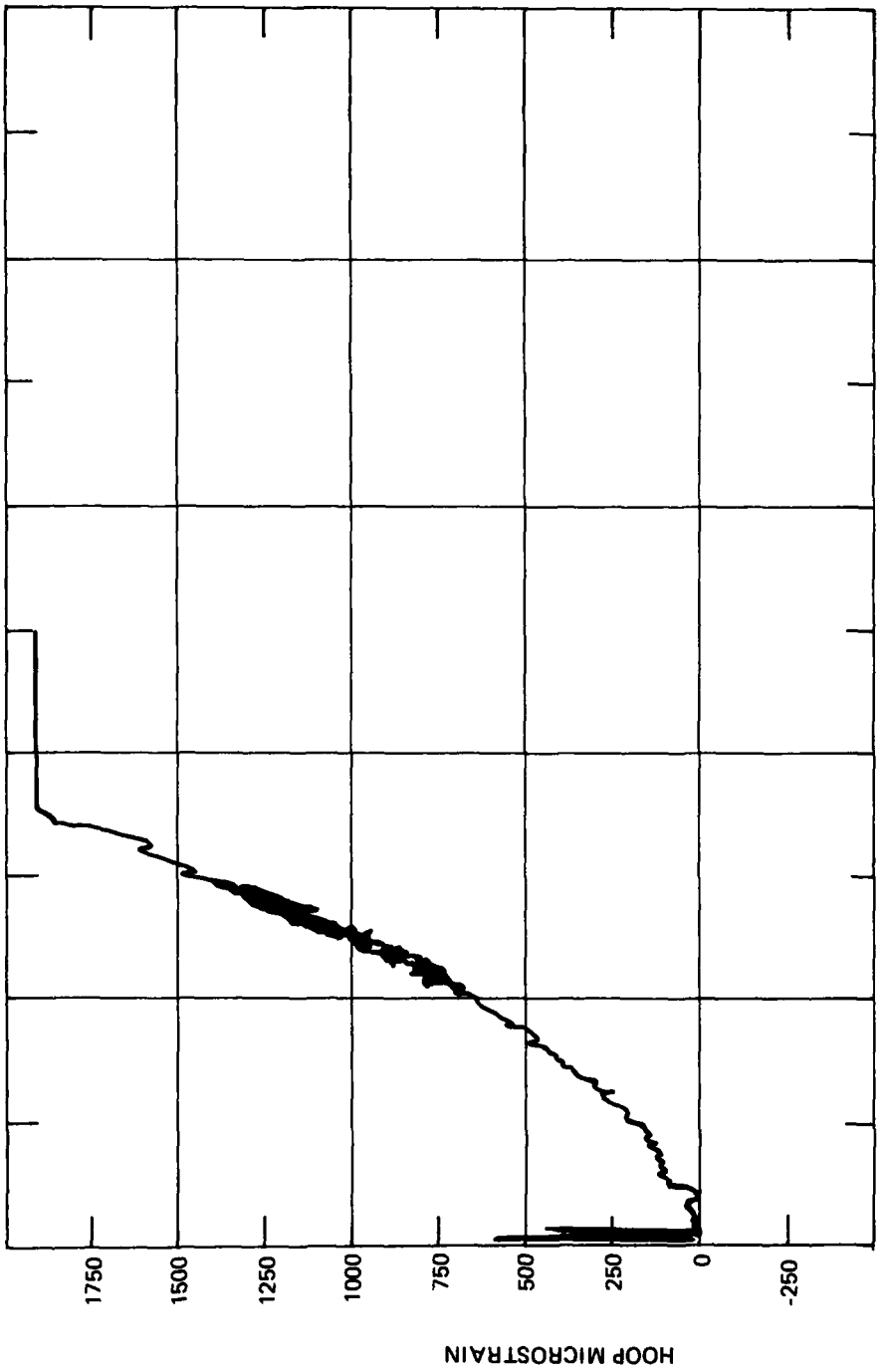

Figure A11 STRAIN vs. SPEED, CHANNEL 9

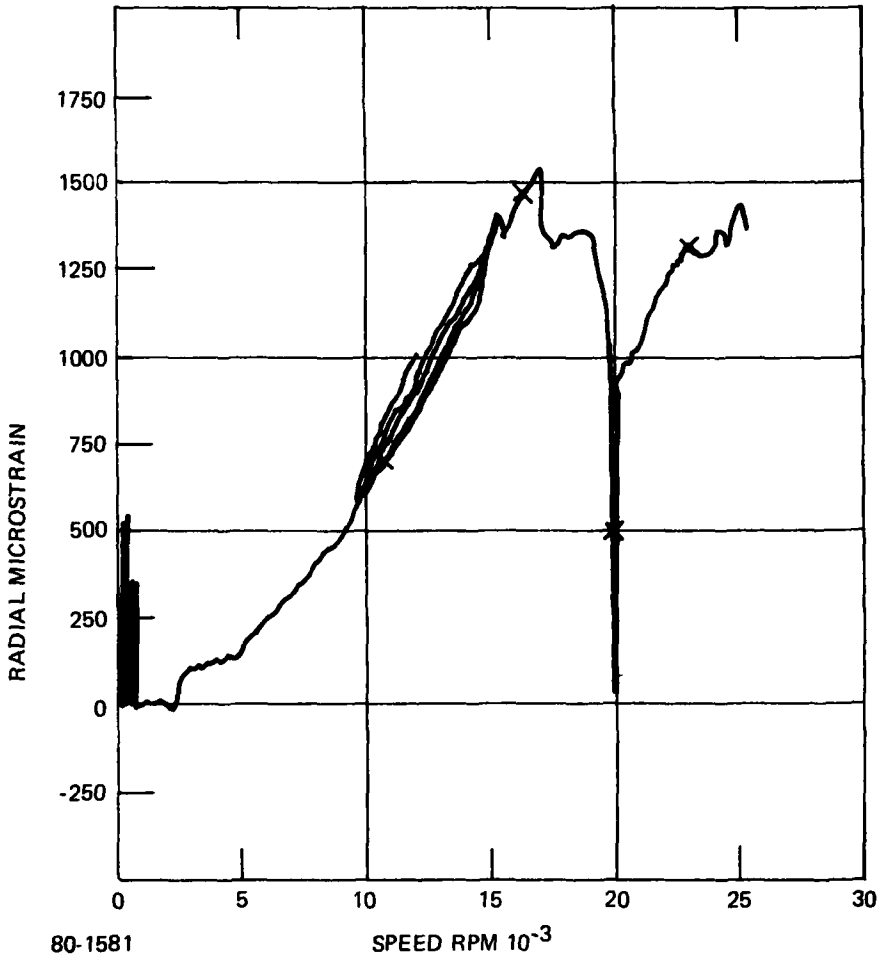

Figure A12 STRAIN vs. SPEED, CHANNEL 10

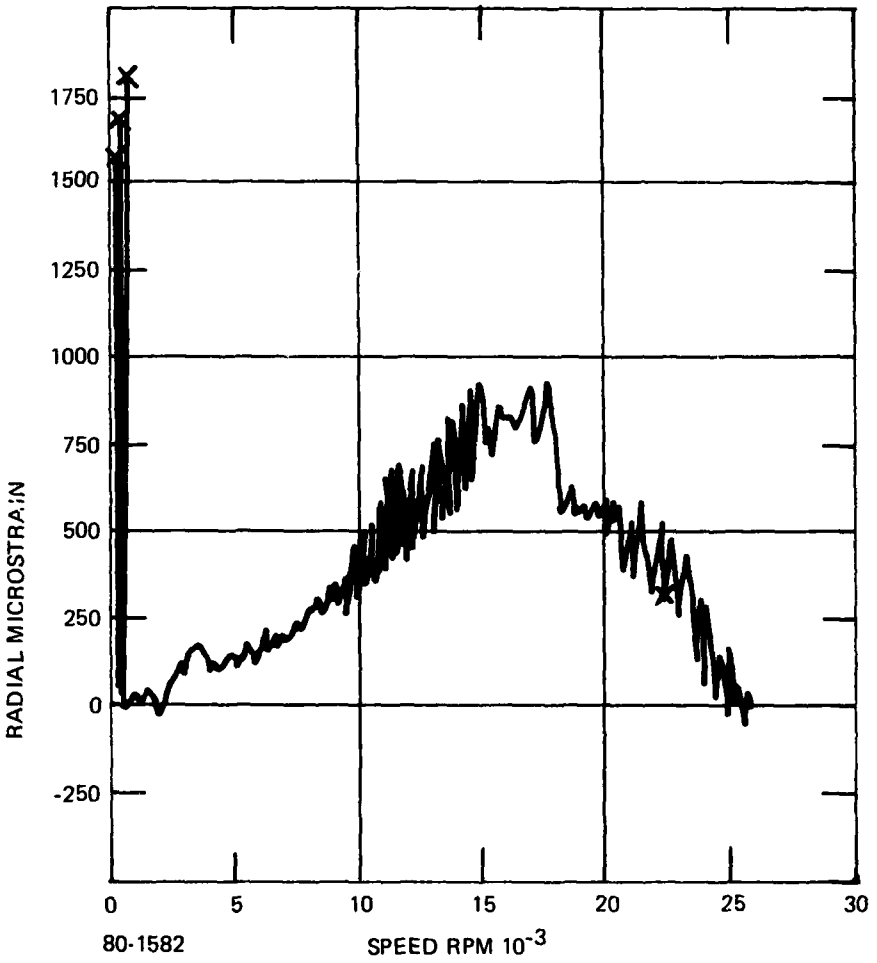

Figure A13 STRAIN vs. SPEED, CHANNEL 11

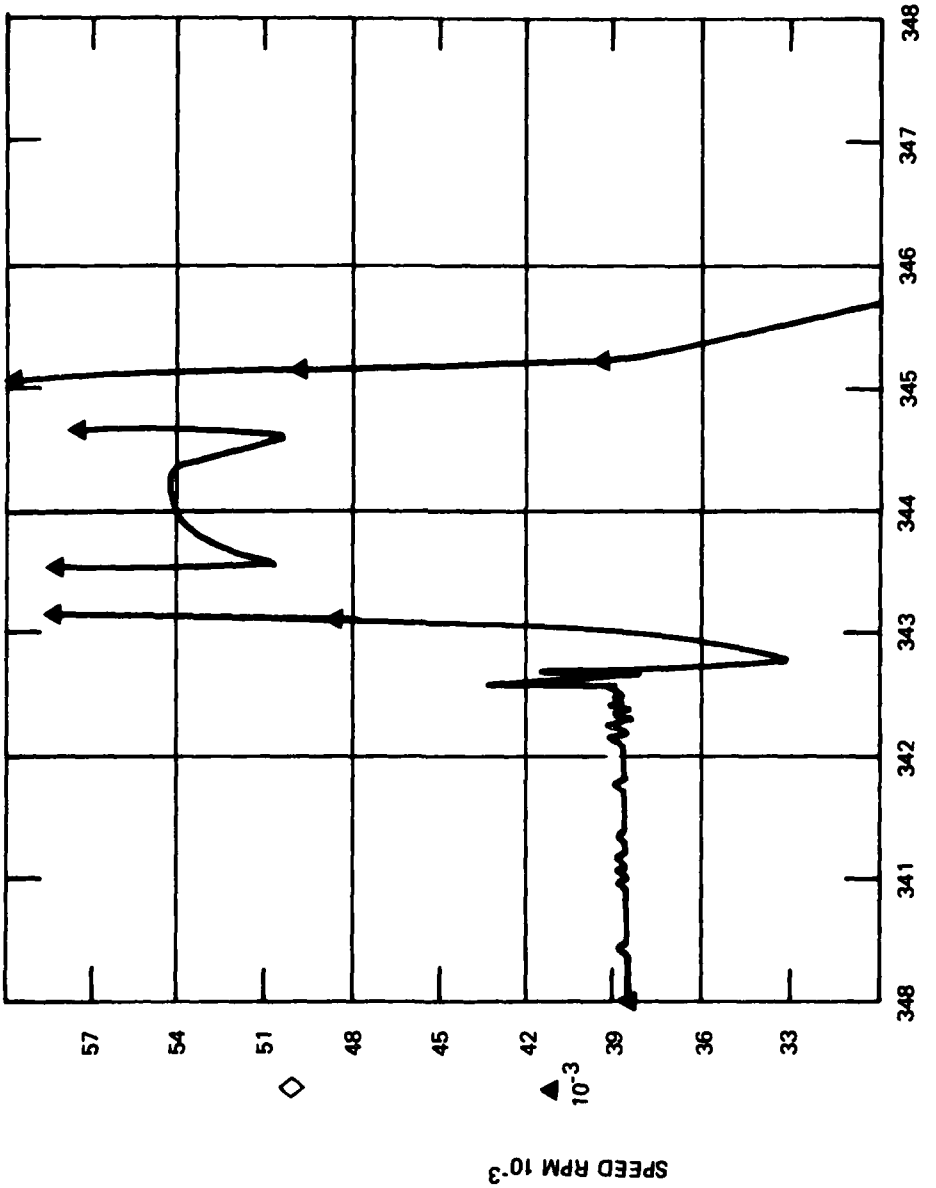

Figure A14 SPEED vs. TIME, RUN 2

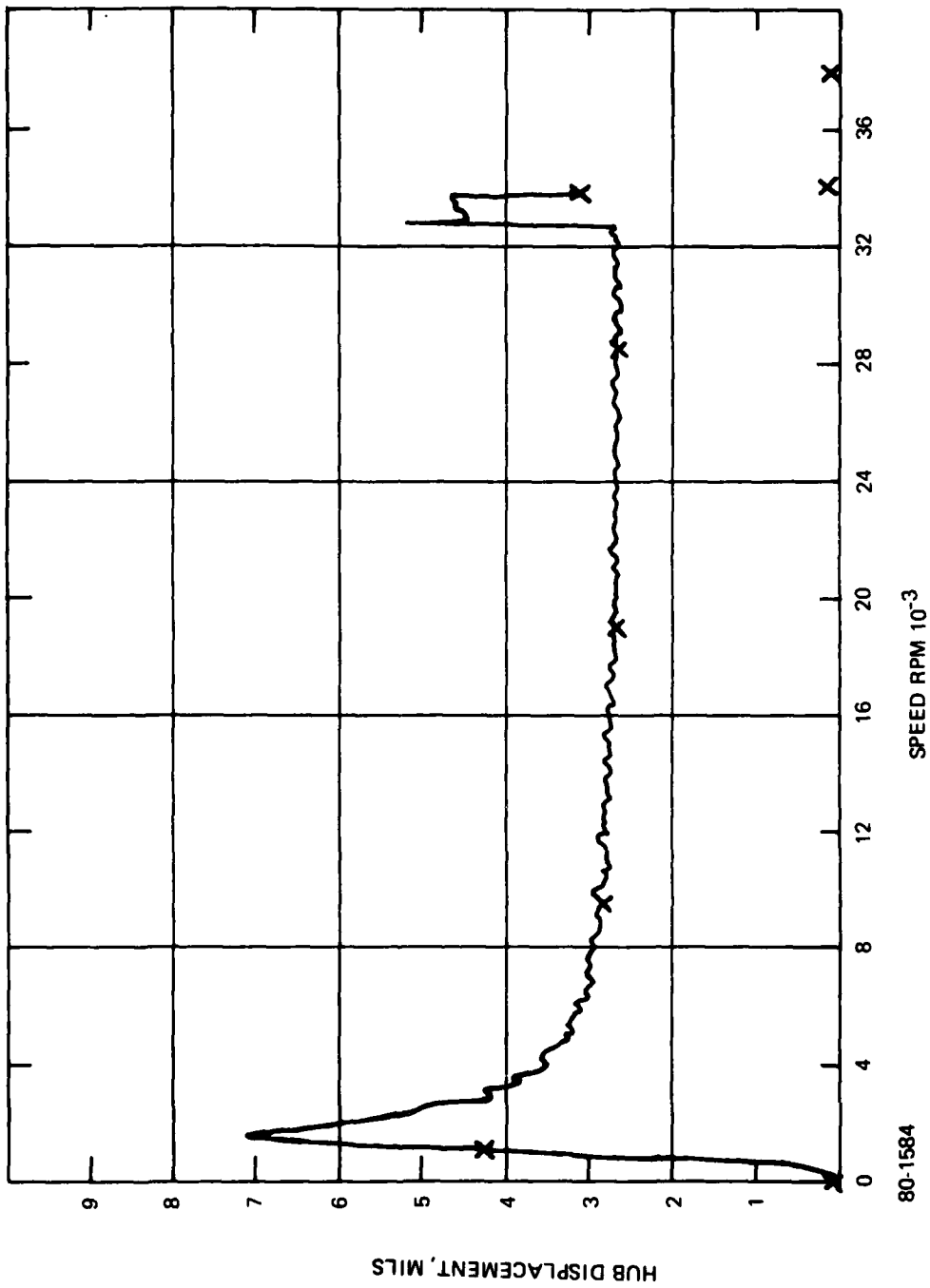

Figure A15 HUB DISPLACEMENT vs. SPEED, RUN 2

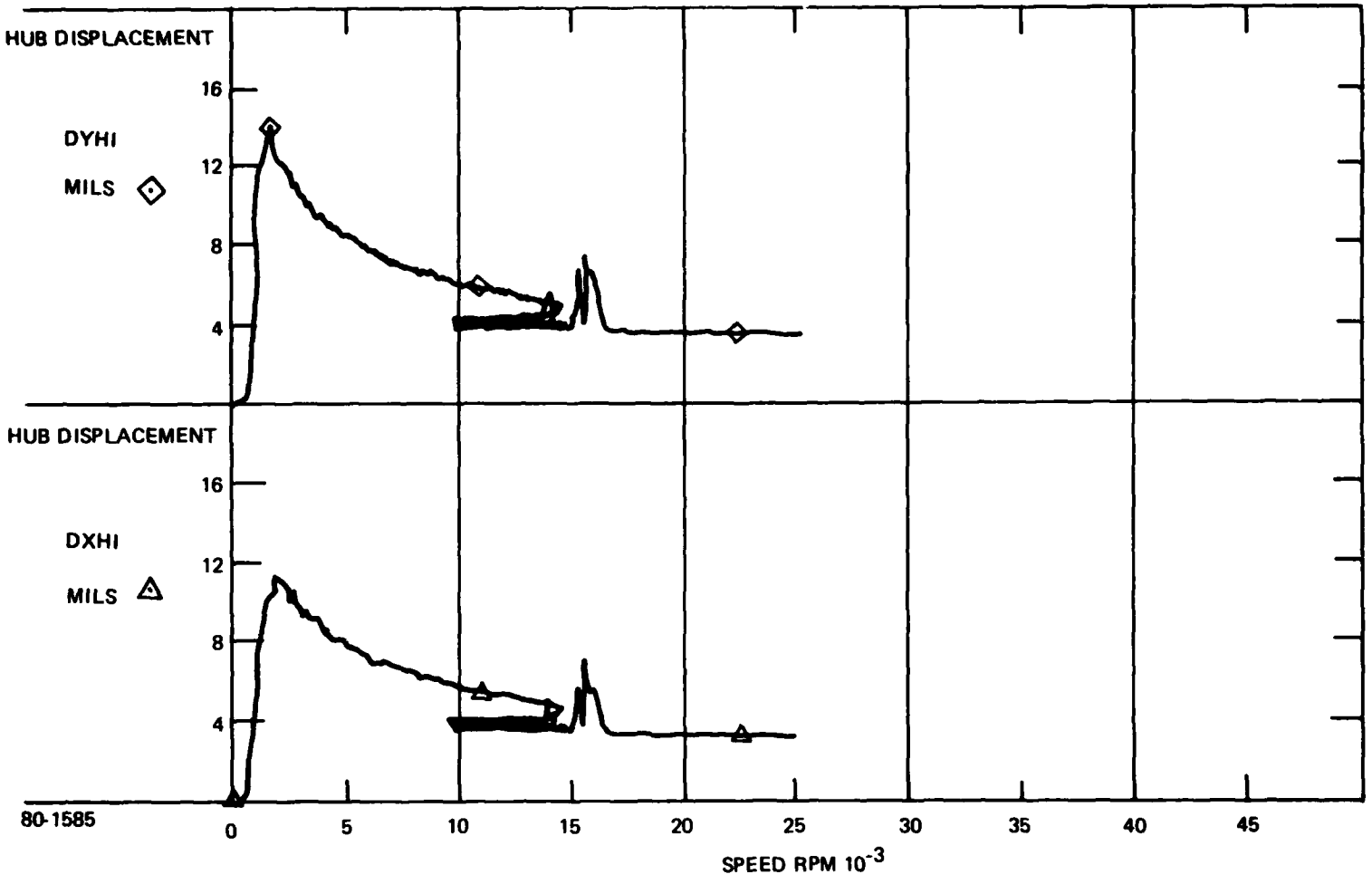

Figure A16 HUB DISPLACEMENT vs. SPEED, RUN 1

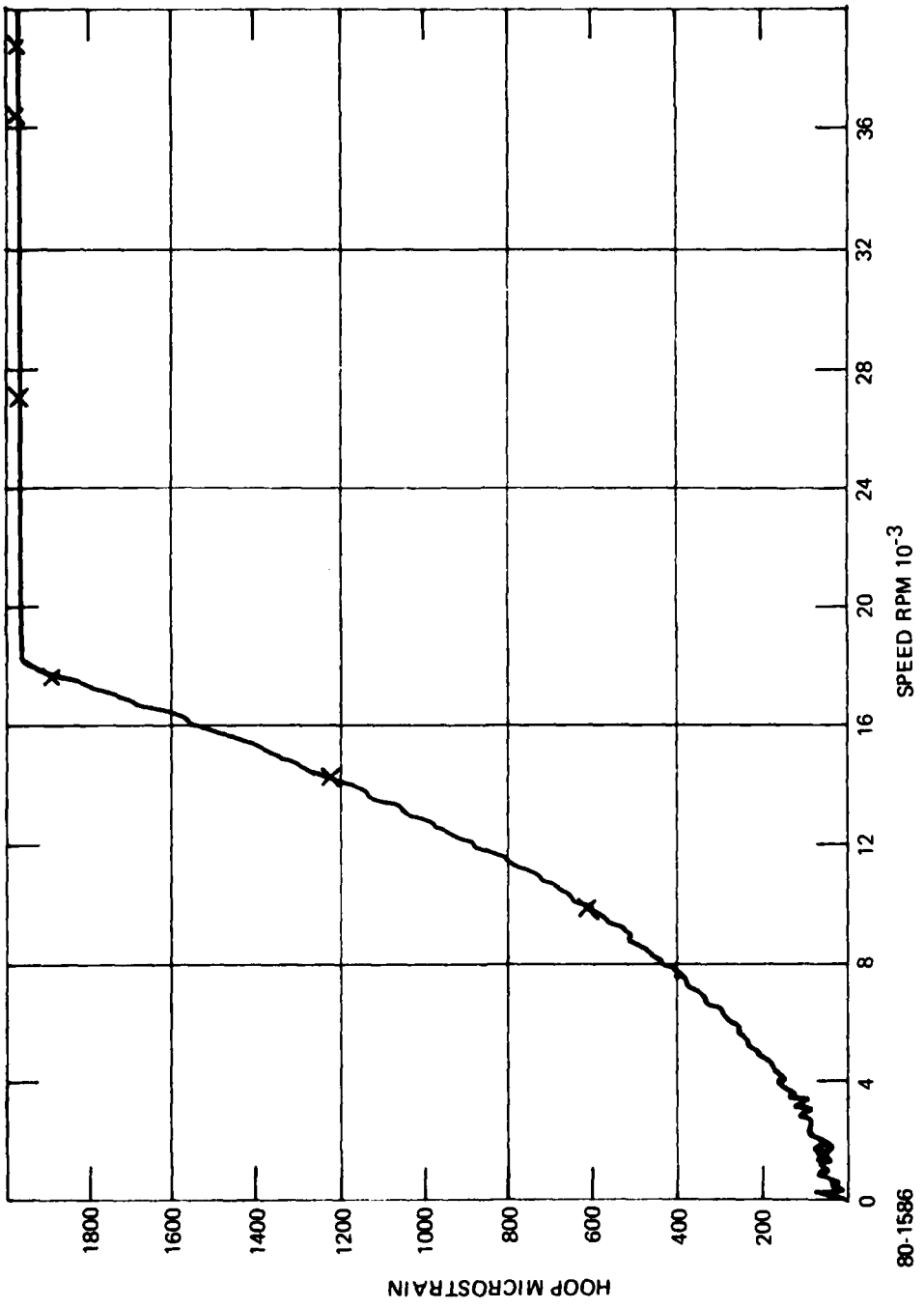

Figure A17 CHANNEL 1 STRAIN vs. SPEED, RUN 2

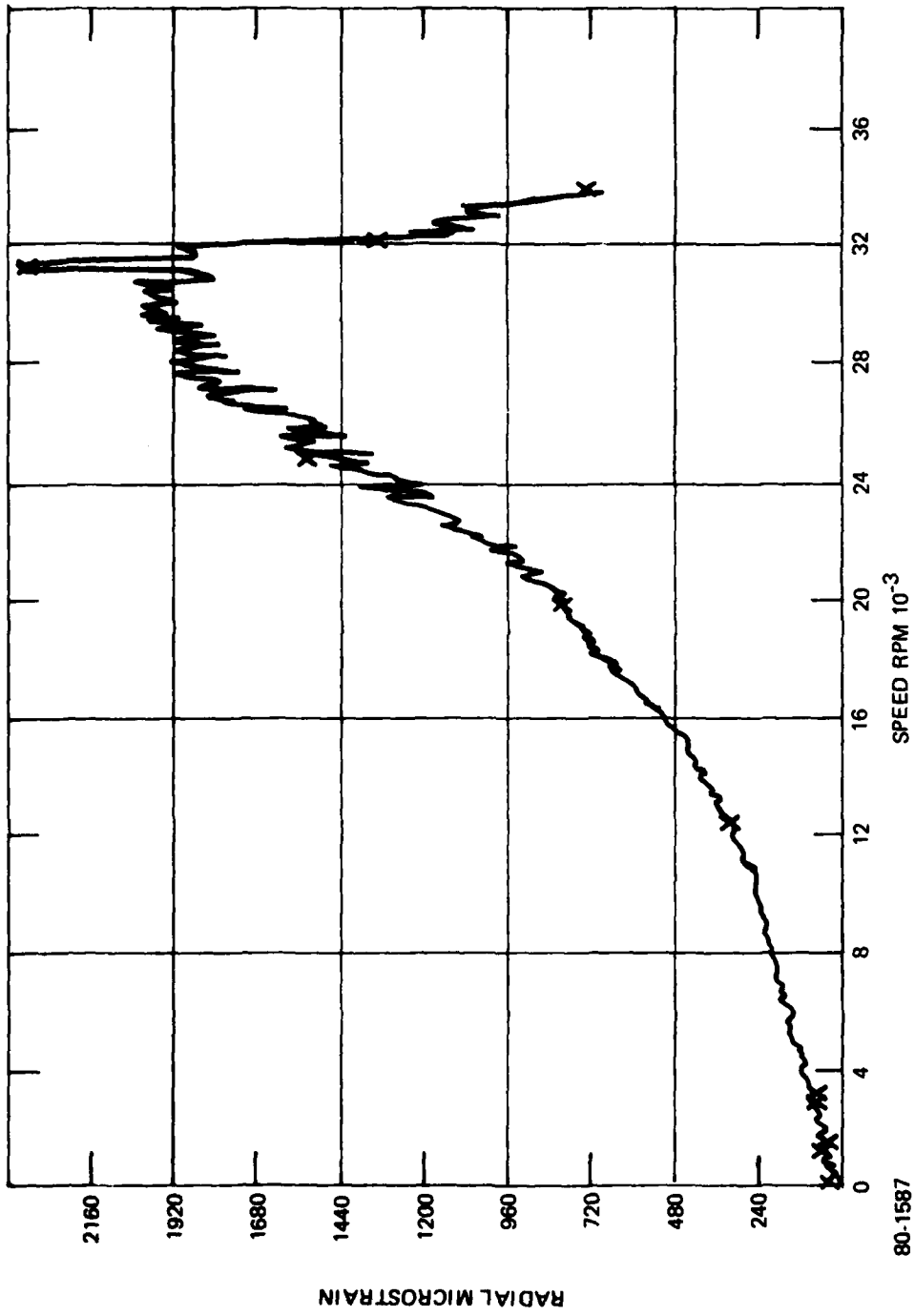

Figure A18 CHANNEL 2 STRAIN vs. SPEED, RUN 2

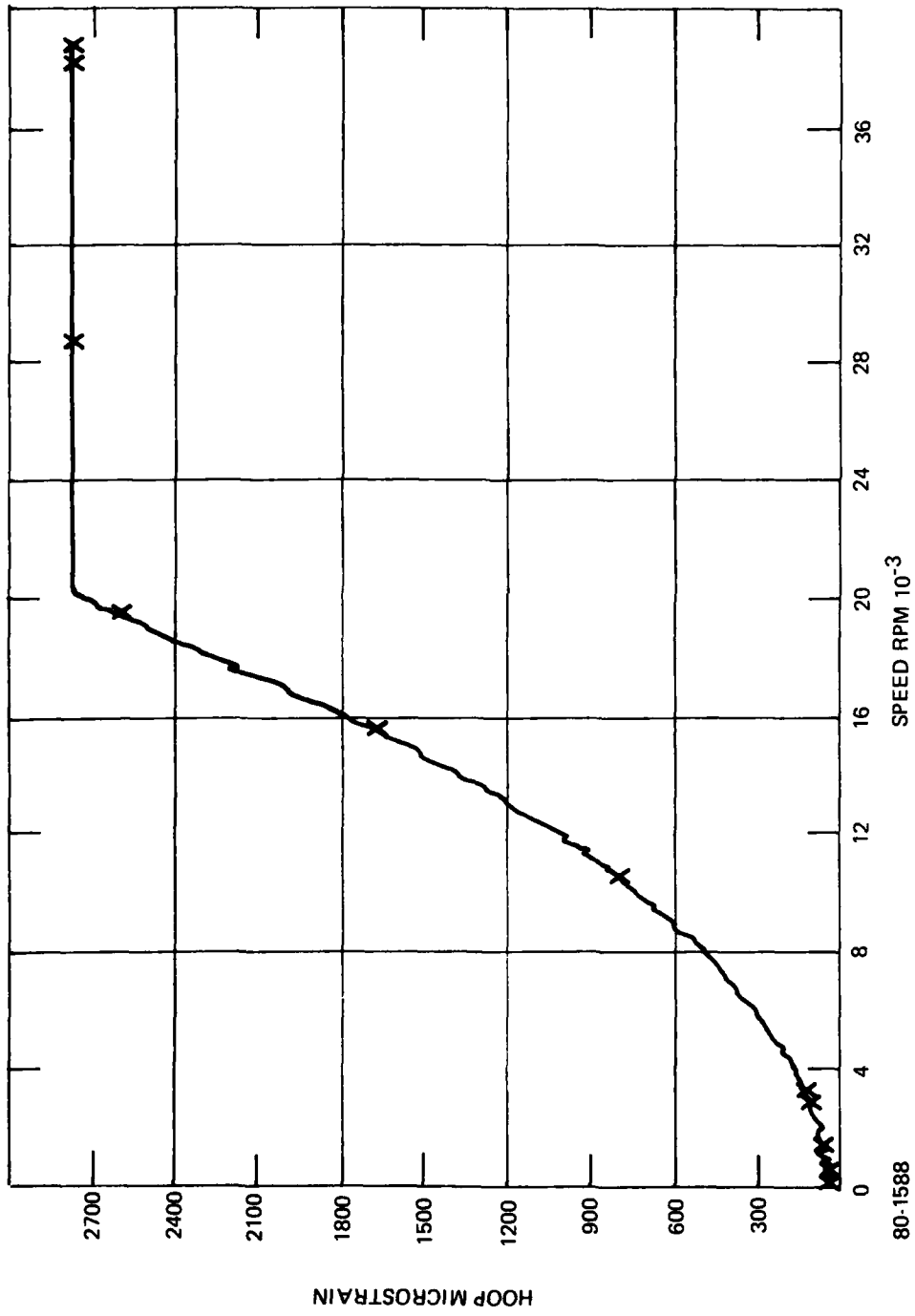

Figure A19 CHANNEL 3 STRAIN vs. SPEED, RUN 2

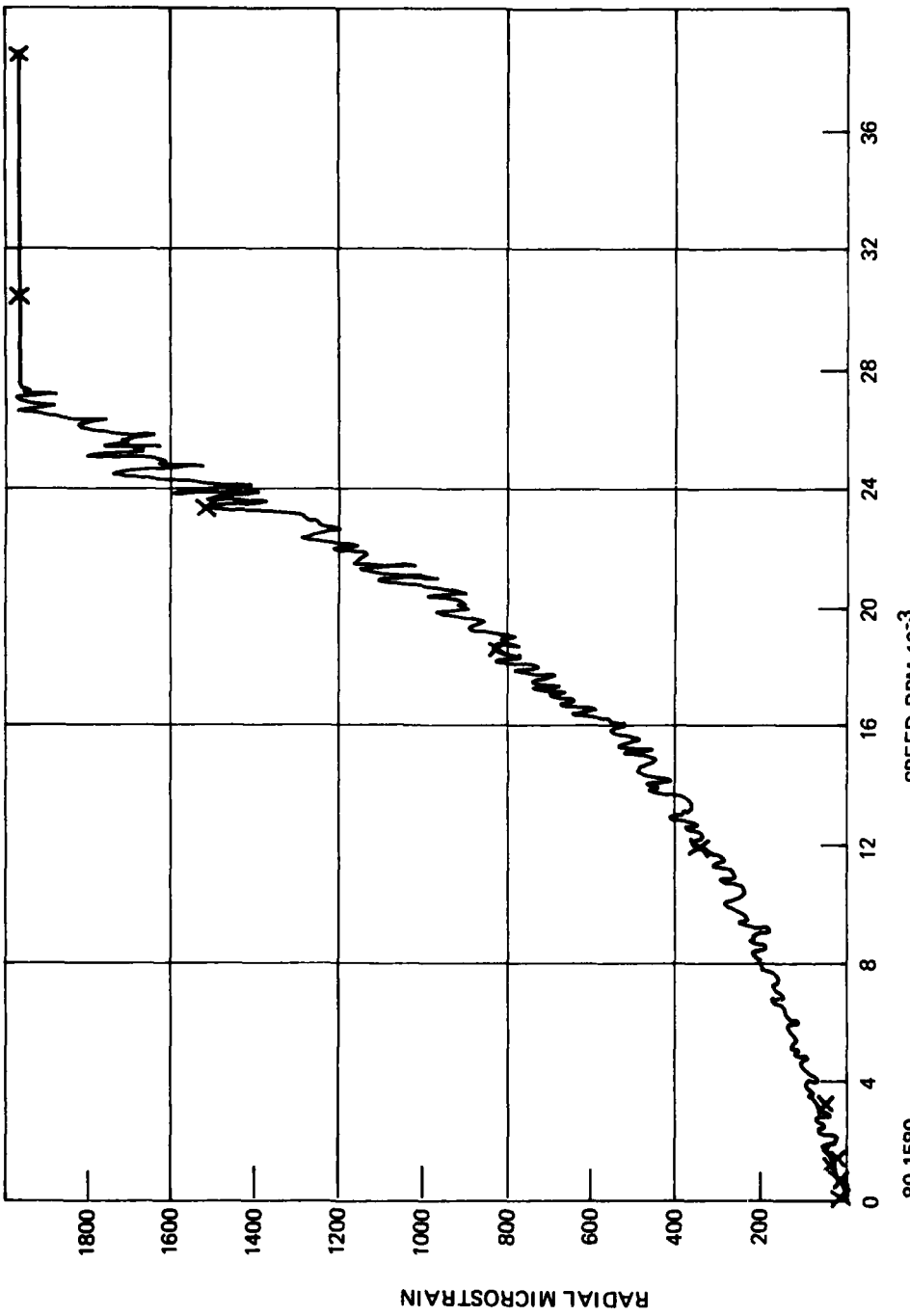

Figure A20 CHANNEL 4 STRAIN vs. SPEED, RUN 2

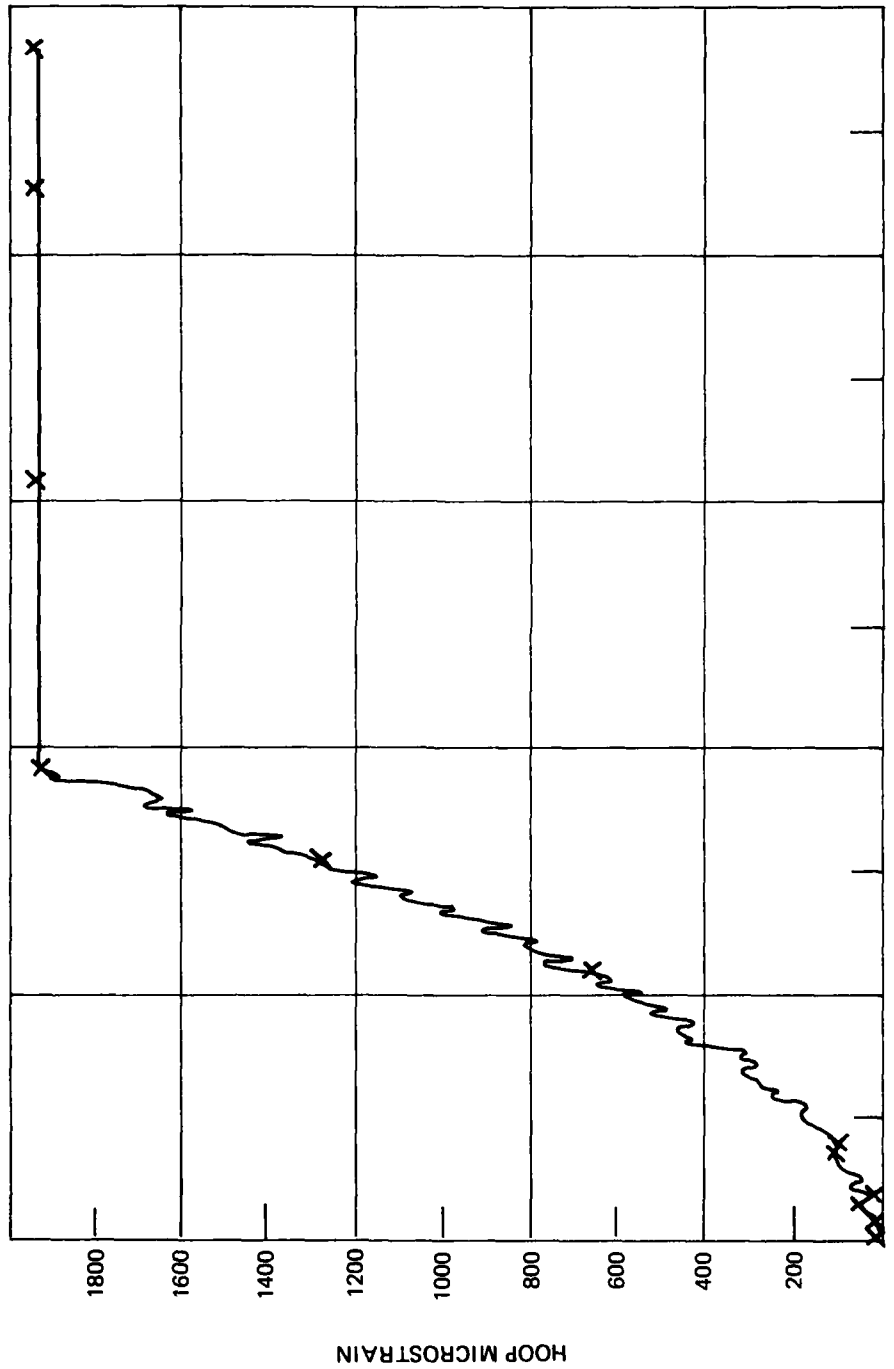

Figure A21 CHANNEL 5 STRAIN vs. SPEED, RUN 2

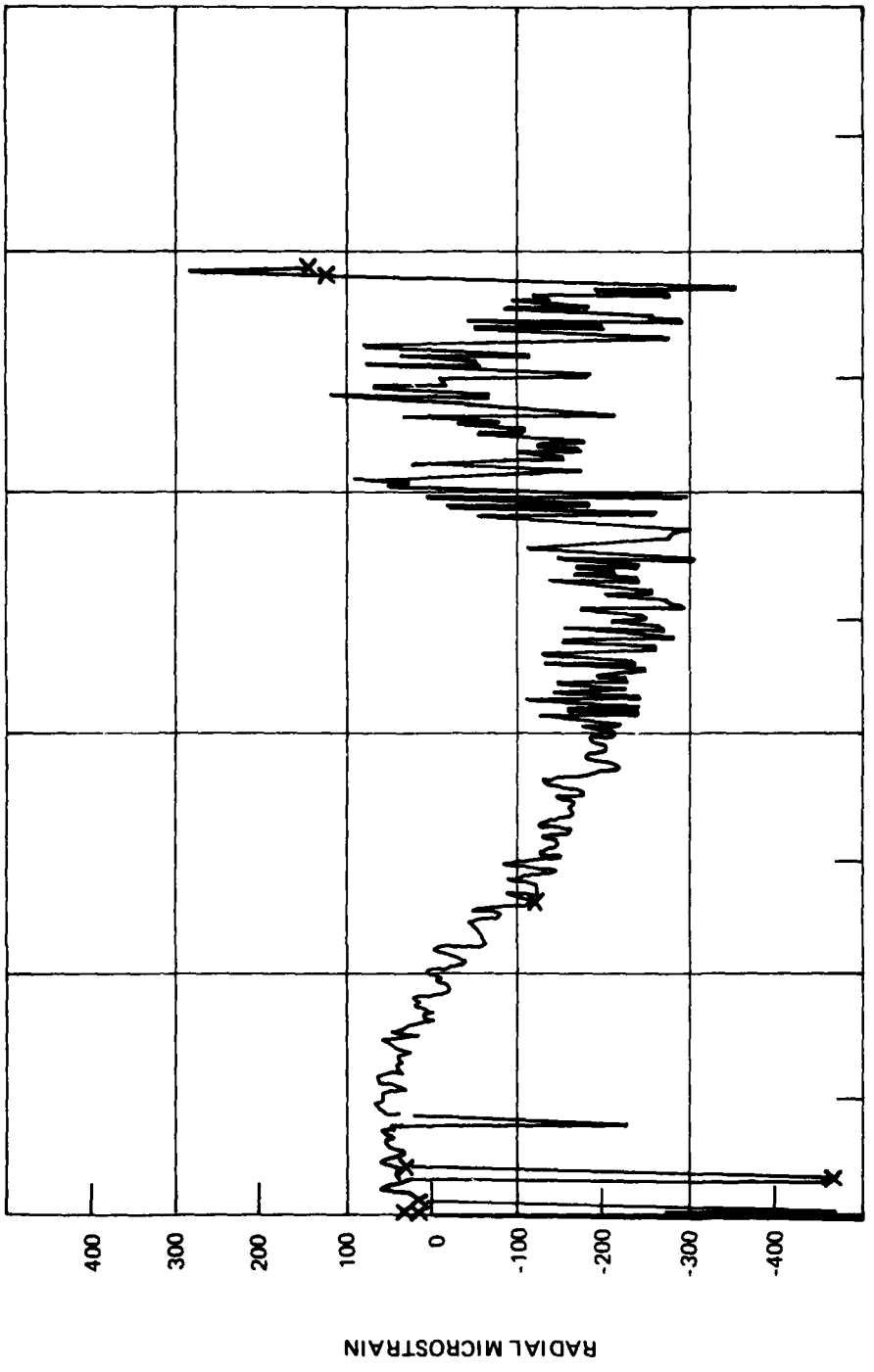

Figure A22 CHANNEL 6 STRAIN vs. SPEED, RUN 2

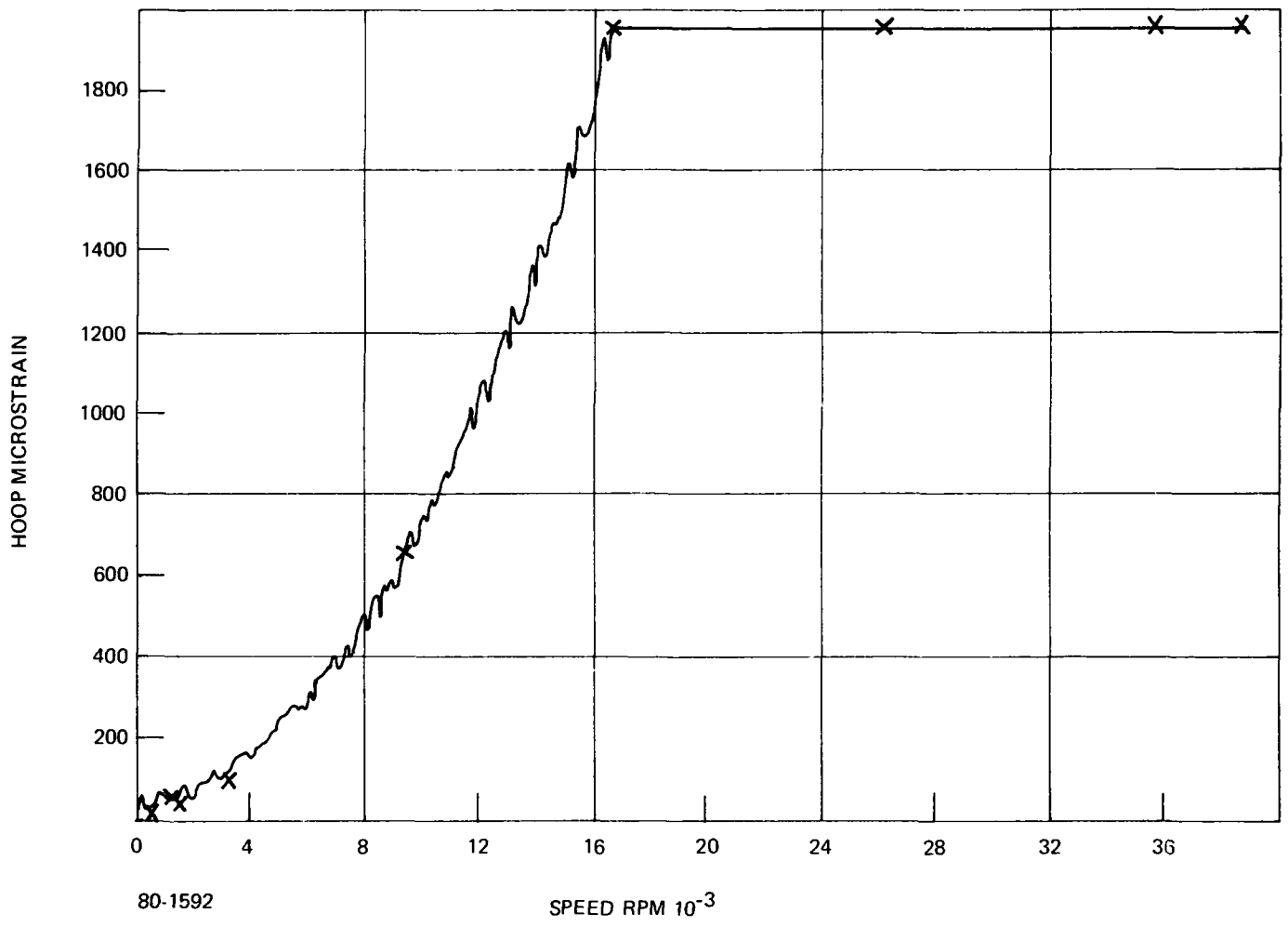

Figure A23 CHANNEL 7 STRAIN vs. SPEED, RUN 2

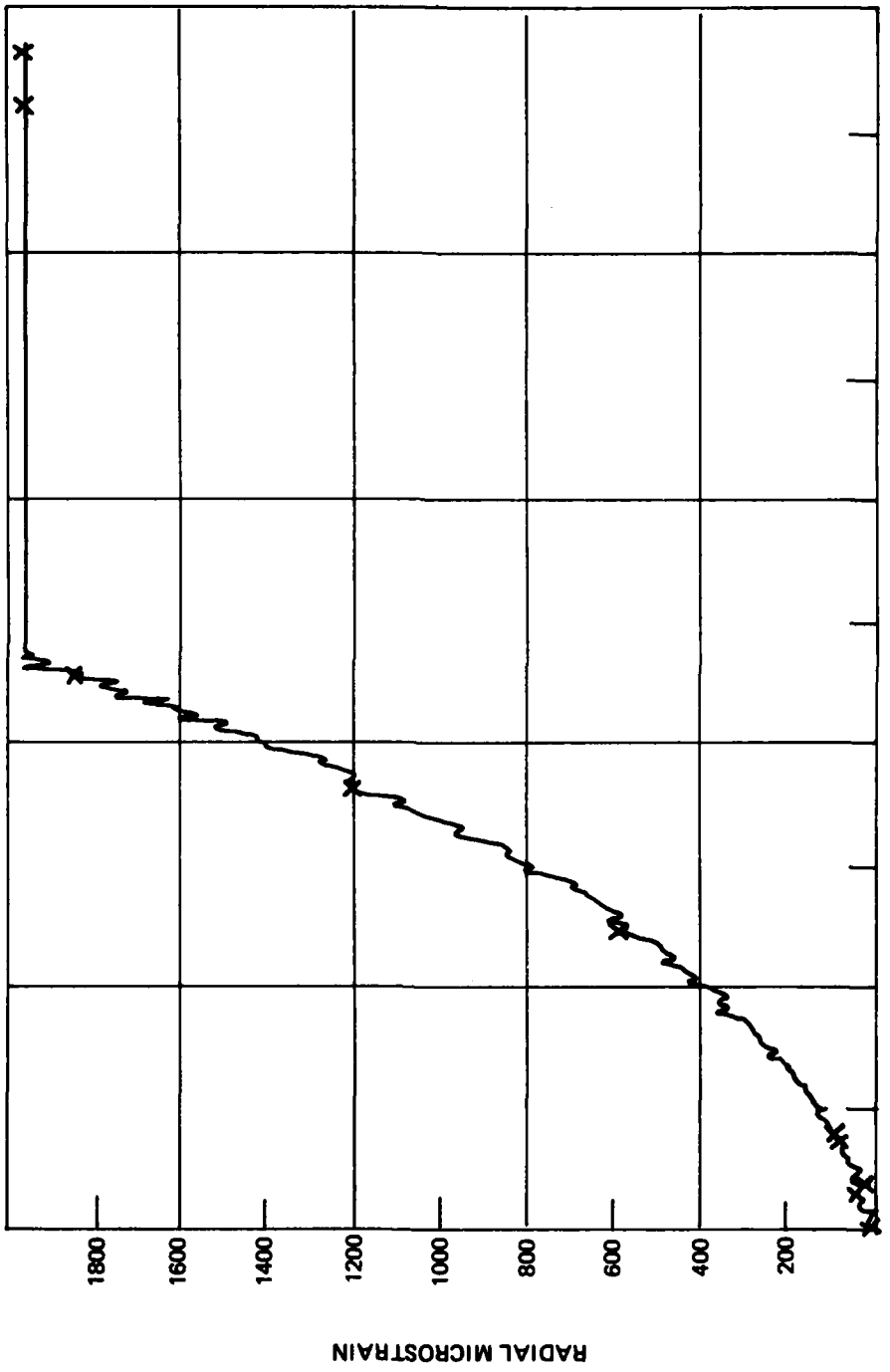

Figure A24 CHANNEL 8 STRAIN vs. SPEED, RUN 2

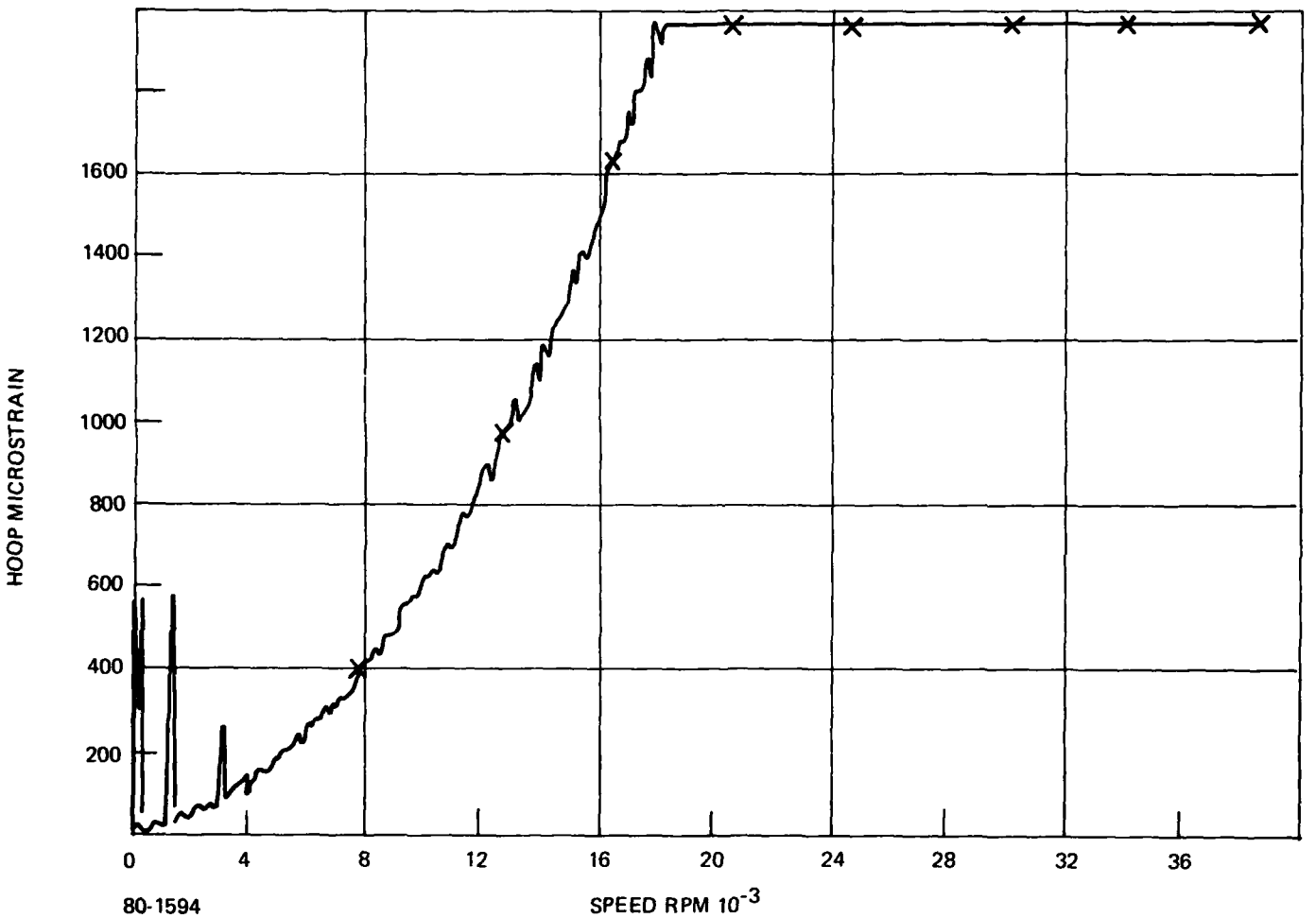

Figure A25 CHANNEL 9 STRAIN vs. SPEED, RUN 2

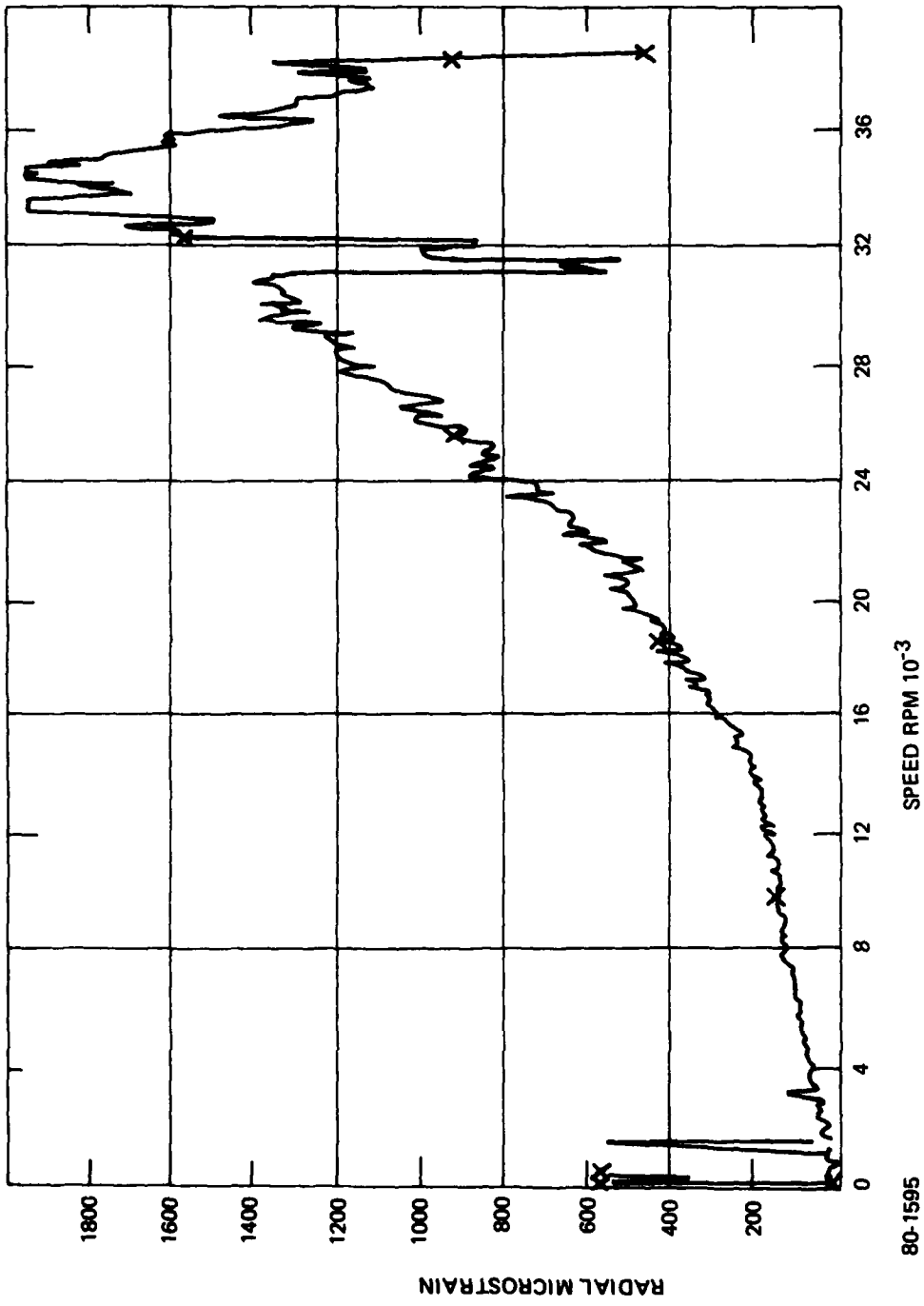

Figure A26 CHANNEL 10 STRAIN vs. SPEED, RUN 2

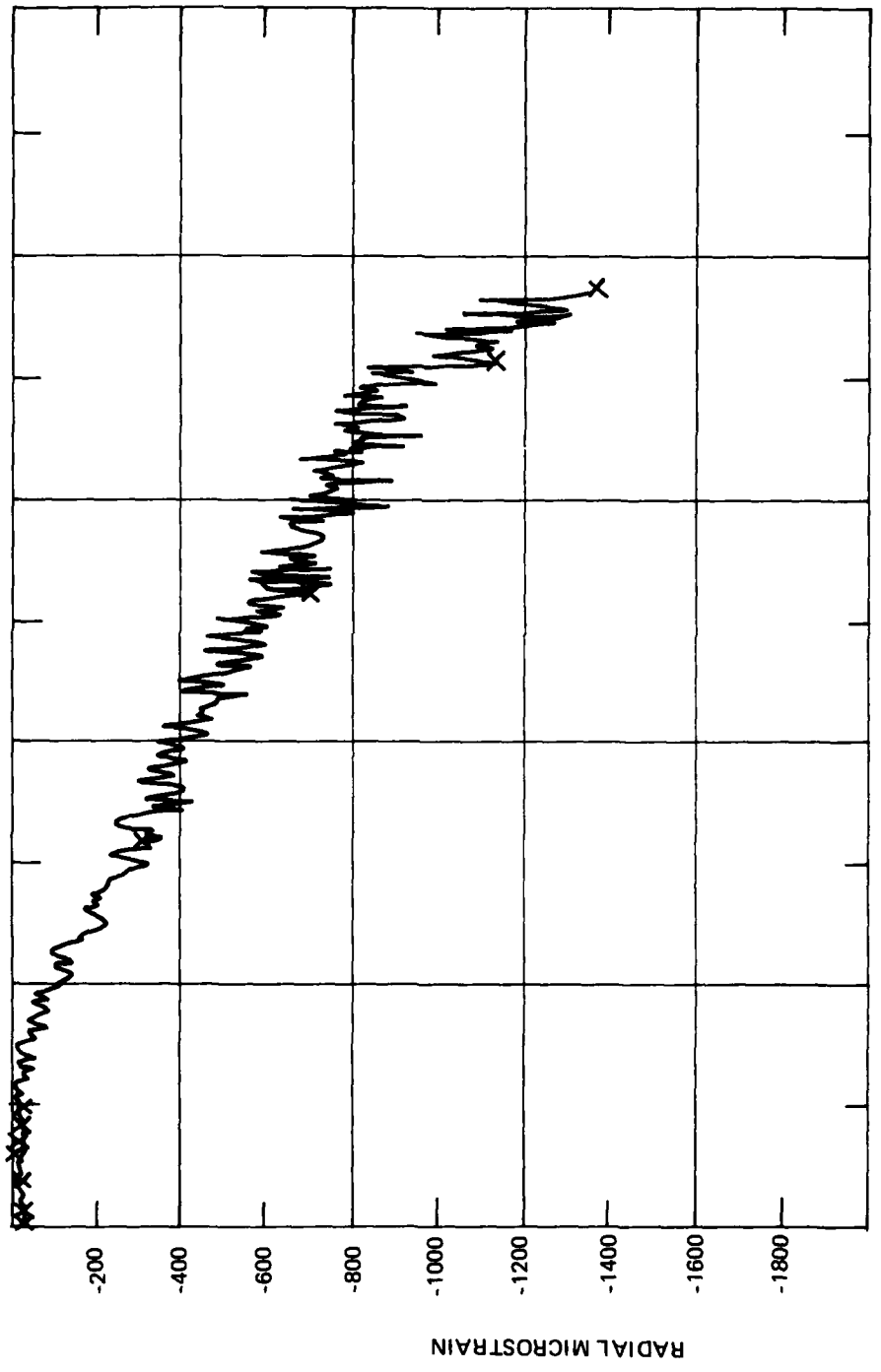

Figure A27 CHANNEL 11 STRAIN vs. SPEED, RUN 2

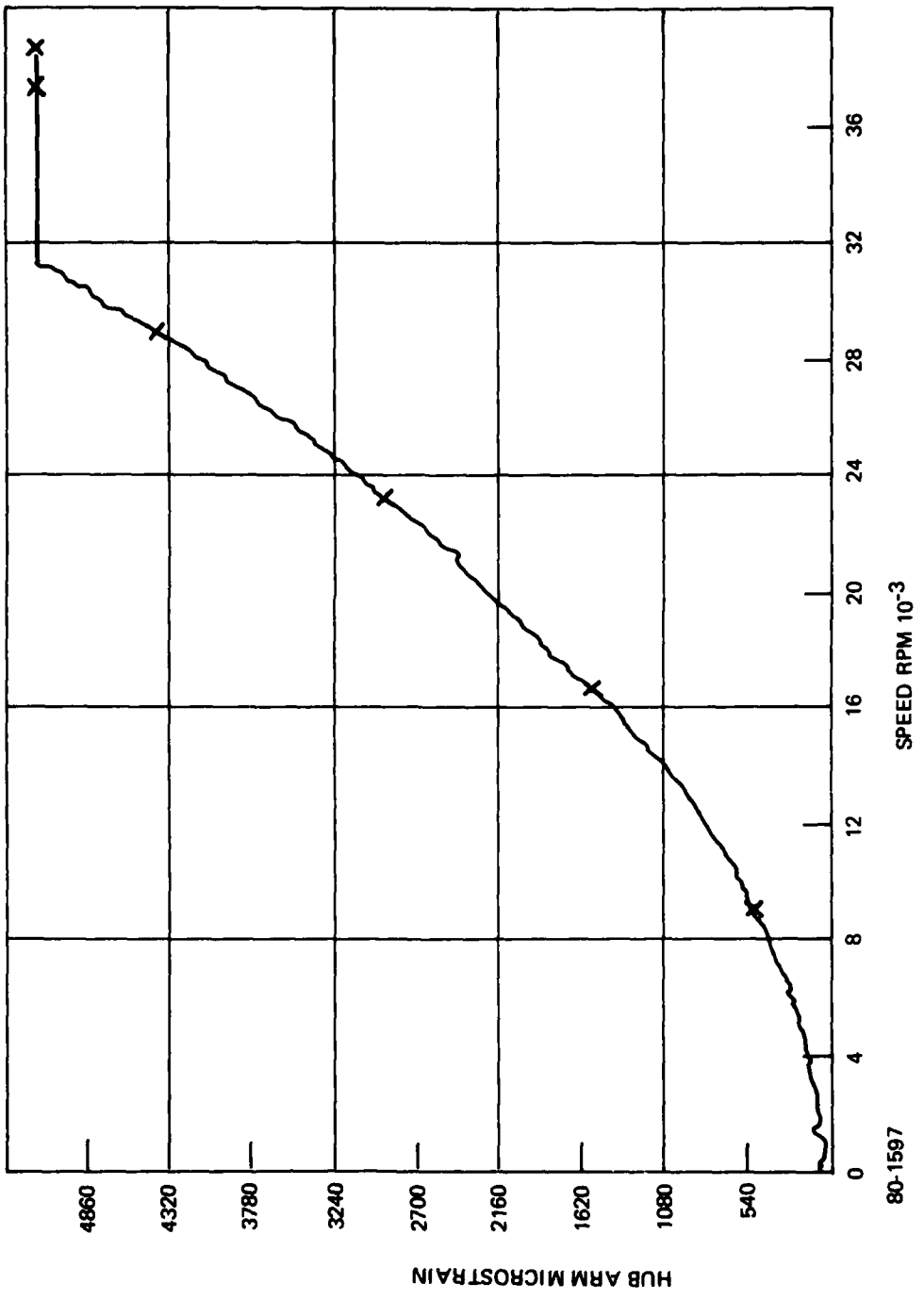

Figure A28 CHANNEL 12 STRAIN vs. SPEED, RUN 2

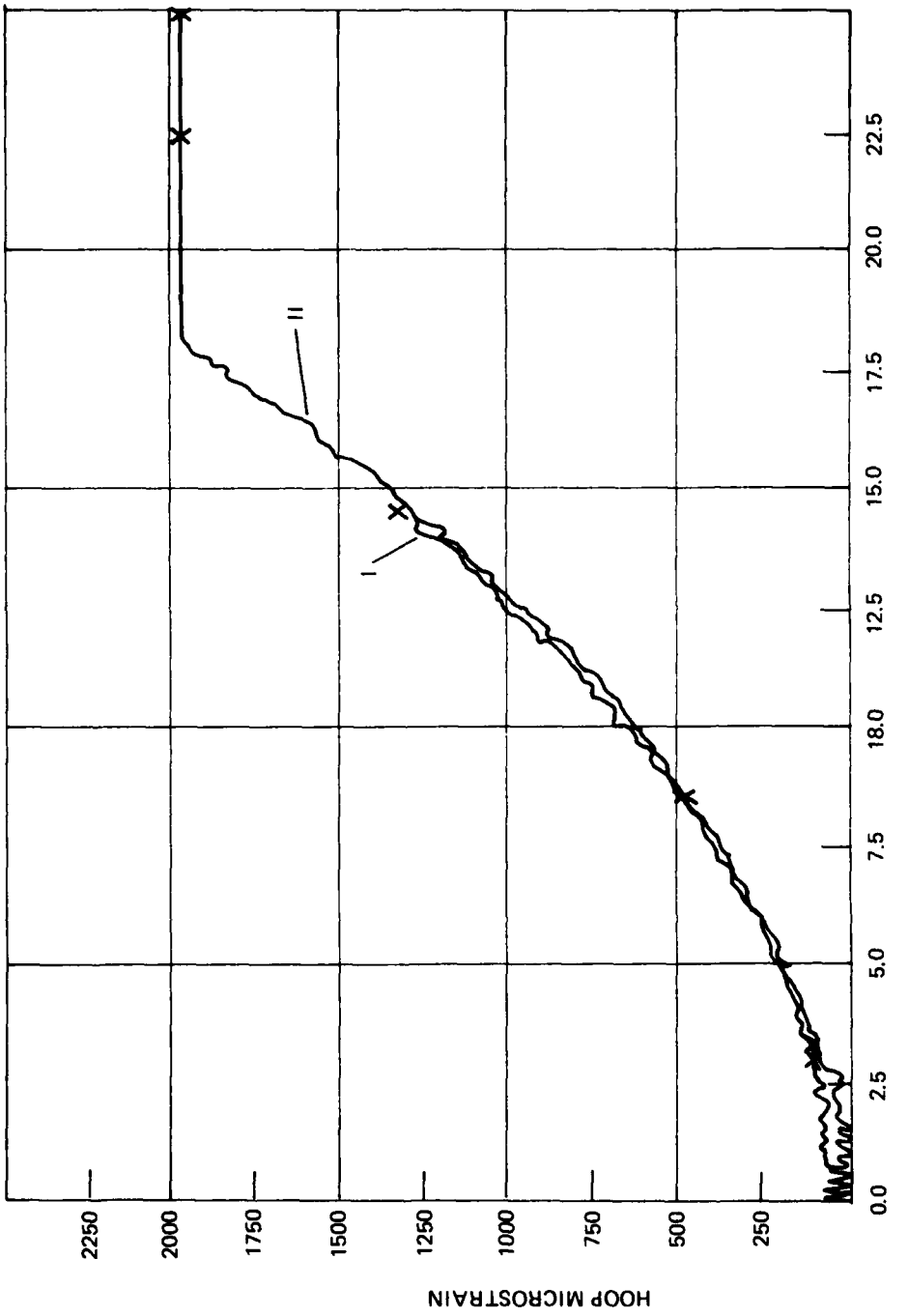

Figure A29 CHANNEL 1, RUN 1 AND RUN 2

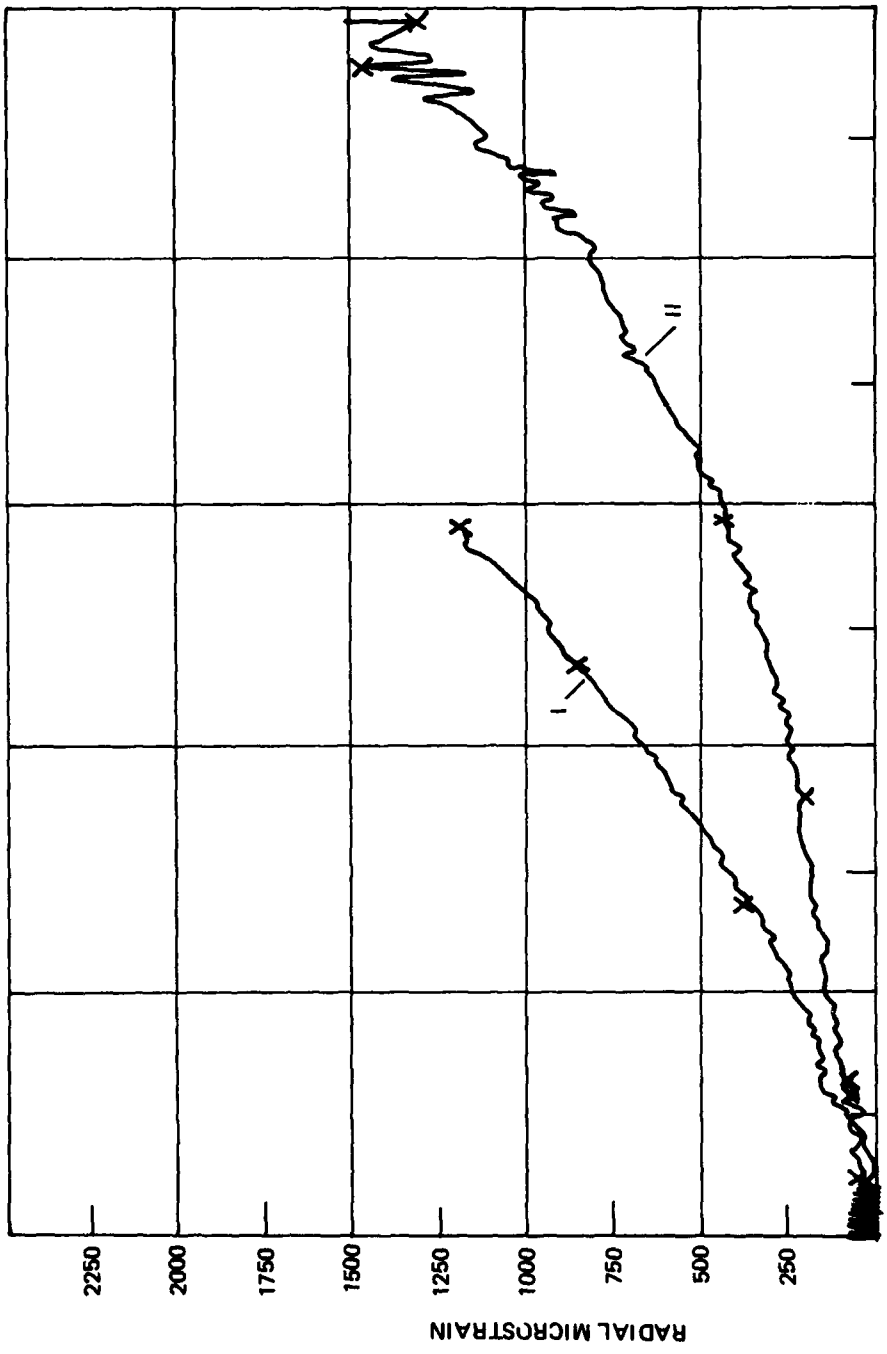

Figure A30 CHANNEL 2, RUN 1 AND RUN 2

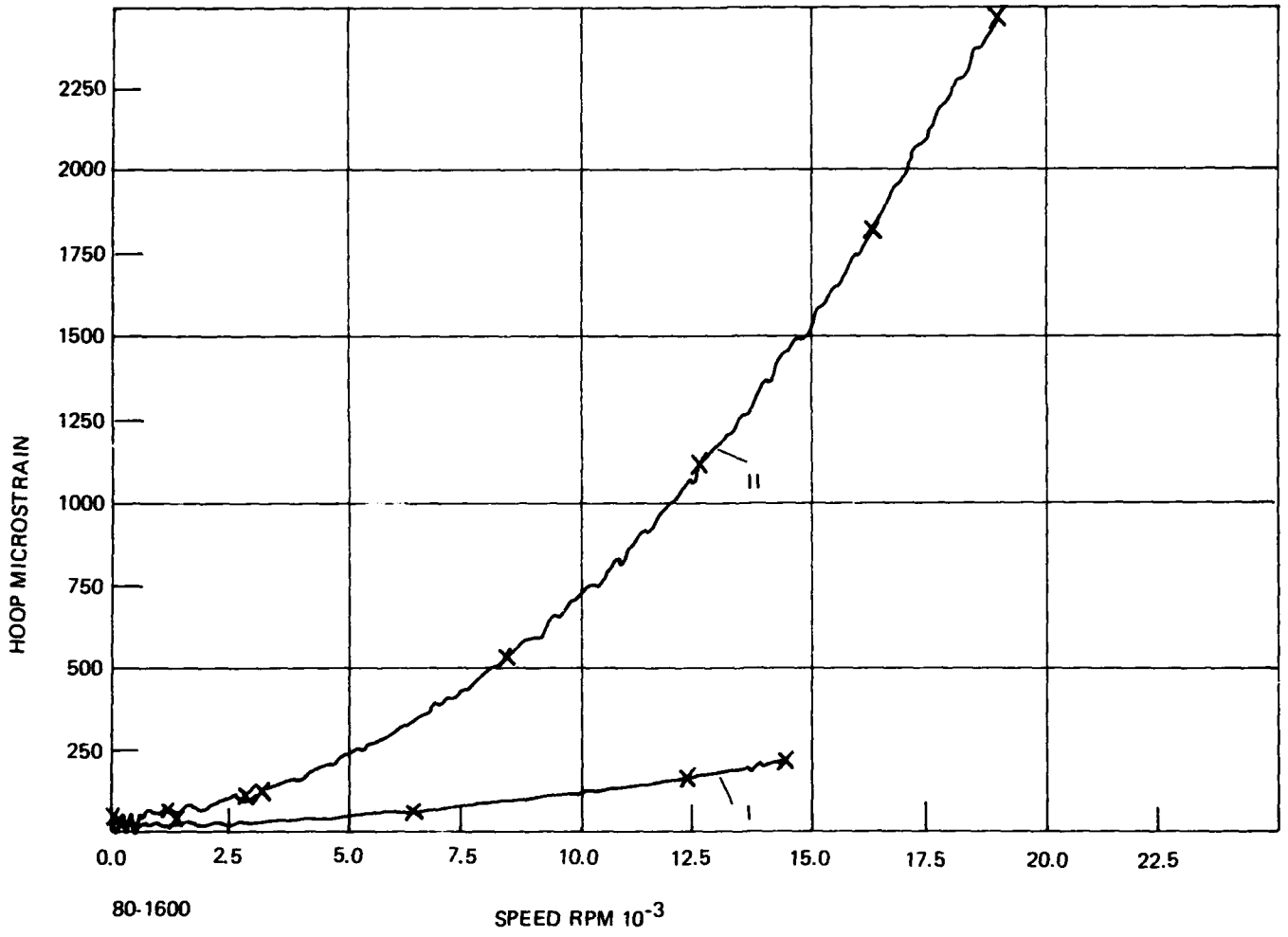

Figure A31 CHANNEL 3, RUN 1 AND RUN 2

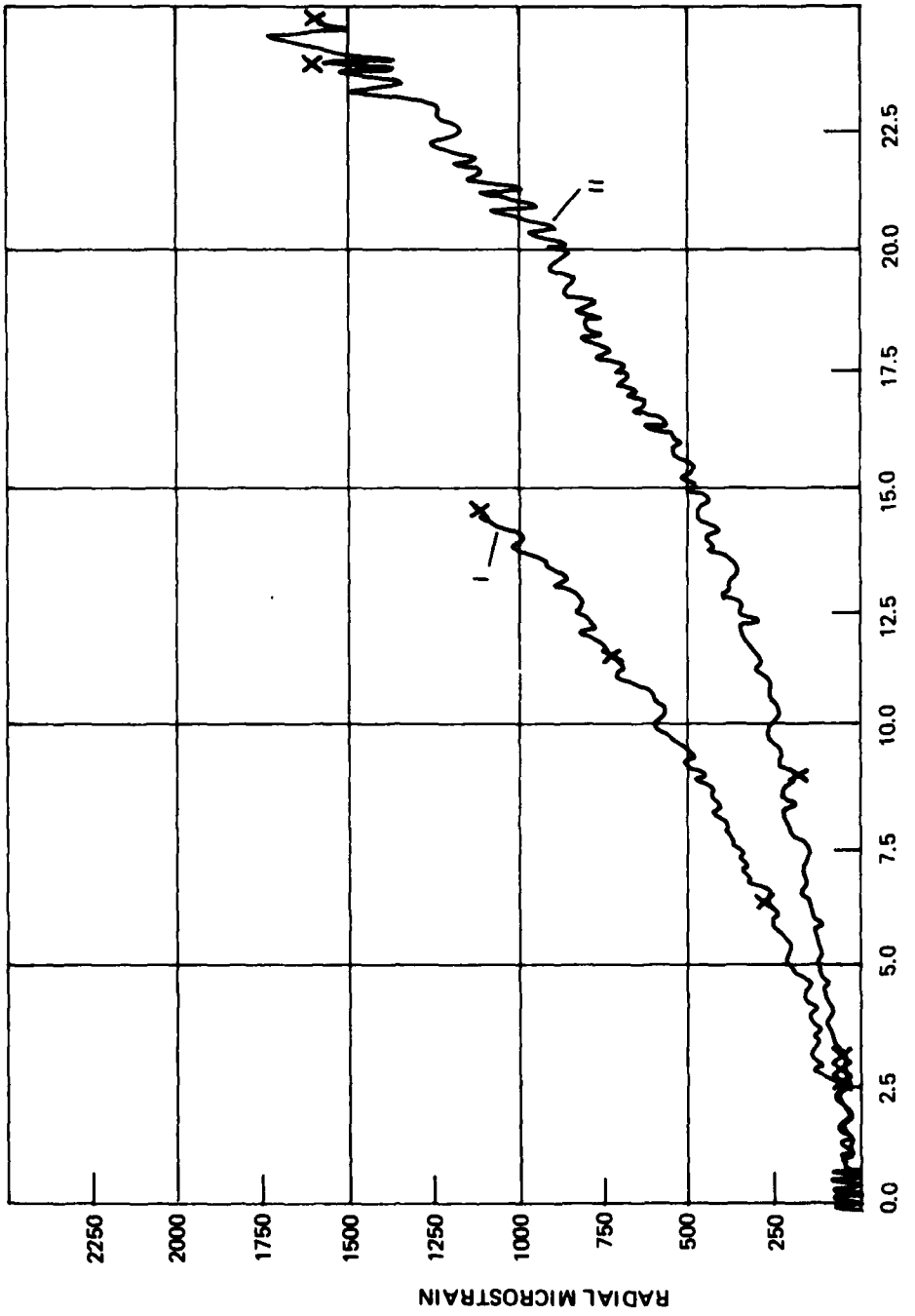

Figure A32 CHANNEL 4, RUN 1 AND RUN 2

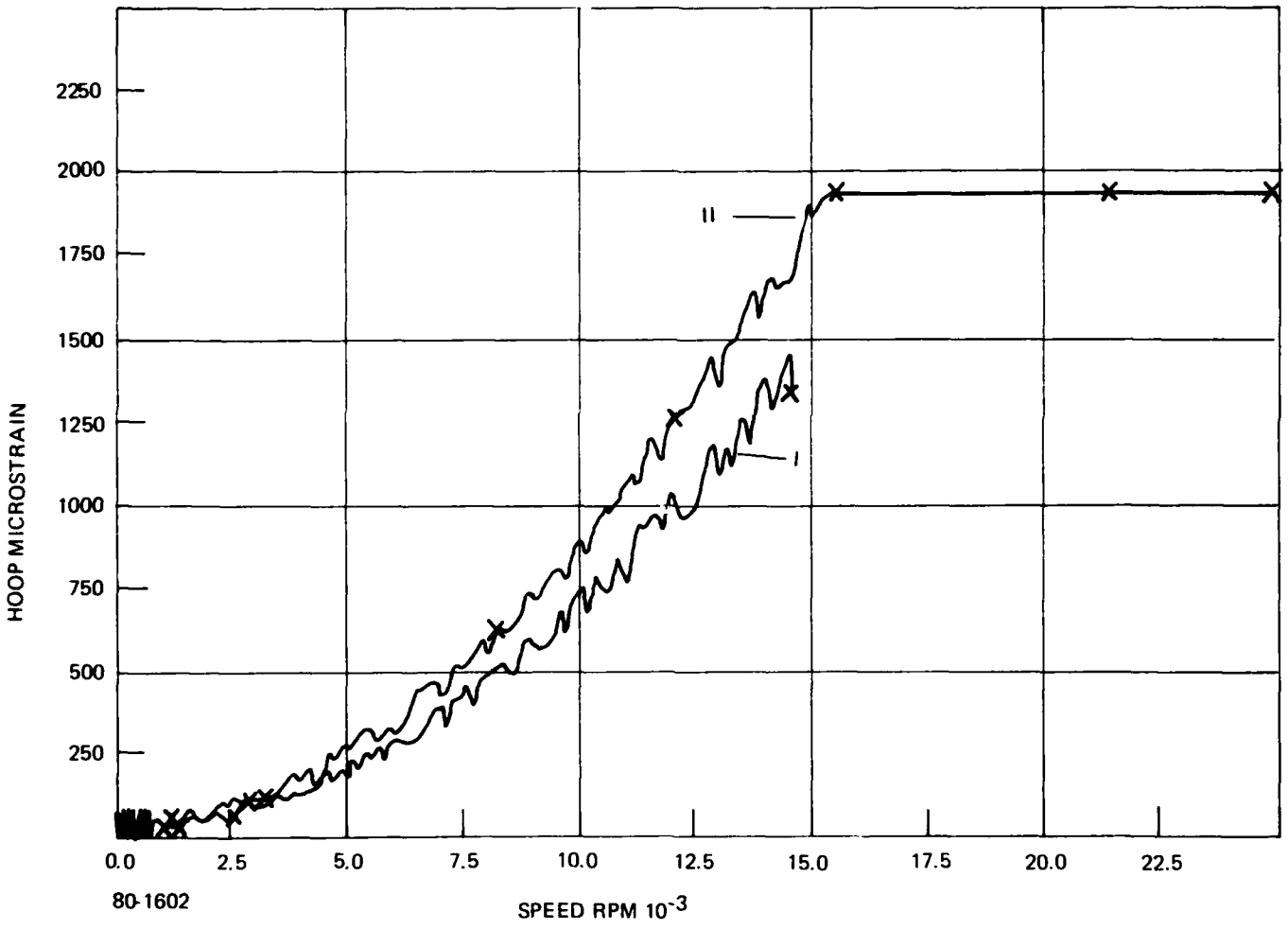

Figure A33 CHANNEL 5, RUN 1 AND RUN 2

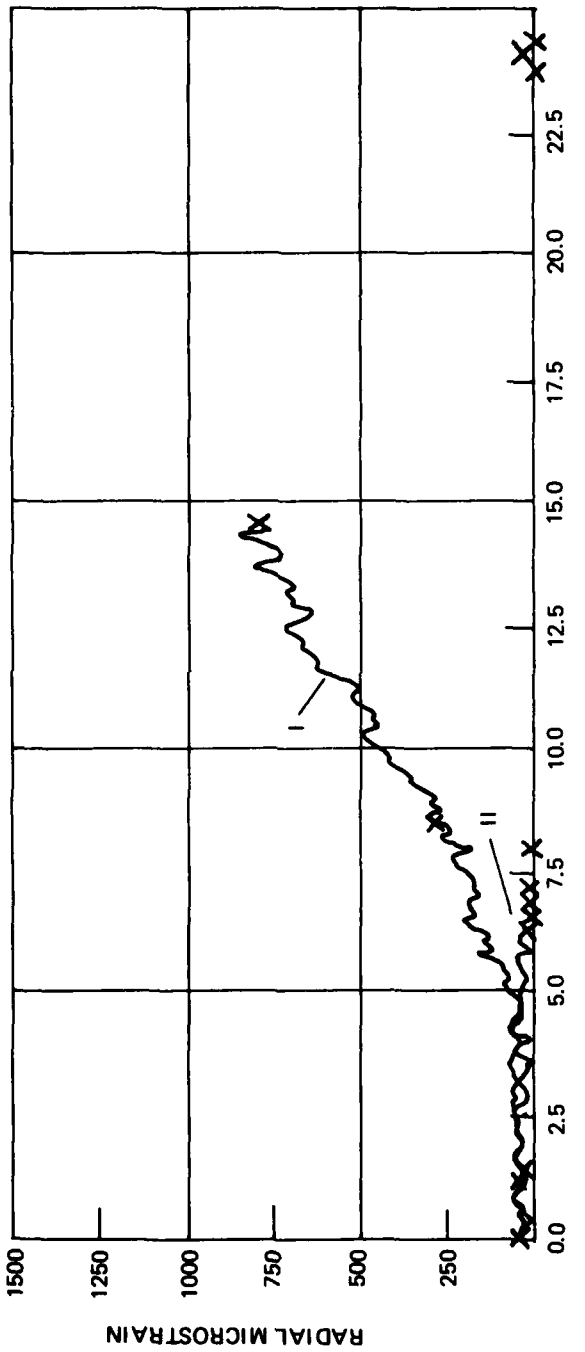

Figure A34 CHANNEL 6, RUN 1 AND RUN 2

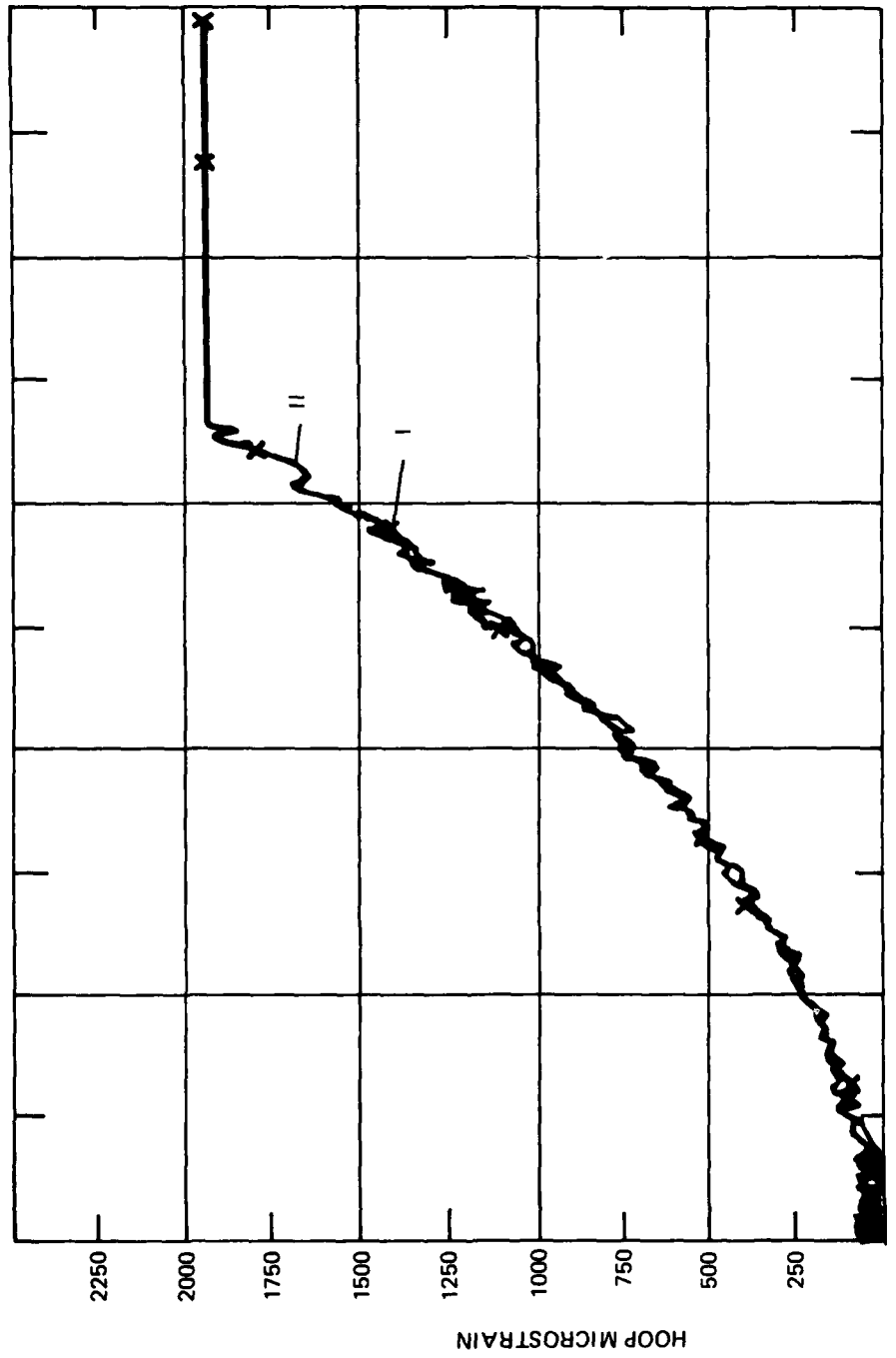

Figure A35 CHANNEL 7, RUN 1 AND RUN 2

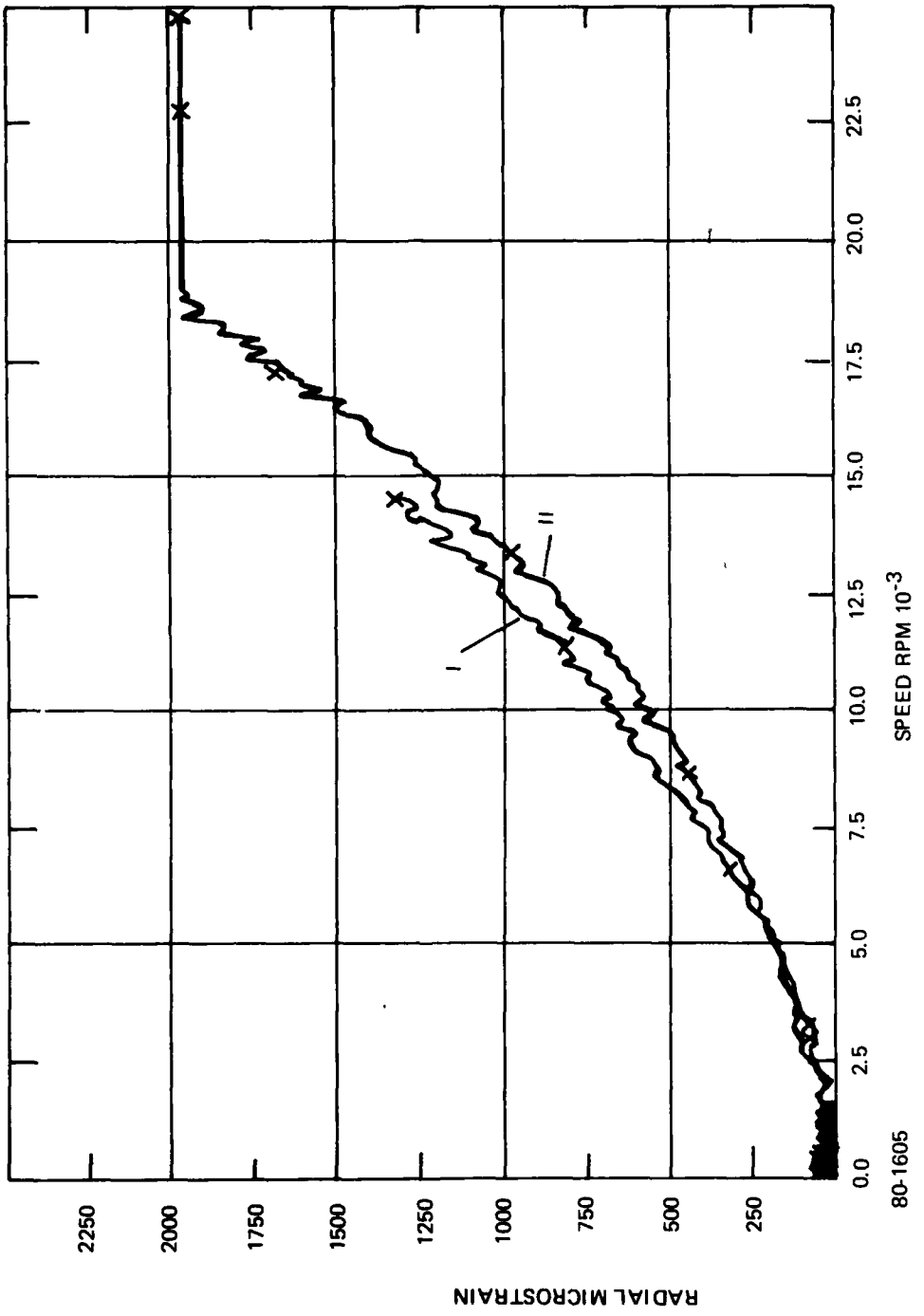

Figure A36 CHANNEL 8, RUN 1 AND RUN 2

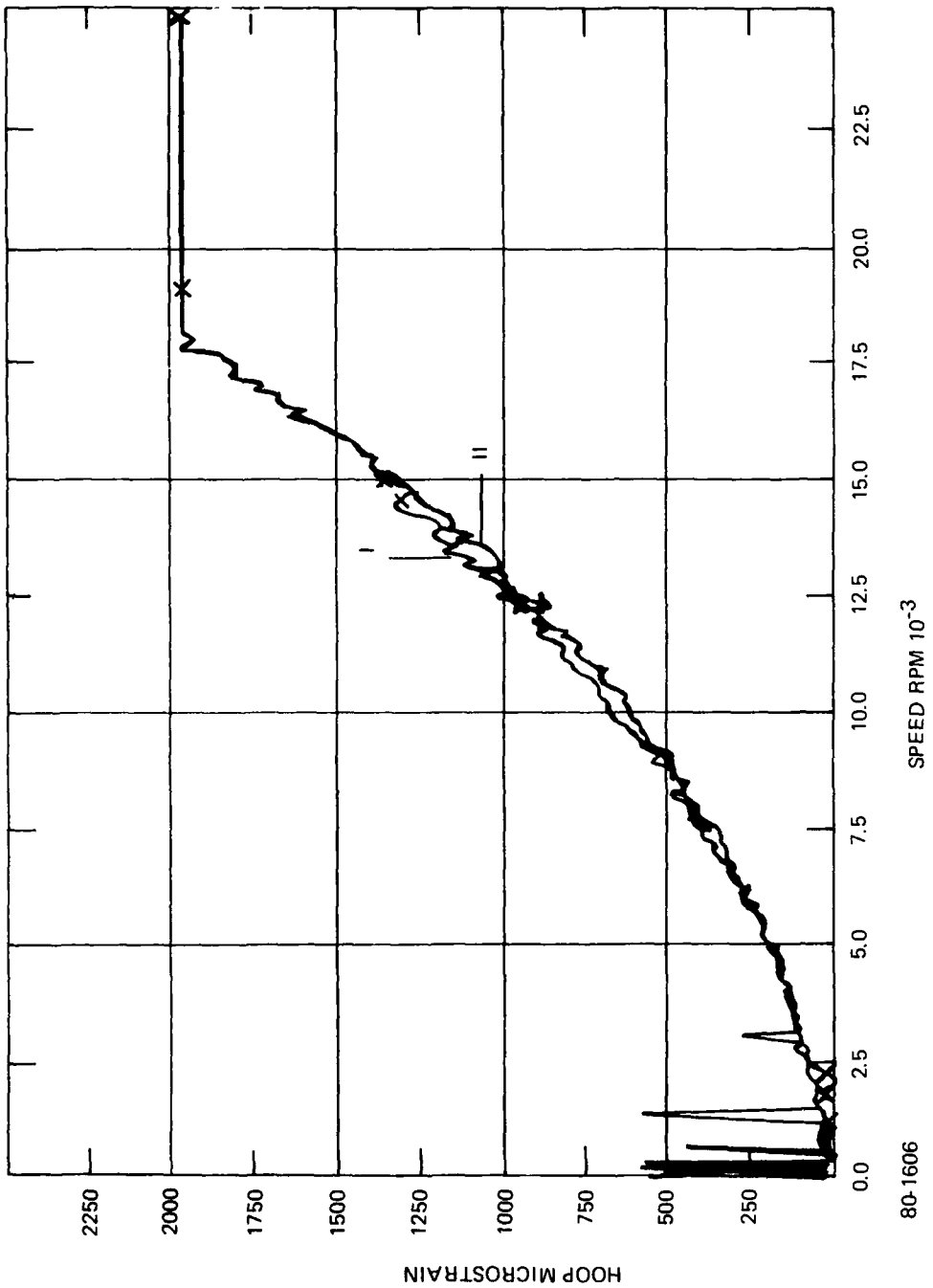

Figure A37 CHANNEL 9, RUN 1 AND RUN 2

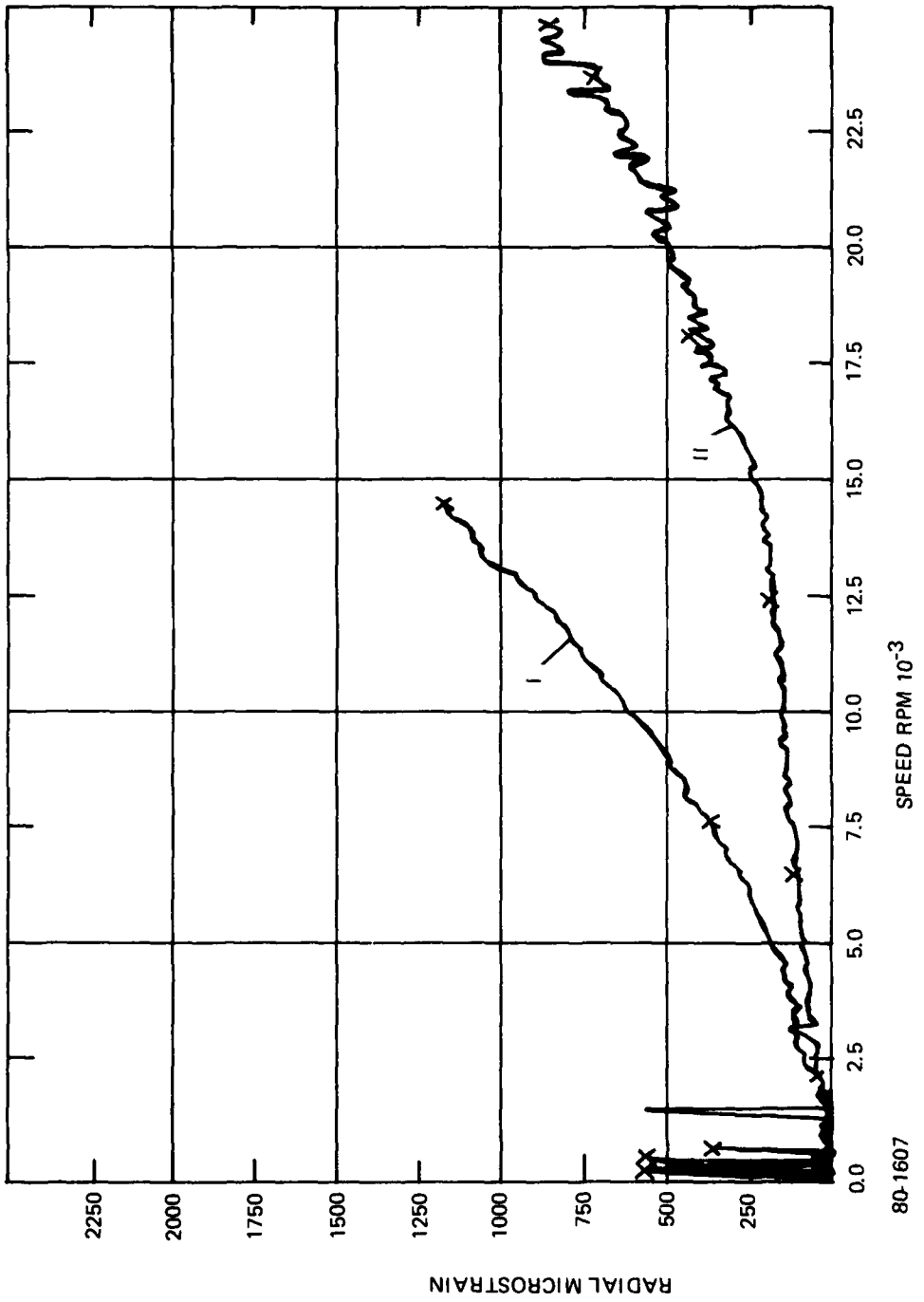

Figure A38 CHANNEL 10, RUN 1 AND RUN 2

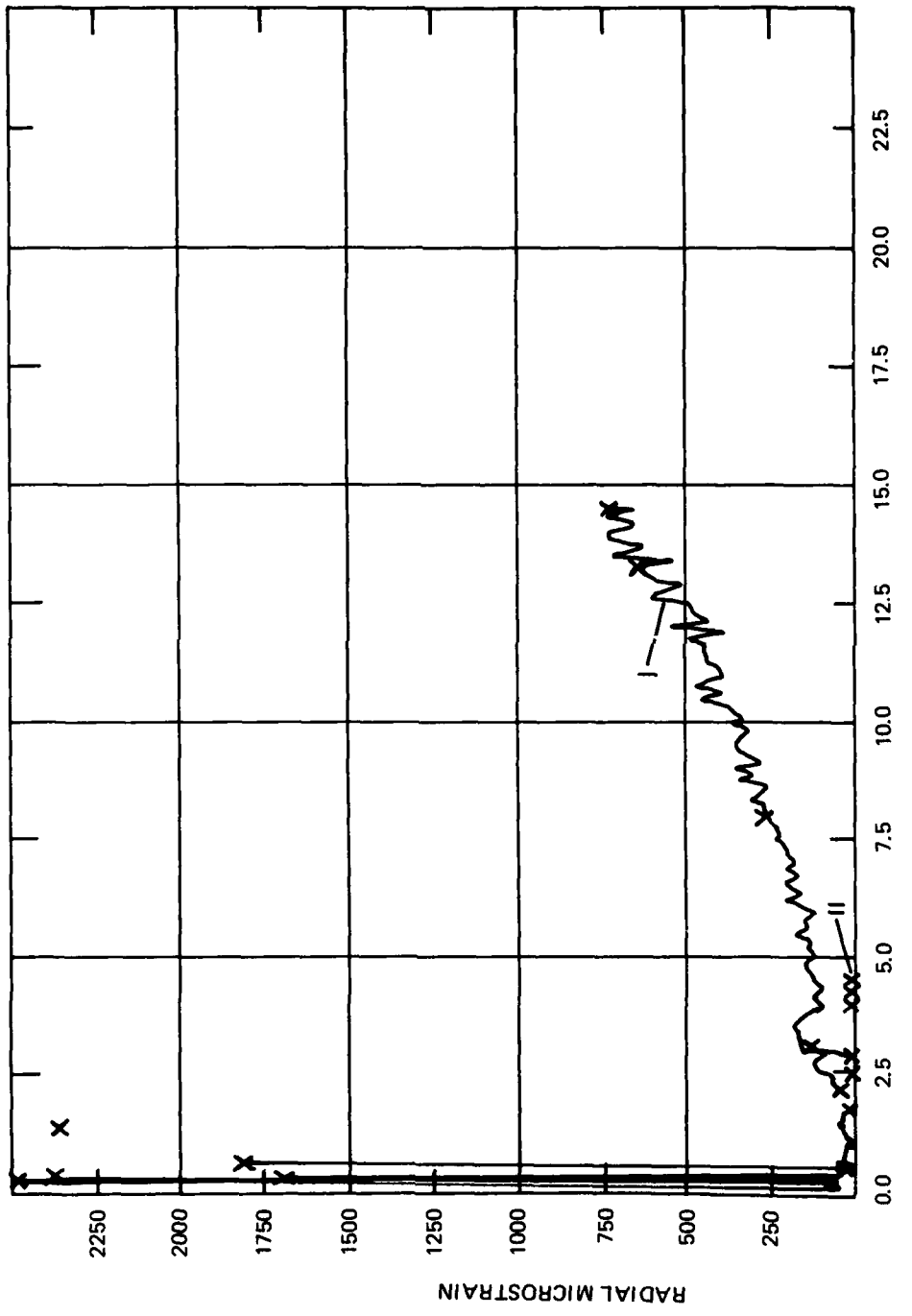

Figure A39 CHANNEL 11, RUN 1 AND RUN 2

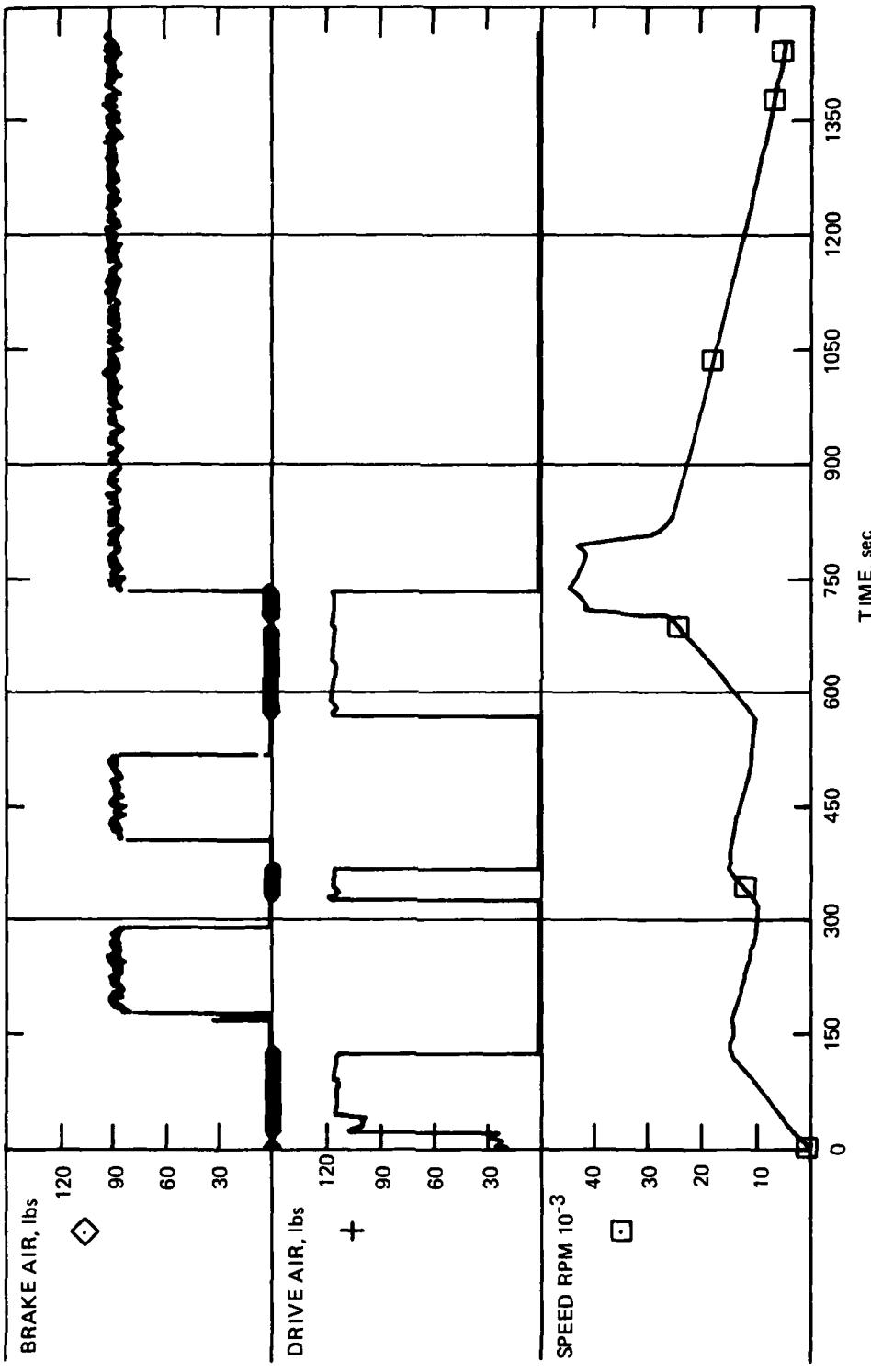

Figure A40 SPEED CYCLING, RUN 1

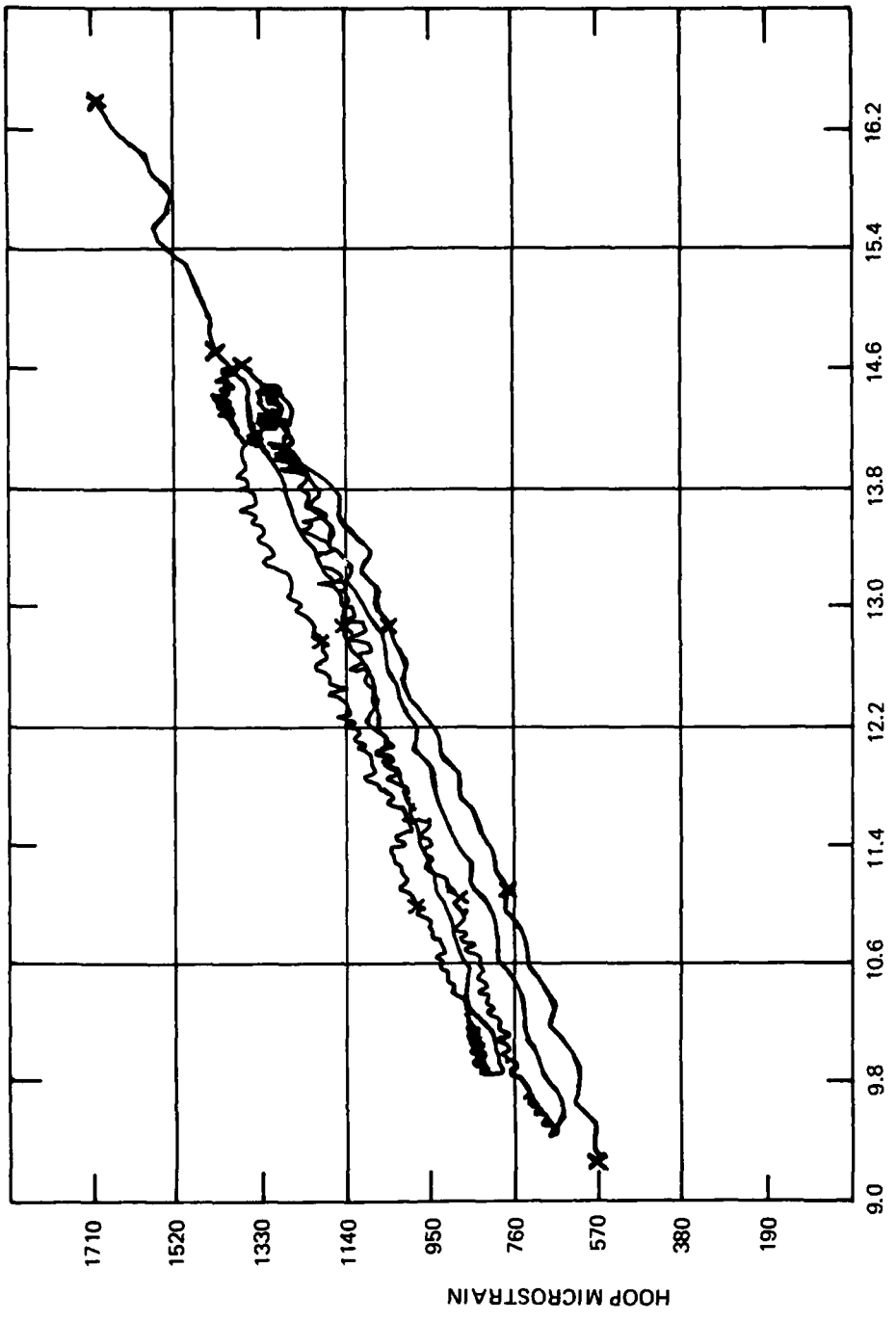

Figure A41 CHANNEL 1 STRAIN CYCLING, RUN 1

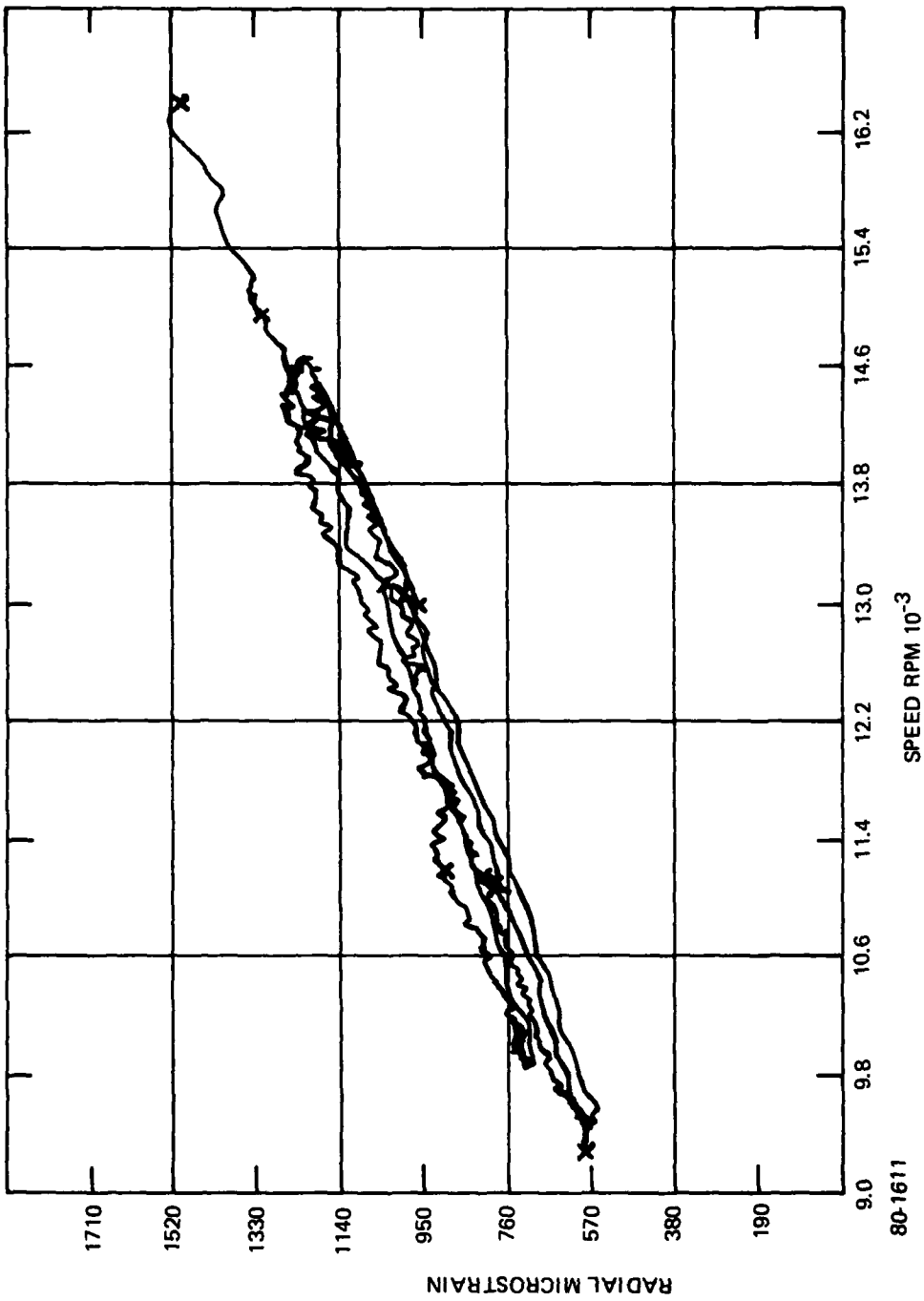

Figure A42 CHANNEL 2 STRAIN CYCLING, RUN 1

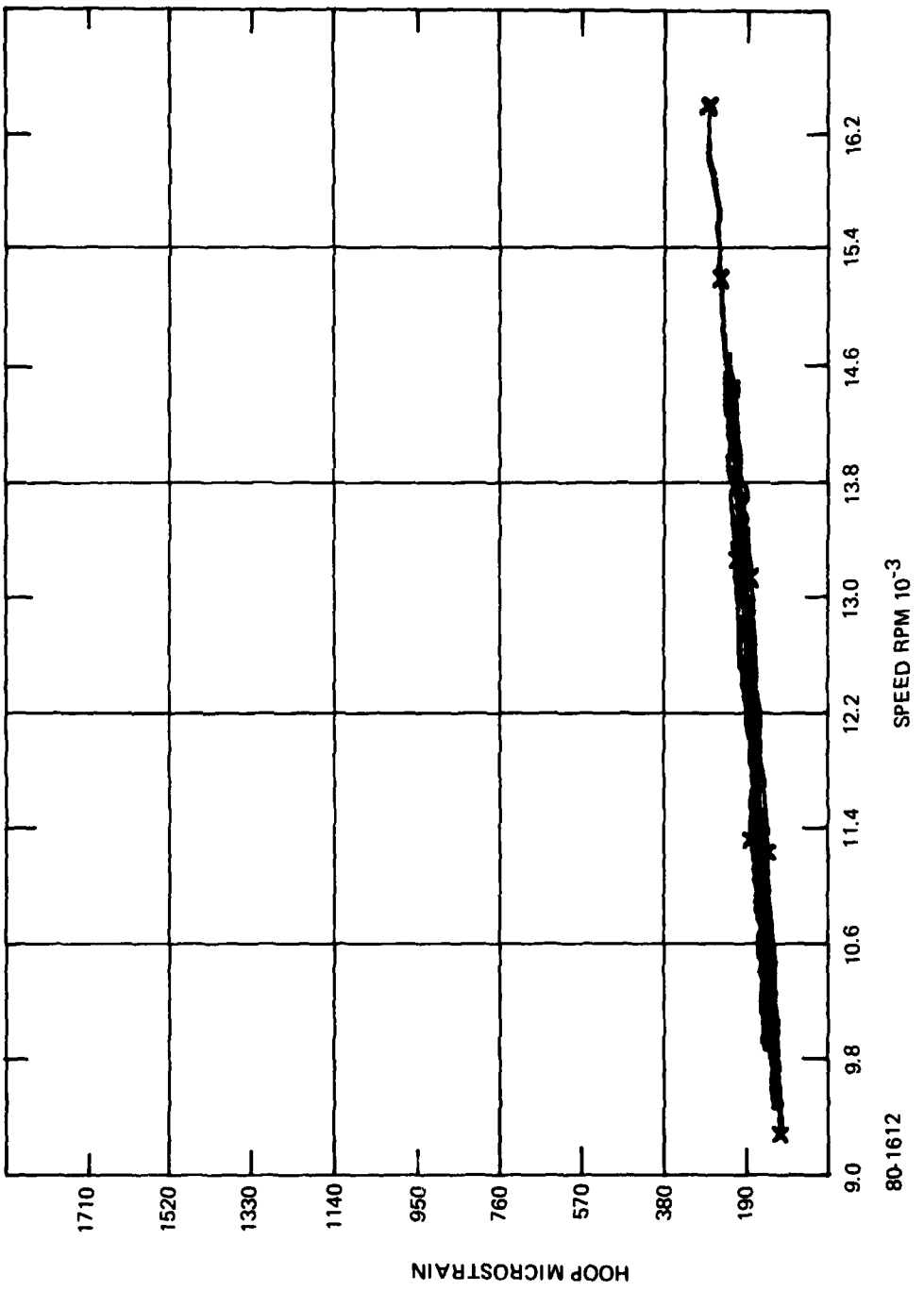

Figure A43 CHANNEL 3 STRAIN CYCLING, RUN 1

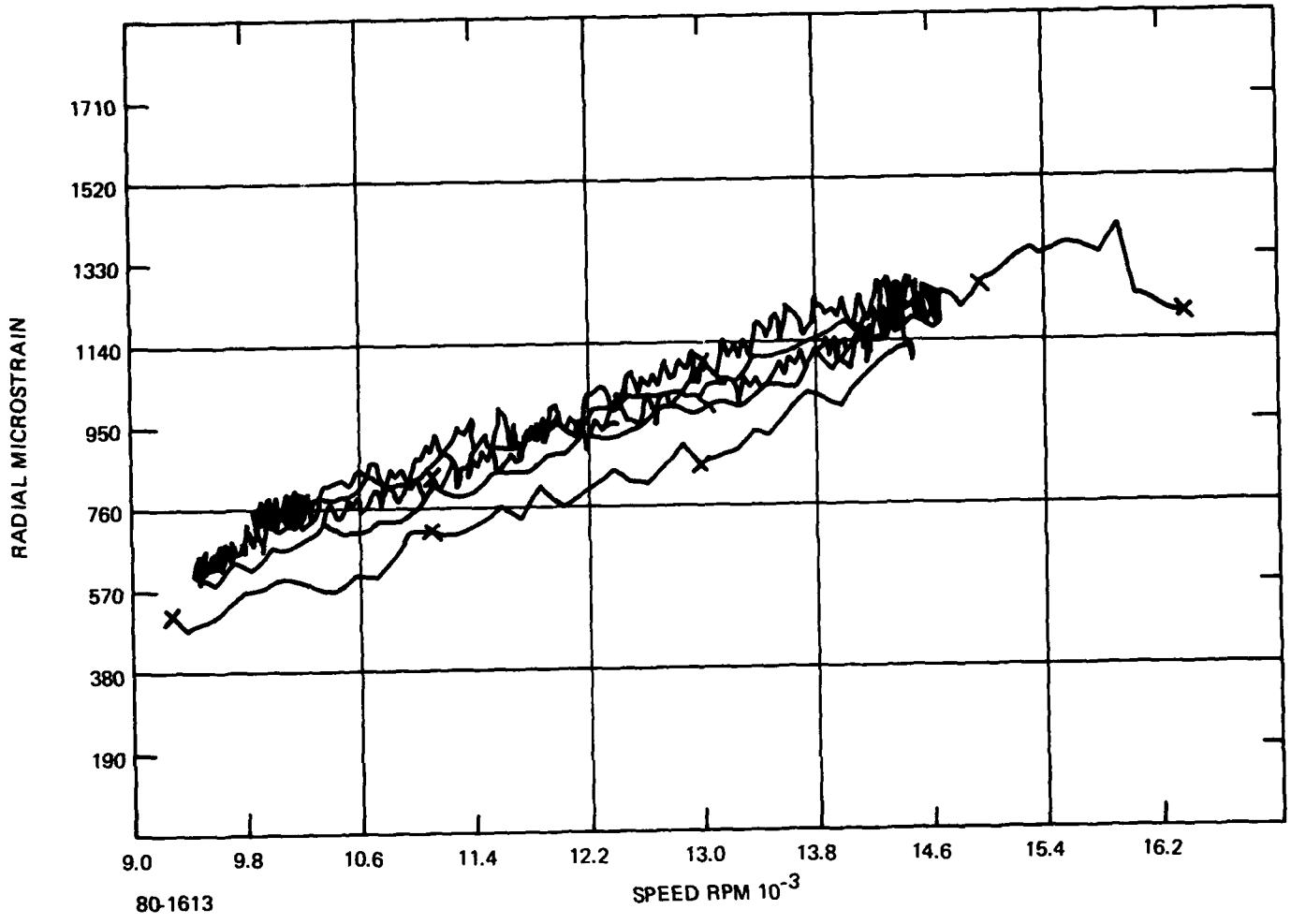

Figure A44 CHANNEL 4 STRAIN CYCLING, RUN 1

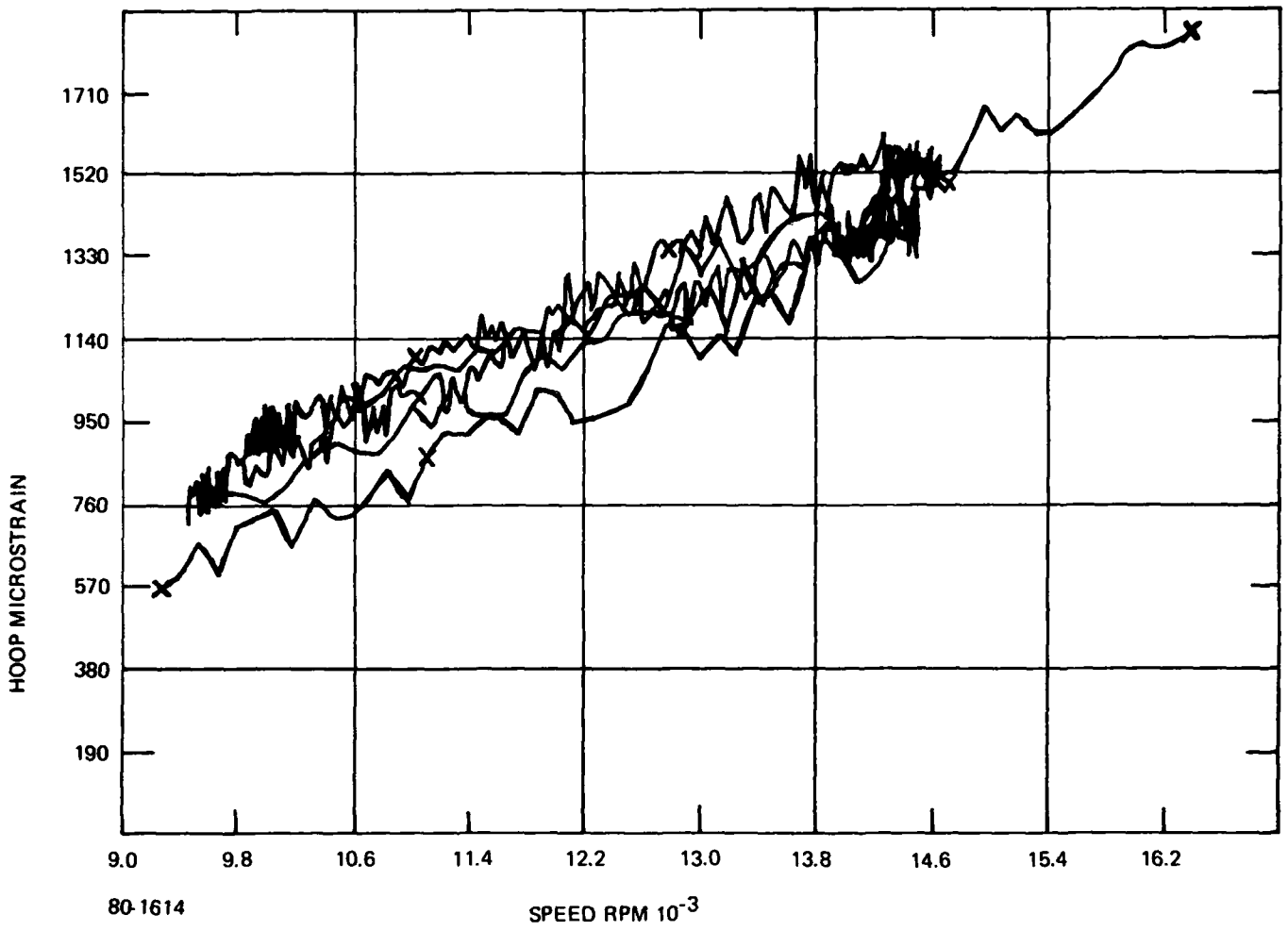

Figure A45 CHANNEL 5 STRAIN CYCLING, RUN 1

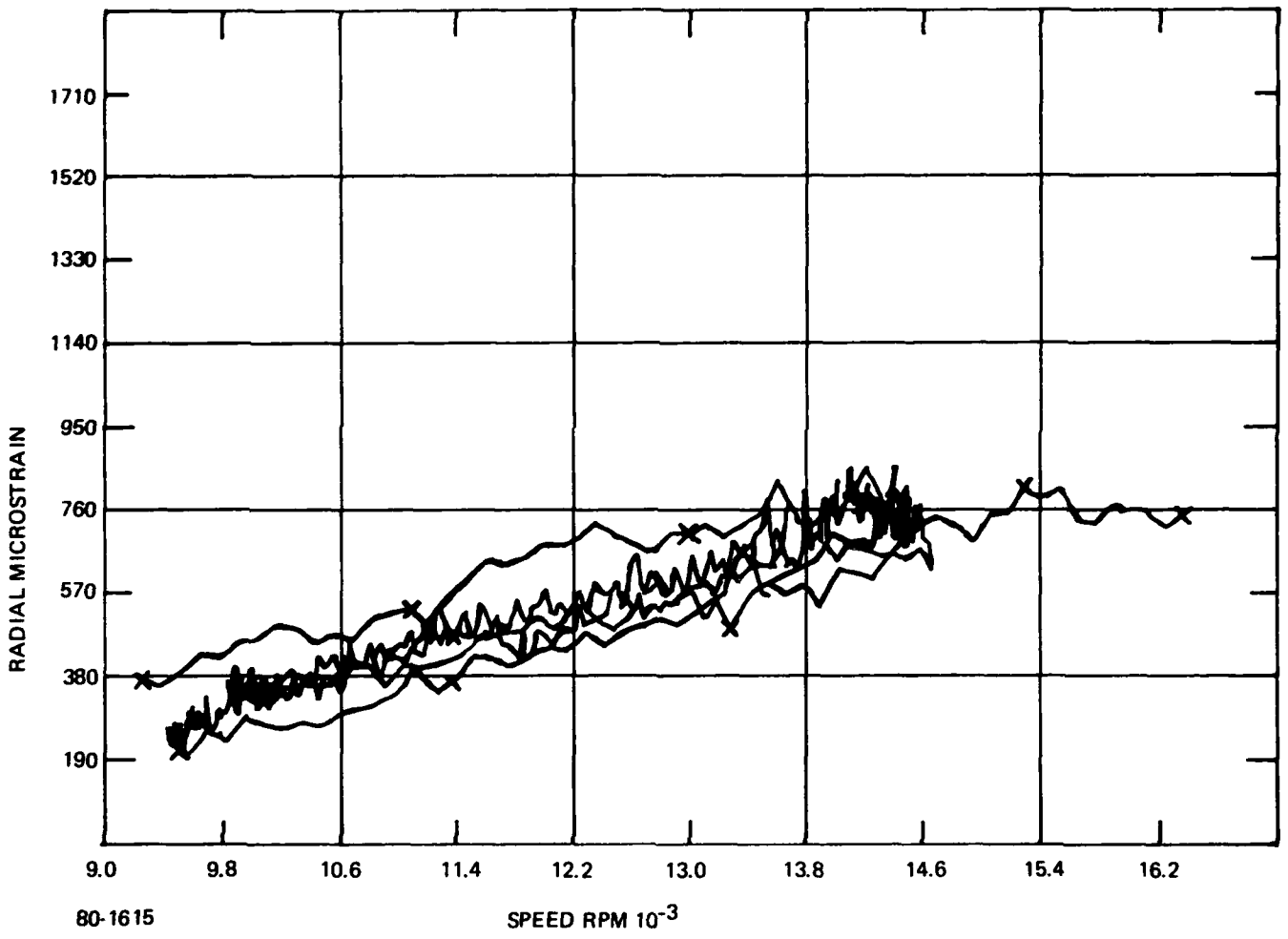

Figure A46 CHANNEL 6 STRAIN CYCLING, RUN 1

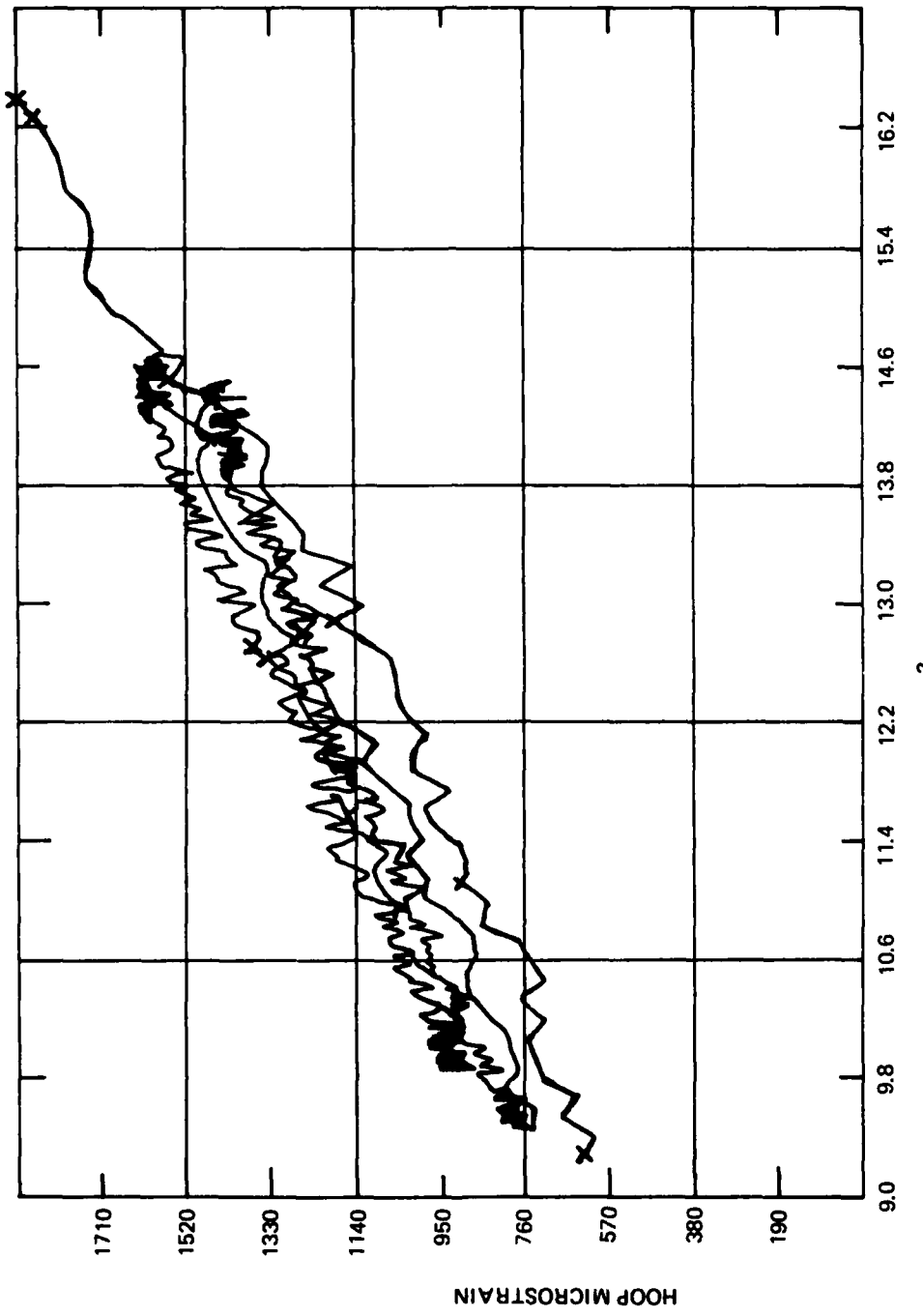

Figure A47 CHANNEL 7 STRAIN CYCLING, RUN 1

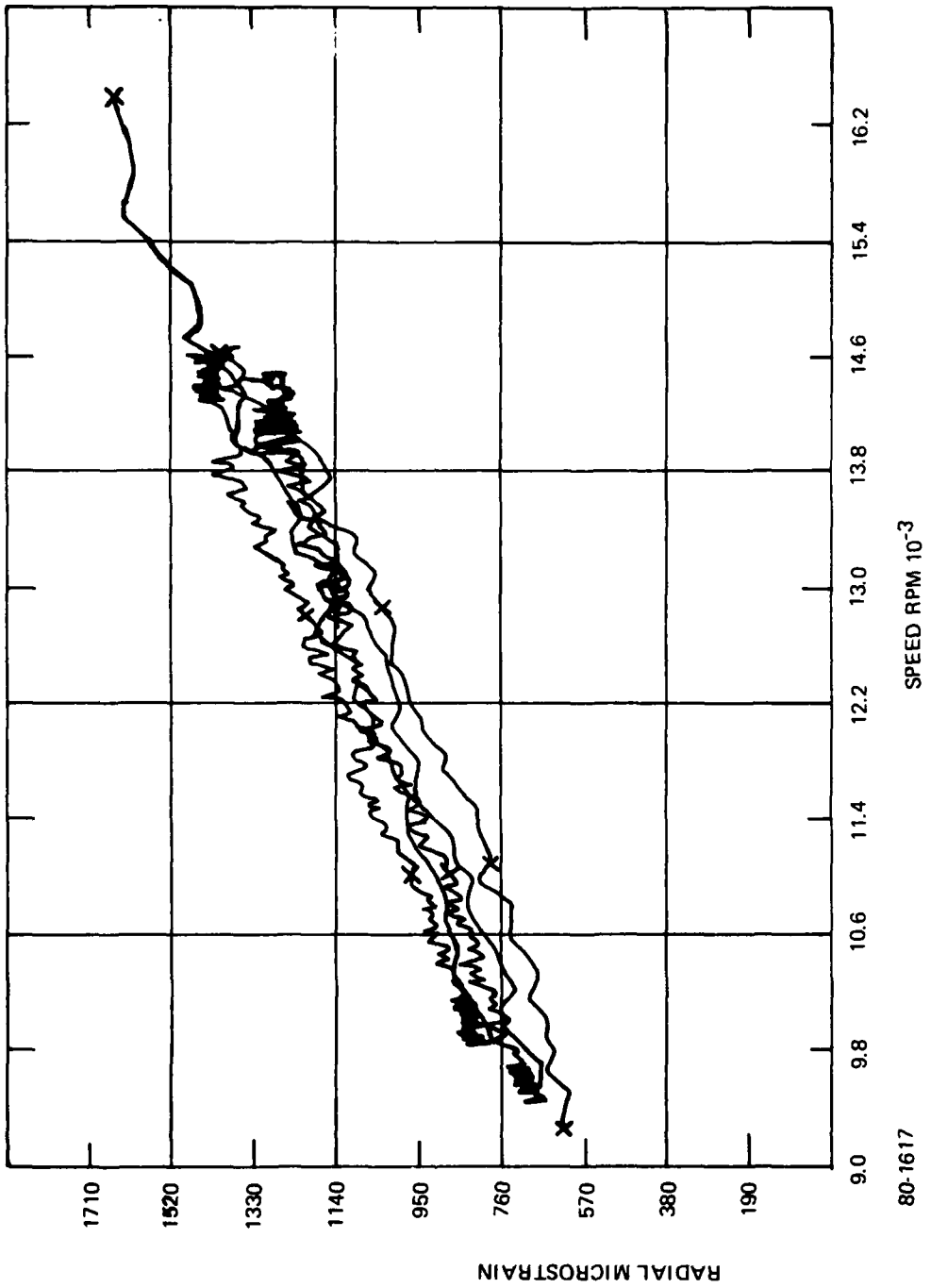

Figure A48 CHANNEL 8 STRAIN CYCLING, RUN 1

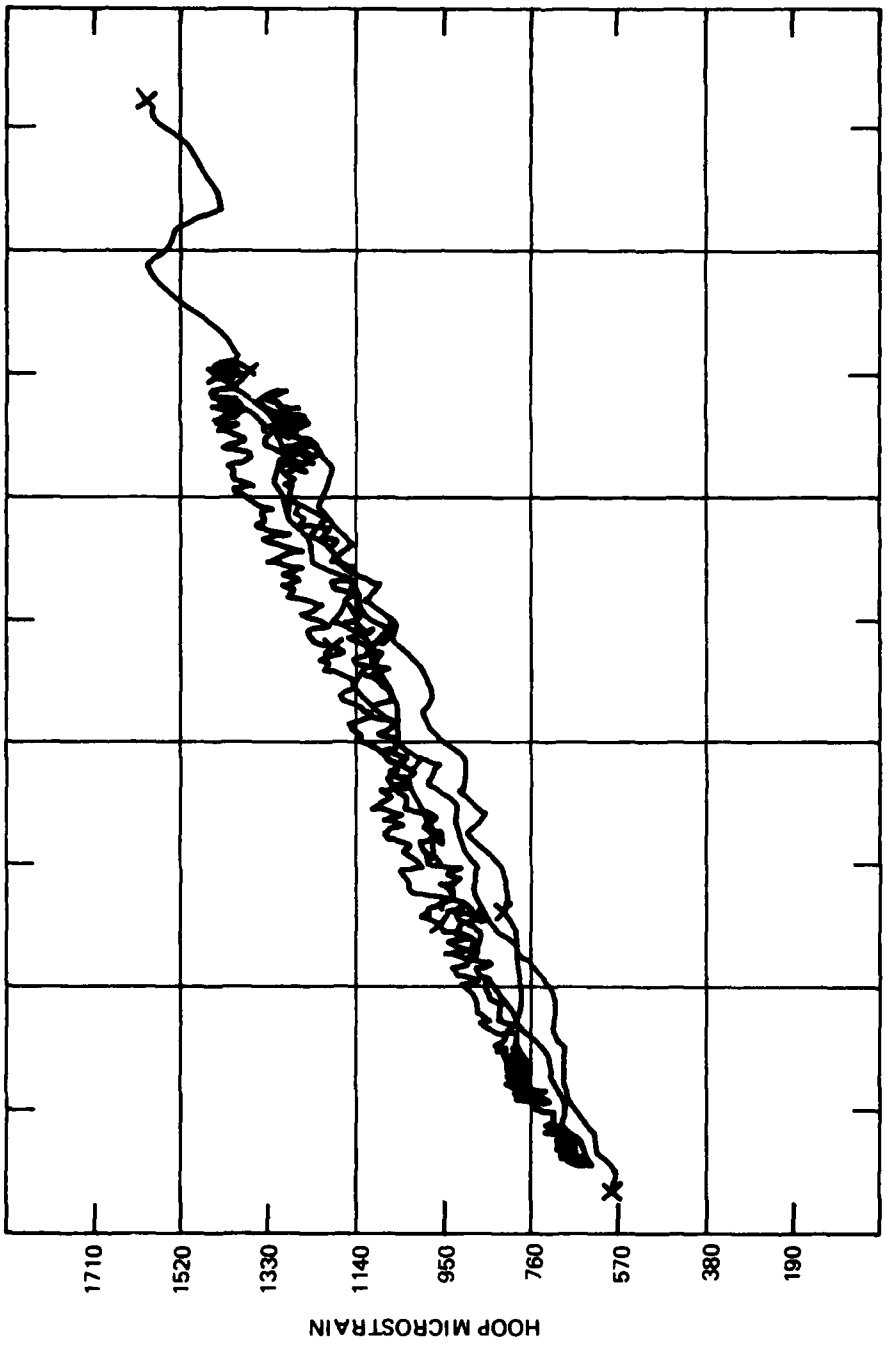

Figure A49 CHANNEL 9 STRAIN CYCLING, RUN 1

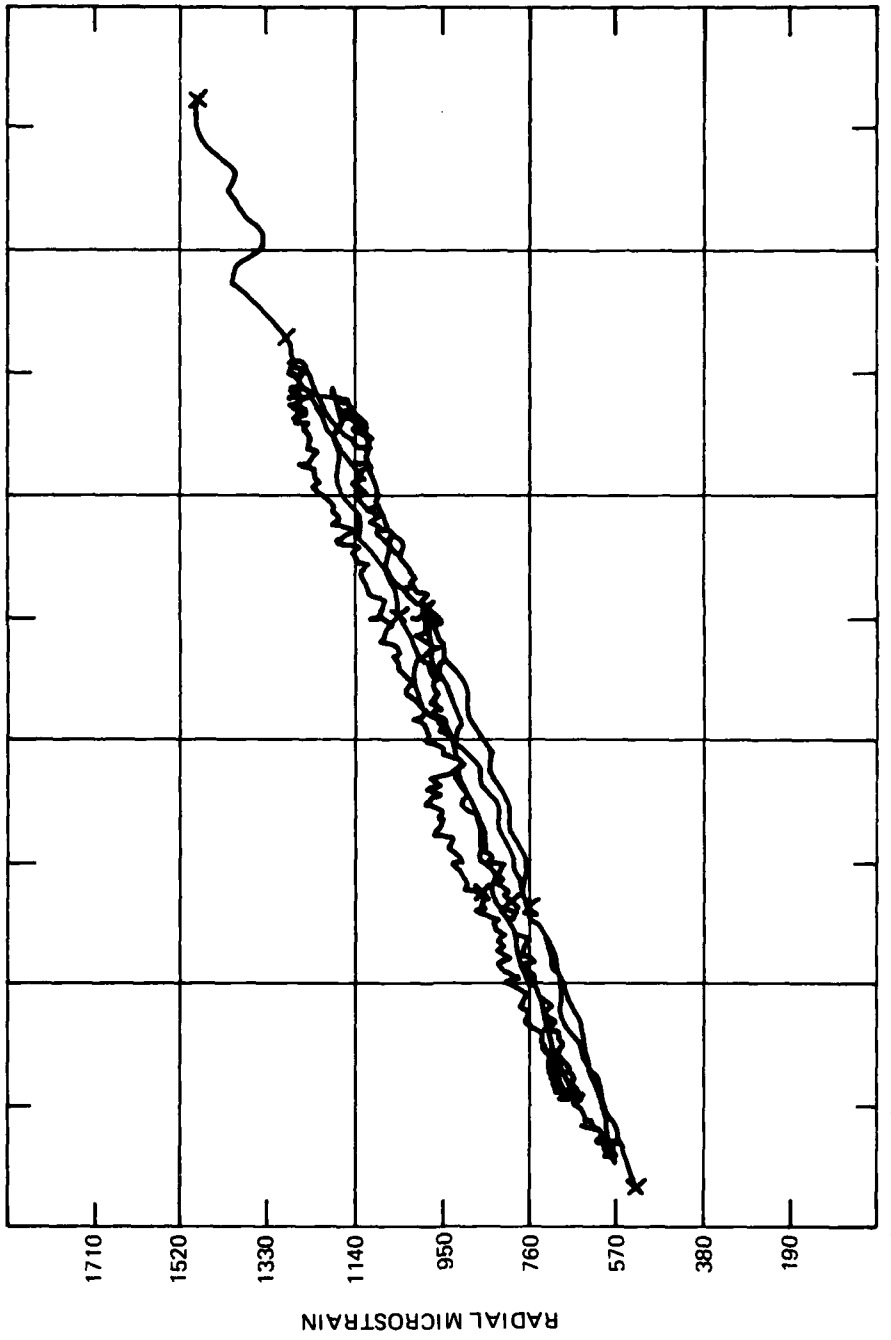

Figure A50 CHANNEL 10 STRAIN CYCLING, RUN 1

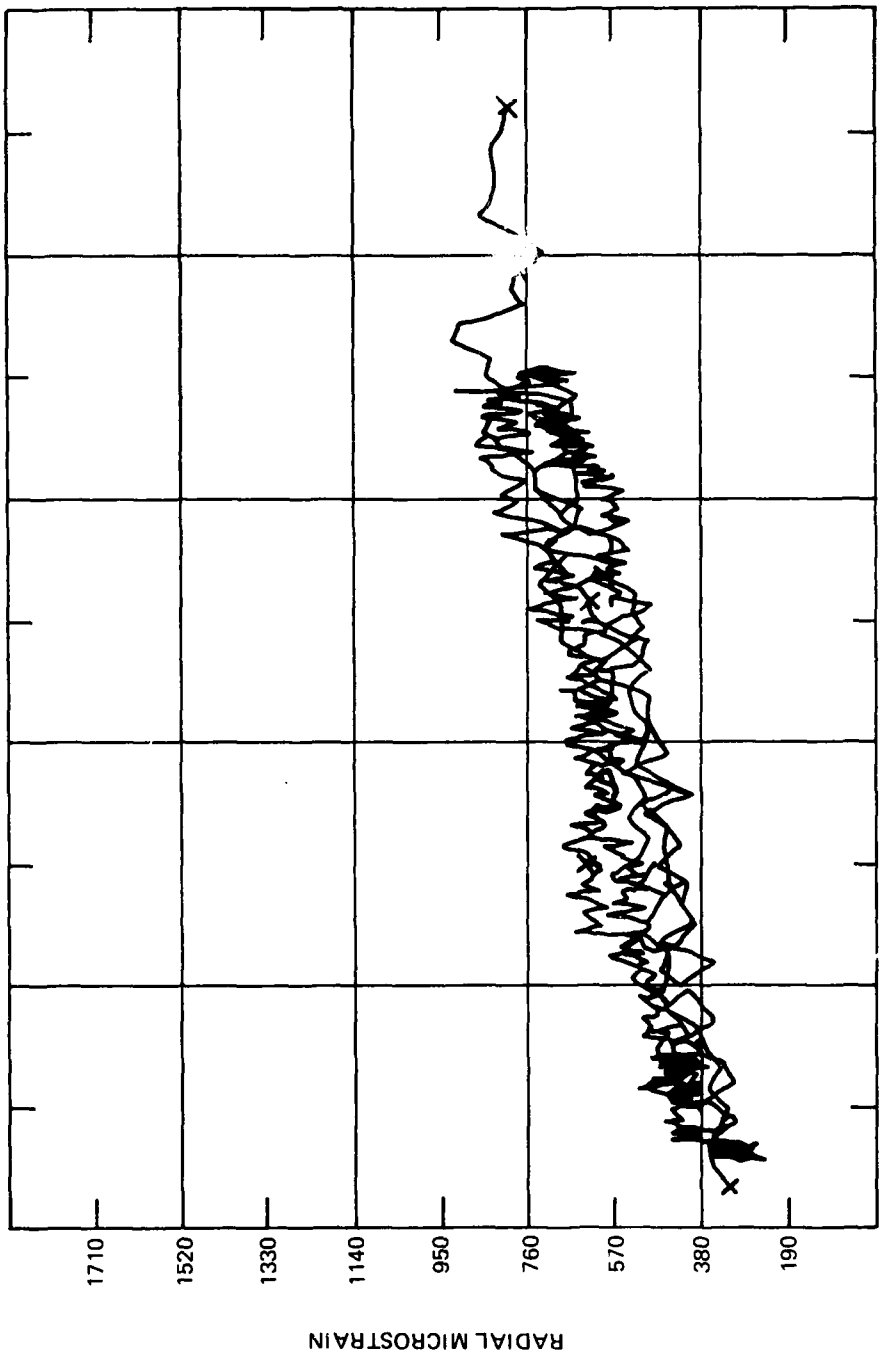

Figure A51 CHANNEL 11 STRAIN CYCLING, RUN 1

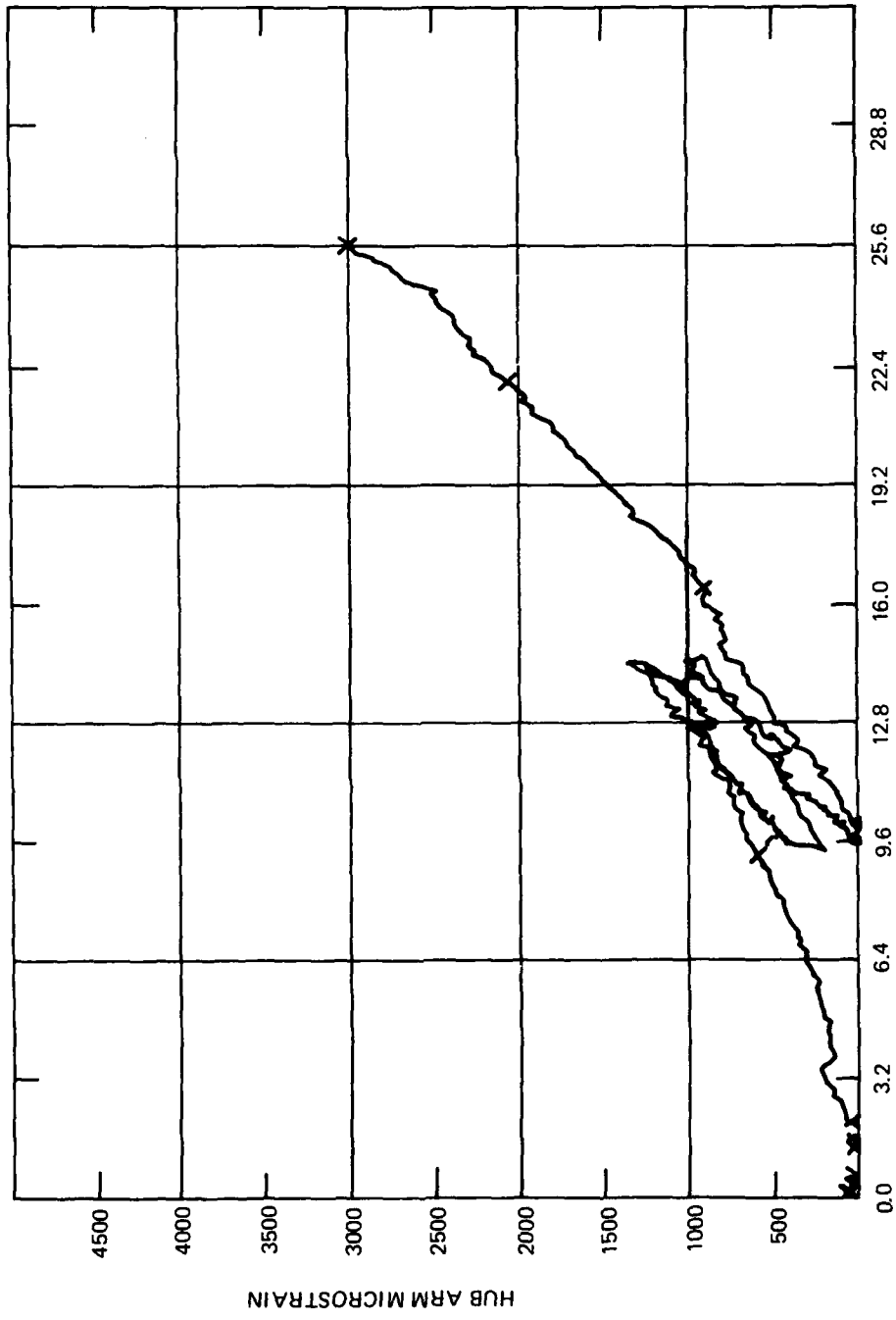

Figure A52 CHANNEL 12 STRAIN CYCLING, RUN 1

APPENDIX B

DUREL/ARDEL POLYARYLATE DATA

APPENDIX B DUREL/ARDEL POLYARYLATE DATA

POLYARYLATES AND AVCO FATIGUE DATA

Polyarylates are a new class of engineering thermoplastics based chemically on Biphenal A and phthalic acids. These materials are amorphous with high heat resistance (heat deflection temperature ~350°F) and superior mechanical toughness. While the tensile strength and modulus are typical of high performance thermoplastics, the fatigue resistance and creep resistance are outstanding. Furthermore, the retention of these properties over a much wider temperature range (-40°F to 250°F) than does polycarbonate makes them nearly unique. The polyarylates also exhibit outstanding elastic recovery characteristics from flexural, tensile and compressive deformations. The deformation at yield is 7% and very little mechanical loss is exhibited under cyclic loading below the yield point. The endurance limit in flexural fatigue varies from 2400 psi at 10^7 cycles to better than 4000 psi at 10^4 cycles.

Other characteristics are excellent retention of strength and impact resistance after exposure to UV or high temperature (300°F) soak. The abrasion resistance is very good but not outstanding. The flammability of polyarylates is V-0 according to UL 94 test procedure.

The polyarylates are suitable for injection molding and extrusion although high, well controlled temperatures are required. The resin needs to be heated to the temperature region of 675-735° for proper molding. It is an efficient molding material since up to 25% regrind can be used for most applications with little change in properties. Polyarylates are marketed by Hooker Chemical (Durel) and by Union Carbide (Ardel). The specific chemical differences between these two are not known.

Two tensile fatigue tests were performed on Durel 400 tensile bars in accordance with ASTM procedure D638. Type I specimens were used. The test area dimensions were 0.123 x 0.500 inch. One test was run for 2000 cycles and the other for 10,000 cycles. Both tests were run by adjusting the load to obtain the desired strain excursions.

The 10,000 cycle fatigue test specimen was to cycle between 0.2 - 0.5% on the low end and 1.4 - 1.5% strain on the high end at a rate of 30 cycles per minute. The specimen contained a 0.025-inch diameter hole in the center to determine the effect of stress concentration as discussed in the stress analysis. The sample was set up in the MTS load frame which is an electrohydraulic loading system capable of stepless cycling rates from 1 cycle per 1000 seconds, to 1000 cycles per second.

The load vs. time was recorded on an Instron loading system recorder. Strain vs. time was recorded on a BBN, X-Y plotter. A Daytronic model 300 D-93 strain gage signal conditioner module was used as a strain gage readout. The specimen strain was detected by means of an Avco strain gage extensometer which averages the output of strain gage on both sides of a flexure beam.

The specimen was installed in self tightening "Vee" grips. Strips of fine gut emory cloth were inserted between the separated grips and the sample to eliminate gouges in the specimen due to clamping forces. The extensometer was installed such that the 0.025-inch diameter hole was centered in the 2 inch gage length. The lower limit of load was set at 25 lbs to obtain a 0.2% strain. Cycling was started and the upper load limit was gradually increased until a 1.45% strain excursion was reached in the gage section. Hysteresis effects (lack of strain recovery) due to the rapid cycling rate caused the strain limits to drift upward during the first 100 cycles until the lower limit stabilized at 0.95% and the upper limit at 2.4% from the initial zero settings. Thus, the desired strain excursion was maintained but the limits (0.5 and 1.5%) were exceeded. This type of hysteresis is common for plastic materials under rapid cycling. Periodic minor control adjustments were required throughout the test to maintain the desired strain excursions.

After completion of the 10,000 cycle fatigue test, the test specimen was removed from the grips and allowed to recover for five minutes, after which the gage length was determined (with a scale) to have returned to its 2-inch dimension. Subsequent tests indicate this recovery time is less than 30 seconds. The grip area of the specimen showed some scratch marks indicating grip slippage, accounting for the load adjustments required during the test. The only other markings on the specimen were four short radial cracks around the hole. These were less than ½ the hole diameter.

The load-time trace recorded the lower load limit of 25 lbs and a high limit of 270 lbs during the 2.4% maximum strain cycling. The load during the 2.3% maximum strain cycling period was 255 lbs. The Δ load range versus Δ strain range beyond the 100 cycle hysteresis stabilization period was the following:

Δ load range = 210 - 260 lb

Δ strain range = 1.30 - 1.55%

These values correspond to a modulus range (based upon the cross sectioned area at the hole) of 2.766×10^5 to 2.872×10^5 psi (i.e., no change from static data).

The 2000-cycle fatigue test was performed in a similar manner except that the specimen did not incorporate a hole. This cycling test was conducted in the Instron loading system at a rate of 12 cycles per minute which represented the minimum cycling rate of the equipment. The instrumentation was the same as for the 10,000 cycle fatigue test. The specimen was to cycle between 0.2 - 0.5% and 1.8 - 2.0% strain.

The lower limit of load was set at 20 lbs to obtain the lower limit of strain. Cycling was started and the upper limit of load adjusted to obtain a 1.9% strain excursion in the gage section. Hysteresis effects similar to the 10,000 cycle test caused the strain limits to drift upward during the first dozen cycles until the lower limit stabilized at 0.7% and the upper limit at 2.6% from the initial zero settings. While adjusting the upper limit of load during the first dozen cycles, the specimen was overloaded to a strain level of 3.1% (385-lb load). After the hysteresis stabilization period (~12 cycles), the load time trace recorded a lower load limit of 20 lbs and an upper limit of 315 lbs at 2.6% maximum strain. The Δ load vs. Δ strain range beyond the hysteresis stabilization period was as follows:

Δ load range = 2.73 - 289 lbs

Δ strain range = 1.84 - 2.05%

As in the case of the 10,000 cycle test, the tensile modulus was apparently unaffected by the cycling test. The above strain and load values yield a tensile modulus range from 2.292×10^5 - 2.413×10^5 psi. After cycling the sample was stressed to failure. The load deflection curve yielded the following data:

Yield Strength 0.2% (psi)	Ult. Stress (psi)	Total Strain %	E (psi)
5670	10,000	34.0	2.9×10^5

The tensile modulus derived from vendor data is 2.67×10^5 psi.

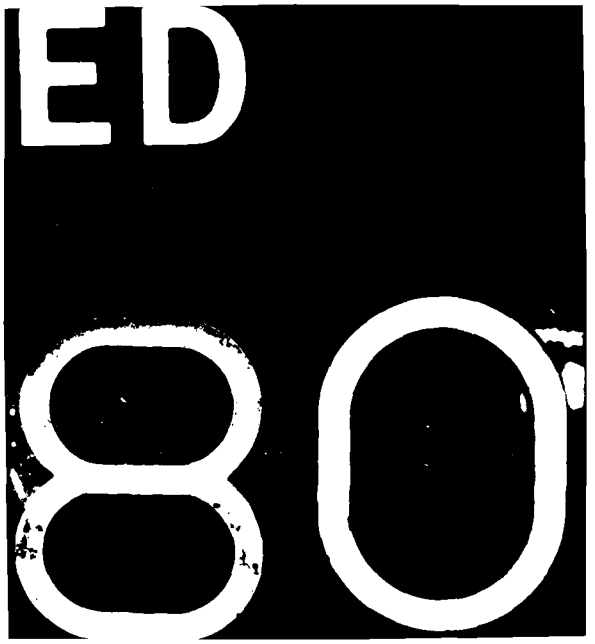
ED
80